

Naval Command,  
Control and Ocean  
Surveillance Center RDT&E Division

San Diego, CA  
92152-5001

4

AD-A262 325



Technical Report 1501  
September 1992

DTIC  
ELECTE  
MAR 31 1993  
S C D

# VLF Source Localization with a Freely Drifting Acoustic Sensor Array

G. C. Chen

Reproduced From  
Best Available Copy

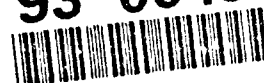
20000920076

Approved for public release; distribution is unlimited.



93 3 30 079

93-06492



15708

Technical Report 1501  
September 1992

# VLF Source Localization with a Freely Drifting Acoustic Sensor Array

G. C. Chen

DTIC QUALITY INSPECTED 1

Accession For	
NTIS CRA&I	<input checked="checked" type="checkbox"/>
DTIC TAB	<input type="checkbox"/>
Unannounced	<input type="checkbox"/>
Justification	
By	
Distribution /	
Availability Codes	
Dist	Avail and/or Special
A-1	

**NAVAL COMMAND, CONTROL AND  
OCEAN SURVEILLANCE CENTER  
RDT&E DIVISION  
San Diego, California 92152-5000**

---

**J. D. FONTANA, CAPT, USN**  
Commanding Officer

**R. T. SHEARER**  
Executive Director

---

**ADMINISTRATIVE INFORMATION**

The work detailed in this report was performed for the NO3A Block program of the Office of Naval Technology, 800 North Quincy Street, Arlington, VA 22217, under program element 0602314N, project RJ14C32, accession number DN308105.

Released by  
C. E. Persons, Head  
Processing Applications Branch

Under authority of  
J. A. Roese, Head  
Signal and Information  
Processing Division

**ACKNOWLEDGMENTS**

I would like to express my sincere gratitude to my advisor, Professor W. S. Hodgkiss for his guidance and advice during the research of this thesis. I also wish to thank my committee members for reviewing this dissertation and offering constructive criticism.

I am indebted to the graduate academic fellowship program sponsored by the Naval Command, Control and Ocean Surveillance Center's RDT&E Division (NRaD) (formerly Naval Ocean Systems Center) and the support of the NO3A Block program of the Office of Naval Technology. Without their support, my graduate studies at UCSD would not have been possible. Special thanks are due to Dr. C. E. Persons, Dr. D. K. Barbour, and Dr. J. A. Roese of NRaD for their continuous encouragement and unwavering support over the last few years.

During a major portion of this research, the Marine Physical Laboratory (MPL) kindly provided the office space and computing facilities. The hospitality of MPL during this period is greatly appreciated. I have enjoyed sharing ideas and learning from several members of Professor W. S. Hodgkiss' acoustic signal-processing research group at MPL. Special thanks go to Dr. G. L. D'Spain for sharing his expertise with the Swallow floats and Dr. J. M. Tran, a former member of MPL, for many insightful discussions on array processing. I also thank the members of the Swallow float team for preparing the sea experiment and collecting the experimental data needed in this dissertation. The Swallow float experiment was sponsored by the Office of Naval Research.

Finally, I am grateful to my family for their support and for enduring the countless hours of my graduate studies over these last few years. It is to them I dedicate this dissertation.

JA

## SUMMARY

### OBJECTIVE

The objective of this study is to demonstrate the source localization and tracking capability of the freely drifting Swallow float volumetric array with the matched-field processing (MFP) technique using data collected during the 1989 Swallow float experiment conducted in the Northeast Pacific.

### RESULTS

Marine Physical Laboratory's set of nine freely drifting, infrasonic sensors, capable of recording ocean ambient noise in the 1- to 25-Hz range, was deployed to span the water column of 4100-m depth, with horizontal aperture on the order of 5 km. Even though the floats were freely drifting, their positions were determined with the 8-kHz internal navigation system and a postprocessing least-squares-based localization procedure. The rms position error estimated by the float localization procedure is less than 5 meters, which is within the desired accuracy of one-tenth of a wavelength at the highest frequency of interest, 25 Hz (6 m), in order to effectively beamform the acoustic data. Analysis of the acoustic data showed high signal-to-noise ratio and high magnitude-squared coherence at 14 Hz among all floats during some time intervals. The 14-Hz was a continuous wave (cw) tone projected by a source of opportunity deployed about 2500 km from the Swallow float array. The high coherence among the floats provided an opportunity to matched-field process the acoustic data. The replica pressure field was modeled with an adiabatic normal-mode numerical technique using the environmental data collected during the experiment. Initial MFP of the experimental data revealed difficulties in estimating the source depth and range while the source azimuth estimate was quite successful. The main cause of the MFP performance degradation was incomplete knowledge of the environment. An environment adaptation technique using a global optimization algorithm was developed to alleviate the environmental mismatch problem. With limited knowledge of the environment and a known location of the 14-Hz source during a selected time interval according to the source log, the ocean-acoustic environment can be adapted to the acoustic data in a matched-field sense. Using the adapted environment, the 14-Hz source was successfully localized and tracked in azimuth and range within a region of interest using the MFP technique for a period of 6 hours.



# CONTENTS

TABLE OF CONTENTS .....	ii
LIST OF FIGURES .....	v
LIST OF TABLES .....	x
INTRODUCTION .....	1
1. MATCHED-FIELD ARRAY PROCESSING .....	3
1.1 Introduction.....	3
1.2 Replica Pressure Field Modeling.....	3
1.2.1 Range-Independent Environment .....	4
1.2.1.1 Normal Mode Model .....	5
1.2.1.2 Fourier Integral Model.....	6
1.2.2 Range-Dependent Environment.....	6
1.2.2.1 Normal Mode Model .....	6
1.2.2.2 Parabolic Equation Model .....	7
1.3 Beamforming Processor Structure .....	8
1.3.1 Bartlett Method .....	8
1.3.2 Minimum Variance Method.....	9
1.3.3 Eigenvector Method.....	11
1.4 Summary.....	12
2. 1989 SWALLOW FLOAT EXPERIMENT.....	14
2.1 Introduction.....	14
2.2 Swallow Float System Description.....	14
2.3 1989 Experiment Summary .....	16
2.4 Data Description .....	19
2.4.1 8-KHz Range Data.....	19
2.4.2 Acoustic VLF Data .....	19
2.4.3 Environmental Data .....	22
2.5 Summary.....	25
3. SWALLOW FLOAT LOCALIZATION.....	26
3.1 Introduction.....	26
3.2 Float Localization Techniques .....	27
3.2.1 Least-Squares Filter .....	27
3.2.2 Kalman Filter .....	27
3.3 Inputs to the Localization Filter.....	30
3.3.1 Measurement Data .....	30
3.3.1.1 Travel Time Estimates .....	30
3.3.1.2 Sound Speed Estimates.....	36
3.3.2 Measurement Statistics .....	39
3.3.2.1 Travel Time Variances.....	39

3.3.2.2	Sound Speed Variances .....	42
3.3.3	Initial Estimates .....	42
3.3.3.1	Initial Position Estimates .....	43
3.3.3.2	Initial Velocity Estimates .....	44
3.3.3.3	Initial Position and Velocity Variance Estimates .....	46
3.4	Filter Tuning .....	47
3.4.1	Least-Squares Filter .....	47
3.4.2	Kalman Filter .....	48
3.5	Localization Results .....	50
3.6	Summary .....	56
4.	SOURCE LOCALIZATION WITH SWALLOW FLOAT ARRAY .....	57
4.1	Introduction .....	57
4.2	VLF Acoustic Data Preparation .....	58
4.2.1	Aligning Float Time Bases .....	58
4.2.2	Selecting Data Records .....	60
4.2.2.1	Signal-to-Noise Ratio .....	60
4.2.2.2	Spatial Coherence .....	60
4.2.3	Estimating the Array Covariance Matrix .....	63
4.2.4	Inverting the Array Covariance Matrix .....	63
4.3	Acoustic Propagation Modeling .....	64
4.3.1	Environmental Data .....	65
4.3.2	Modeling with Adiabatic Normal Modes .....	65
4.3.2.1	Depth Eigenfunctions .....	67
4.3.2.2	Horizontal Wave Numbers .....	70
4.3.2.3	3-D Field Approximation .....	71
4.4	Experimental Data-Processing Results .....	72
4.5	Controlled Simulation .....	76
4.5.1	No Mismatch Simulations .....	76
4.5.2	Uncertainty in Float Positions .....	80
4.5.3	Uncertainty in Sound Speed Structure .....	84
4.6	Summary .....	84
5.	SELF-COHERENT MATCHED-FIELD PROCESSING .....	89
5.1	Introduction .....	89
5.2	Literature Review .....	89
5.2.1	Self-Cohering Technique .....	89
5.2.2	Focalization Technique .....	91
5.3	Environment Adaptation Technique .....	91
5.3.1	Global Optimization Method .....	92
5.3.1.1	Motivation .....	93
5.3.1.2	Simulated Annealing Algorithm .....	93
5.3.1.3	Fast Simulated Annealing Procedure .....	94
5.3.2	Reducing the Parameter Search Spaces .....	95

---

5.4	Processing Results .....	97
5.4.1	Simulation .....	97
5.4.1.1	Sound Speed Adaptation .....	98
5.4.1.2	Wave Number Adaptation .....	106
5.4.1.3	Remarks .....	112
5.4.2	Experimental Data .....	117
5.4.2.1	Sound Speed Adaptation .....	117
5.4.2.2	Wave Number Adaptation .....	123
5.5	Summary .....	123
CONCLUSIONS .....		128
APPENDICES .....		130
REFERENCES .....		137

## FIGURES

Figure 1.1	General beamformer structure. ....	9
Figure 2.1	Schematic drawing of a typical Swallow float. ....	15
Figure 2.2	Swallow floats deployment geometry and float retrieval positions, July 1989, 34° N, 122° W. ....	17
Figure 2.3	Planned Swallow float deployment depth. Also plotted in this figure is the sound speed profile based on historical temperature and salinity data. ....	18
Figure 2.4	8-kHz acoustic range pulses received by float 1 (freely drifting) as a function of time during the July, 1989, experiment. The horizontal axis of the figure gives the time in units of Swallow float record number. Eighty records represent one hour. ....	20
Figure 2.5	VLF acoustic spectrogram of float 1, 00:28 - 08:28 PST, 9 July 1989. The vertical axis of the figure gives the time in units of Swallow float record number. Eighty records represent one hour. ....	21
Figure 2.6	MARK VI source - Swallow float array geometry, 9 July 1989. The line of triangles marks the AXBT measurements taken between 8 - 10 July 1989. ....	23
Figure 2.7	Sound speed profiles collected during the 1989 experiment. ....	24
Figure 3.1	Swallow float array geometry conceptual diagram. ....	26
Figure 3.2	Float 2 listening to float 8, July 1989 experiment. The horizontal axis of the figure gives the time in units of Swallow float record number. Eighty records represent one hour. ....	32
Figure 3.3	Float 8 listening to float 2, July 1989 experiment. The horizontal axis of the figure gives the time in units of Swallow float record number. Eighty records represent one hour. ....	32
Figure 3.4	Travel time estimates between two freely drifting floats (2 and 8). The horizontal axis of the figure gives the time in units of Swallow float record number. Eighty records represent one hour. ....	33
Figure 3.5	Leading edges of each float's detection of its own surface echo pulses. The horizontal axis of the figure gives the time in units of Swallow float record number. Eighty records represent one hour. ....	34
Figure 3.6	Float 11 surface echo pulses, July 1989 experiment. The horizontal axis of the figure gives the time in units of Swallow float record number. Eighty records represent one hour. ....	35
Figure 3.7	Histogram of float 11 surface echoes minus the mean 5411 msec (binwidth is one msec), July 1989 experiment. ....	35
Figure 3.8	Float 9 listening to float 11, July 1989 experiment. The horizontal axis of the figure gives the time in units of Swallow float record number. Eighty records represent one hour. ....	37

Figure 3.9	Float 11 listening to float 9, July 1989 experiment. The horizontal axis of the figure gives the time in units of Swallow float record number. Eighty records represent one hour. ....	37
Figure 3.10	Direct path travel time estimates between bottomed floats 9 and 11, calculated using constant mode values of surface echo travel times, July 1989 experiment. The horizontal axis of the figure gives the time in units of Swallow float record number. Eighty records represent one hour. ....	38
Figure 3.11	Histogram of direct path travel time estimates minus the mean 4159 msec (binwidth is one msec), July 1989 experiment. ....	38
Figure 3.12	Travel time difference between floats 2 and 8 and a second-order fit, July 1989 experiment. The horizontal axis of the figure gives the time in units of Swallow float record number. Eighty records represent one hour. ....	41
Figure 3.13	Travel time difference (floats 2 and 8) minus second-order fit, July 1989 experiment. The horizontal axis of the figure gives the time in units of Swallow float record number. Eighty records represent one hour. ....	41
Figure 3.14	Plane view of coordinate system used for float localization. ....	43
Figure 3.15	Mean innovation and RMS error of the Kalman and least-squares filters, July 1989 experiment. ....	51
Figure 3.16	RMS residual of least-squares filter position estimates, July 1989 experiment. The horizontal axis of the figure gives the time in units of Swallow float record number. Eighty records represent one hour. ....	51
Figure 3.17	Float horizontal displacement estimates using least-squares filter during the July 1989 experiment. The circles mark the starting positions. ....	52
Figure 3.18	Float depth estimates using least-squares filter, July 1989 experiment. The horizontal axis of the figure gives the time in units of Swallow float record number. Eighty records represent one hour. ....	53
Figure 3.19	Float depth estimates using Kalman filter, July 1989 experiment. The horizontal axes of the figure give the time in units of Swallow float record number. Eighty records represent one hour. ....	54
Figure 3.20	Float speed estimates derived from the Kalman filter's X, Y, and Z velocity estimates, July 1989 experiment. The horizontal axes of the figure give the time in units of Swallow float record number. Eighty records represent one hour. ....	55
Figure 4.1	Matched-field processing block diagram. ....	57
Figure 4.2	(a) Float 2 listening to float 8, (b) Float 8 listening to float 2, (c) Travel time difference between floats 2 and 8, and (d) Second-order fit of (c). ....	59

Figure 4.3	Acoustic pressure power spectra for midwater floats. ....	61
Figure 4.4	(a) Spatial coherence at 14 Hz and (b) Phase difference between floats 0 and 2 at 14 Hz during records 1040 - 1240. ....	62
Figure 4.5	Sound speed profiles between 150° W and 122° W. ....	66
Figure 4.6	Sound speed profiles at the source and Swallow float array. ....	66
Figure 4.7	Modal eigenfunctions at frequency of 14 Hz. ....	68
Figure 4.8	Ray traces for source at 90 m. ....	69
Figure 4.9	Matched-field processing results using the Bartlett method for the 14-Hz source during record 1145. ....	73
Figure 4.10	Matched-field processing results using the MV method for the 14-Hz source during record 1145. ....	74
Figure 4.11	Matched-field processing results using the MUSIC method for the 14-Hz source during record 1145. ....	75
Figure 4.12	Matched-field processing simulation results (no mismatch) using the Bartlett method. ....	77
Figure 4.13	Matched-field processing simulation results (no mismatch) using the MV method. ....	78
Figure 4.14	Matched-field processing simulation results (no mismatch) using the MUSIC method. ....	79
Figure 4.15	Matched-field processing simulation of uncertainty in sensor positions using the Bartlett method. ....	81
Figure 4.16	Matched-field processing simulation of uncertainty in sensor positions using the MV method. ....	82
Figure 4.17	Matched-field processing simulation of uncertainty in sensor positions using the MUSIC method. ....	83
Figure 4.18	Matched-field processing simulation of uncertainty in sound speed structure using the Bartlett method. ....	85
Figure 4.19	Matched-field processing simulation of uncertainty in sound speed structure using the MV method. ....	86
Figure 4.20	Matched-field processing simulation of uncertainty in sound speed structure using the MUSIC method. ....	87
Figure 5.1	Environment adaptation technique block diagram. ....	92
Figure 5.2	Matched-field simulation (no mismatch) of 14-Hz source for the three time intervals corresponding to the experimental data collected during 1989 experiment. ....	99
Figure 5.3	Matched-field simulation of environmental mismatch for the three time intervals corresponding to the experimental data collected during 1989 experiment. ....	100
Figure 5.4	(a) Excess (demeaned) sound speed profiles computed from 30 AXBT measurements made between 140° W and 150° W, July 1989, (b) Normalized versions of the first and second EOFs derived from (a). ....	101

Figure 5.5	Trajectories of the sound speed EOF coefficients and cost function learning curve for a typical annealing run. ....	103
Figure 5.6	Energy surface as a function of sound speed EOF coefficients computed by exhaustive search (simulation). ....	104
Figure 5.7	Joint trajectories of sound speed EOF coefficients for different annealing runs. ....	105
Figure 5.8	(a) Sound speed profile derived from the environment adaptation technique (dotted line), "true" profile (solid line), and measured sound speed profile (dashed line); (b) the difference version of (a), i.e., using the measured profile as reference (dashed line), the "true" minus the measured and the adapted minus the measured are in solid and dotted lines, respectively (simulation). ....	107
Figure 5.9	Self-cohered source locations by environment adaptation technique using sound speed EOF coefficients as search parameters. ....	108
Figure 5.10	(a) Excess (demeaned) horizontal wave numbers at 14 Hz derived from 30 AXBT measurements made between 140° W and 150° W, July 1989, (b) Normalized versions of the first and second EOFs derived from (a). ....	109
Figure 5.11	Trajectories of the wave number EOF coefficients and cost function learning curve for a typical annealing run (simulation). ....	110
Figure 5.12	Energy surface as a function of wave number EOF coefficients computed by exhaustive search (simulation). ....	111
Figure 5.13	Joint trajectories of the wave number EOF coefficients for different annealing runs. ....	113
Figure 5.14	Deviations in adapted wave numbers and "true" wave numbers from the measured model wave numbers (simulation). ....	114
Figure 5.15	Self-cohered source locations by environment adaptation technique using wave number EOF coefficients as search parameters (simulation). ....	115
Figure 5.16	Range-azimuth energy surface derived from repeating the optimization procedure for each range-azimuth cell (simulation). ....	116
Figure 5.17	Matched-field processing of experimental data during the three time intervals. ....	118
Figure 5.18	Range-azimuth energy surface derived from repeating the optimization procedure for each range-azimuth cell using data collected at 01:47 PST, July 1989. ....	119
Figure 5.19	Energy surface as a function of sound speed EOF coefficients computed by exhaustive search corresponds to source location during 01:47 PST, July 1989. ....	120
Figure 5.20	(a) Sound speed profile (dotted line) computed from the optimal EOF coefficients obtained from Figure 5.19 and the averaged model sound speed profile (dashed line). (b) The difference version of (a) i.e., using the measured profile as reference	

	(dashed line), the adapted minus the measured is plotted in dotted line. ....	121
Figure 5.21	Self-cohered source locations by environmental adaptation technique using sound speed EOF coefficients as the search parameters. ....	122
Figure 5.22	Energy surface as a function of wave number EOF coefficients computed by exhaustive search corresponds to source location during 01:47 PST, July 1989.....	124
Figure 5.23	Adapted wave numbers compared to measured model wave numbers.....	125
Figure 5.24	Self-cohered source locations by environmental adaptation technique using wave number EOF coefficients as the search parameters. ....	126



## TABLES

Table 2.1	Planned and actual deployment depths, July 1989 experiment.	16
Table 3.1	Surface echo travel time estimates for bottomed floats.	31
Table 3.2	Direct path travel time estimates between bottomed floats.	36
Table 3.3	Estimated variance of bottomed float travel time, July 1989 experiment.	39
Table 3.4	Estimated variance of bottomed float travel time based on predicted float movement, July 1989 experiment.	40
Table 3.5	Estimated variance of freely drifting float travel time, July 1989 experiment.	42
Table 3.6	Rough initial-position estimate, record 1003, 00:00 July 9 1989.	44
Table 3.7	Initial-position estimate produced by the least-squares filter for record 1003, 00:00, July 9 1989.	45
Table 3.8	Initial velocity estimate (in meters/second), record 1003, 00:00, July 1989 experiment.	45
Table 3.9	Estimate of initial position and velocity variance used by the Kalman filter, July 1989 experiment.	46
Table 3.10	Bottomed float surface echo and direct path between bottomed floats travel time estimate, July 1989 experiment.	48
Table 3.11	Mean innovation power produced by the Kalman filter, July 1989 experiment.	49
Table 3.12	Average float speed, July 1989 experiment.	56
Table 4.1	Equivalent source angles for modes trapped in the water column at a frequency of 14 Hz.	70
Table 4.2	Eigenvalues for modes trapped in the water column at a frequency of 14 Hz.	71
Table 4.3	Matched field processing results.	72
Table 4.4	Matched-field processing array gain.	76
Table 4.5	Matched-field simulation of sensor position errors.	80
Table 4.6	Matched-field simulation of sound speed mismatch.	84
Table 5.1	The five largest eigenvalues obtained from eigen-decomposition of the sound speed covariance matrix.	98
Table 5.2	Optimization results from nine runs using sound speed EOF coefficients as search parameters.	102
Table 5.3	The five largest eigenvalues obtained from eigen-decomposition of the wave number covariance matrix.	106
Table 5.4	Optimization results from nine runs using wave number EOF coefficients as search parameters.	112

## INTRODUCTION

Traditionally, source localization has relied on the processing of assumed plane-wave fronts received by spatially distributed sensors to estimate the source bearing or vertical angle of arrivals. In reality, the ocean acoustic channel is extremely complex due to refractive and multipath effects. Assumption of plane-wave arrivals in the processing scheme can lead to severe degradation of the estimate. Matched-field processing (MFP) has been proposed [Bucker, 1976] to actually use the complex ocean acoustic properties to improve source detection and localization. MFP involves the correlation of the actual acoustic pressure field measured at the array with a predicted field due to a source at an assumed location deriving from an acoustic propagation model. A high degree of correlation between the measured field and the predicted field indicates a likely source location. Matched-field processing of the acoustic wavefield has shown that when sufficient environmental characterizations (e.g., sound speed profile, bathymetry, sediment properties) are available, rather remarkable detection and estimation results can be obtained. Most available matched-field work has been for rather simple propagation situations (e.g., range-independent environment or shallow water environment) and much of the work has been restricted to vertical-line arrays [Bucker, 1976; Porter et. al., 1987; Fizell, 1987; Baggeroer et. al., 1988; Ozard, 1989; Feuillade et. al., 1990; Bala and Ozard, 1990; Sotirin et. al., 1990; Tran and Hodgkiss, 1991].

Although matched-field processing offers an appealing approach to the underwater source detection and estimation problem, a common difficulty with this technique occurs when the environment information is inaccurate. A "mismatch" occurs between the measured data and the modelled pressure field, and the performance of the MFP is degraded and leads to errors in the estimation of the source location [Tolstoy, 1989; Feuillade et. al., 1989; Hamson and Heitmeyer, 1989; Gingras, 1989; Daugherty and Lynch, 1990].

The focus of this dissertation research is twofold: (1) to demonstrate the match-field source localization and tracking capability of the Swallow float freely drifting volumetric array using experimental data, and (2) to study the environmental mismatch problem and investigate the technique that may neutralize the effect caused by imprecise knowledge of the environment and thereby lead to MFP localization performance enhancement.

This dissertation is organized as follows. Chapter 1 presents an overview of the most commonly used low-frequency acoustic propagation models and array processing power estimators. Five acoustic propagation models are presented in categories reflecting the ability of the model to handle environmental range dependence. Three array processing methods (Bartlett, Minimum Variance, and MUSIC) are reviewed in the context of matched-field processing, and the basic concepts and properties associated with each method are discussed.

Chapter 2 gives a brief description of the Swallow float system and a summary of the July 1989 Swallow float experiment. Data collected during the experiment, which includes 8-kHz range data, VLF acoustic data, and environmental data, are presented.

In chapter 3, the 8-kHz range data collected by the Swallow floats during the 1989 experiment are used to estimate float positions as a function of time. Two methods (least-squares and Kalman filters) used in localizing the floats are reviewed, and their results are compared.

Chapter 4 presents the results of matched-field processing on the 14-Hz continuous wave (cw) tone collected by the Swallow floats during the 1989 experiment. Issues related to float time-base alignment, data selection criteria, and array covariance matrix estimation are addressed. An adiabatic normal-mode modeling technique and the environmental data collected during the experiment are used to model the acoustic replica pressure fields. All three array processors are implemented and used to compute the matched-field, range-depth and range-azimuth ambiguity surfaces on the experiment data. Controlled simulation is also performed to aid in interpreting the experimental data processing result.

Chapter 5 addresses the environmental mismatch problem. Two techniques, self-cohering and focalization, reported in the literature are briefly reviewed. An environment adaptation technique using a global optimization procedure is proposed to enhance the MFP localization performance. The optimization procedure is implemented using the empirical orthogonal function (EOF) approach to reduce the parameter spaces and a fast simulated annealing algorithm to search for the optimal environmental parameter values. Two types of environmental parameters are considered: sound speed structure and modal wave number. The technique is illustrated using both simulation and experimental data.

Lastly, a summary of this dissertation and a discussion of area of future research is given.

# 1. MATCHED-FIELD ARRAY PROCESSING

## 1.1 Introduction

The problem of coherently summing the outputs from a number of spatially distributed sensors to form a spatial filter is known as beamforming [De Fatta, Lucas, and Hodgkiss, 1988]. In underwater signal processing, conventional beamforming can be viewed as correlating the pressure field measured at the sensors with a plane-wave replica at an assumed incidence angle on the array. A peak in the plane of azimuthal and elevation angle indicates the presence and direction of the source. However, due to the refractive and multipath effects in the ocean, the acoustic pressure field received by an array from a low-frequency narrowband point source cannot be expected to be planar. The nature of the field is a function of range, depth, and azimuth of the source as well as a function of the sound speed structure and the characteristics of the ocean surface and bottom. If array detection and localization performance are to be maximized, the assumed replica for the signal field must match the actual field as closely as possible. Then the steering vector must scan in range, depth, and azimuth, rather than just in directions. Scanning in range, depth, and azimuth requires a prediction of the spatial structure of the received acoustic field for each potential source location. The resulting spatial-filtering process is referred to as matched-field processing. Matched-field processing is a generalization of conventional plane-wave beamforming. In essence, MFP matches the measured field at the array with a realistic acoustic model prediction of the pressure due to a source at an assumed location. In this case, a peak in the range/depth/azimuth ambiguity surfaces indicates the presence and location of the source.

To allow source detection and localization in the matched-field sense, the correlation between the measured pressure field and the replica field must be measured. Thus, the major signal processing functions for matched-field processing include acoustic propagation modeling, which predicts the replica pressure field, and beamformer power estimation, which represents the agreement between actual and replica fields.

## 1.2 Replica Pressure Field Modeling

Formulations of acoustic propagation modeling generally begin with the wave equation. The wave equation is a partial differential equation relating the acoustic pressure or the velocity potential to the space and time, and may be written as

$$\nabla^2 \Phi = \frac{1}{c^2(x, y, z)} \frac{\partial^2 \Phi}{\partial t^2} \quad (1.1)$$

where  $\nabla^2$  is the Laplacian operator,  $\Phi$  is the velocity potential function, and  $c$  is the speed of sound. If harmonic solution is assumed for the potential function

$$\Phi = \phi e^{-i\omega t} \quad (1.2)$$

where  $\phi$  is the time-independent potential function, and  $\omega$  is the source frequency.

Then Equation (1.1) can be reduced to

$$\nabla^2 \phi + k^2 \phi = 0 \quad (1.3)$$

or in cylindrical coordinates,

$$\frac{\partial^2 \phi}{\partial r^2} + \frac{1}{r} \frac{\partial \phi}{\partial r} + \frac{\partial^2 \phi}{\partial z^2} + k^2(z) \phi = 0 \quad (1.4)$$

where  $k = \frac{\omega}{c}$ .

Equation (1.3) is the time-independent (or frequency domain wave equation) also known as the Helmholtz equation. Various theoretical approaches are applicable to the Helmholtz equation depending upon the specific geometrical assumptions made for the propagation and the type of solution chosen for  $\phi$ . In practice, the Helmholtz equation is too complex for analytical solutions; numerical methods are generally used.

To describe the different wave theory numerical modeling approaches, it is convenient to divide them according to range-independent and range-dependent types. Range independence means that the model assumes a cylindrical symmetry for the environment (i.e., a horizontally stratified ocean in which properties vary only as a function of depth). Range dependence indicates that some properties of the ocean medium are allowed to vary as a function of range ( $r$ ) and azimuth ( $\theta$ ) between the source and sensor, in addition to a depth ( $z$ ) dependence. Such range-varying properties commonly include sound speed structure, bathymetry, and sediment properties. The following sections review low-frequency acoustic modeling techniques commonly referenced in the literature. The presentation closely follows an excellent paper [Jensen, 1988] and a recent text [Etter, 1991].

### 1.2.1 Range-Independent Environment

If the ocean is assumed to be perfectly horizontally stratified and azimuthally symmetrical, i.e., the sound speed  $c(z)$  varies only with depth, the solution for the potential function  $\phi$  can be written as the product of a depth function  $Z(z)$  and a range function  $R(r)$  using the separation of variables technique:

$$\phi = Z(z) R(r) \quad (1.5)$$

If the separation constant is designated  $\xi^2$ , the separated equations are [Boyles, 1984]

$$\frac{d^2 Z}{dz^2} + (k^2 - \xi^2) Z = 0 \quad (1.6)$$

$$\frac{d^2 R}{dr^2} + \frac{1}{r} \frac{dR}{dr} + \xi^2 R = 0 \quad (1.7)$$

Equation (1.6) is the depth equation, known as normal mode equation, which describes the standing wave portion of the solution; its solution is the Green's function. Equation (1.7) is the range equation, a zero-order Bessel equation, which describes the traveling wave portion of the solution; its solution can be written in terms of a zero-order Hankel function. The full solution for  $\phi$  can then be expressed by an infinite integral, assuming a single-frequency point source:

$$\phi(r, z) = \int_{-\infty}^{\infty} G(z, z_0; \xi) H_0^{(1)}(\xi r) \xi d\xi \quad (1.8)$$

where  $G()$  is the depth-dependent Green's function, and  $H_0^{(1)}()$  is the zero-order Hankel function for the first kind, and  $z_0$  is the source depth.

### 1.2.1.1 Normal Mode Model

To obtain the normal mode solution to the wave equation, the Green's function is expanded into a complete set of normal mode functions  $u_m$ . The eigenvalues (or the horizontal wave numbers), which are the resulting value of the separation constants, are represented by  $\xi_m$ . These eigenvalues represent the discrete set of values for which solutions of the modal eigenfunctions  $u_m$  exist. The spectrum of eigenvalues generally consists of both a discrete part and a continuous part. By ignoring the continuous part, which corresponds to sound interacting with the bottom at angles above the critical grazing angle (or nonpropagating source nearfield) and by replacing the Hankel function expression by its far-field asymptotic expansion for  $\xi r \gg 1$ , the solution for  $\phi$  can be written as a modal sum:

$$\phi(r, z) = \text{const} \sum_{m=1}^M u_m(z_0) u_m(z) \frac{e^{i\xi r}}{\sqrt{\xi r}} \quad (1.9)$$

where  $M$  is the number of propagating modes.

### 1.2.1.2 Fourier Integral Model

An alternative approach to (1.8) is to replace the Hankel function expression in (1.8) by the first term in the asymptotic expansion:

$$\phi(r, z) = \int_{-\infty}^{\infty} \sqrt{\frac{2\xi}{\pi r}} G(z, z_0; \xi) e^{i\xi r} d\xi \quad (1.10)$$

The infinite integral is then evaluated by means of the fast Fourier transform, which provides value of the potential function  $\phi$  at  $n$  discrete range points for a given source-receiver geometry. This approach requires greater computation effort than the normal mode method but does include the nonpropagating source nearfield.

## 1.2.2 Range-Dependent Environment

### 1.2.2.1 Normal Mode Model

As discussed in the last paragraph, the normal mode model assumes range independence. Extension to range dependence can be accomplished either by mode coupling, which considers the energy scattered from a given mode into other modes, or by invoking the adiabatic assumption, which assumes that all energy in a given mode transfers to the corresponding mode in the new environment, provided that the environmental variations in range are gradual. This section considers two such extensions.

#### Coupled Mode Method

For range-dependent acoustic propagation environment, the range between source and sensor can be divided into a number of range regions, each with range-invariant properties but with allowance for arbitrary variation of environmental parameters with depth within each region. Since the range dependence takes place discretely at the interfaces between regions, the solution within a range-independent region can be constructed using the standard normal mode solution and interface conditions. A complete two-way solution for wave propagation can be written as a sum of local modes with unknown excitation coefficients determined by requiring continuity of pressure and horizontal particle velocity across region boundaries [Evans, 1983]. Computationally, this approach requires the solution of a whole family of normal mode problems, one for each region, followed by a large banded, block linear system. The coupled mode technique does require considerable computational power but provides complete wave solutions with backscattering included.

### Adiabatic Approximation Method

If the cross-mode coupling in the coupled mode method is neglected, we can derive a simple first-order approximation to the full-coupling problem, called the adiabatic normal mode solution. It is assumed that the energy contained in a given mode at the source range will stay in that particular mode throughout the range-varying environment and not couple to neighboring modes. This assumption is accurate for a slow-varying, range-dependent medium. The solution for  $\phi$  in a weak range-dependent environment can be expressed as [Pierce, 1965; Brekhovskikh and Lysanov, 1982]

$$\phi(r, z) = \text{const} \sum_{m=1}^M u_m(z_0; 0) u_m(z; r) \frac{\exp\left(i \int_0^r \xi_m(s) ds\right)}{\sqrt{\xi_m(r) r}} \quad (1.11)$$

The adiabatic mode technique is computationally efficient since no mode coupling effects need to be considered.

#### 1.2.2.2 Parabolic Equation Model

The parabolic equation (PE) approach is a far-field, narrow-angle approximation to the wave equation [Tappert, 1977]. An approximate solution to 2-D propagation problems can be obtained from the parabolic equation, which is derived by assuming a field solution of the form:

$$\phi(r, z) = \psi(r, z) \frac{\exp(ik_0 r)}{\sqrt{r}} \quad (1.12)$$

where  $k_0$  is an average horizontal wavenumber of the propagating wave spectrum. By substituting the expression for  $\phi$  into (1.1), the equation for  $\psi(r, z)$  can be simplified to

$$\frac{\partial^2 \psi}{\partial r^2} + \frac{\partial^2 \psi}{\partial z^2} + 2ik_0 \frac{\partial \psi}{\partial r} + k_0^2 (n^2 - 1) \psi = 0 \quad (1.13)$$

where  $n = k(r, z) / k_0$  is the refraction index. Further assume

$$\frac{\partial^2 \psi}{\partial r^2} \ll 2k_0 \frac{\partial \psi}{\partial r} \quad (1.14)$$

which is the paraxial approximation and is equivalent to saying that if the acoustic field were represented by rays, these would be inclined only at small angles to the horizontal. The paraxial ap-



proximation is the heart of the parabolic equation method, and by combining (1.13) and (1.14) we get

$$\frac{\partial^2 \psi}{\partial z^2} + 2ik_0 \frac{\partial \psi}{\partial r} + k_0^2 (n^2 - 1) \psi = 0 \quad (1.15)$$

This is the standard parabolic equation that represents a wave propagating outwards and close to the horizontal. This approximation takes us from a boundary-value, wave-equation problem to an initial-value, parabolic equation that leads itself to a marching-solution technique when the initial condition is known. Note that PE is an approximation technique that neglects backscattering and, more importantly, assumes energy to propagate within a limited angular spectrum of  $\pm 40^\circ$  with respect to the horizontal.

### 1.3 Beamforming Processor Structure

Conventional beamforming procedures use plane-wave steering vectors as replicas of the true acoustic pressure field and estimate the source bearing by finding the maximum beamformer output that represents the agreement between actual and replica fields. The matched-field processor structure takes the same form as the conventional processor except that the plane-wave replica vector is replaced by a replica vector derived from an acoustic propagation model for the oceanic waveguide of interest. Three such power estimators commonly used in conventional plane-wave array processing that differ in their resolution are reviewed in the context of matched-field processing.

#### 1.3.1 Bartlett Method

Consider the general beamformer structure shown in Figure 1.1. The array of interest consists of  $M$  sensors of known but arbitrary geometry. With  $x_i(f)$  representing the output at the  $i^{\text{th}}$  sensor in frequency domain and  $w_i$  representing the corresponding desired frequency domain weighting factor, the beamformer output can be written as matrix form:

$$Y(f) = W^H X(f) \quad (1.16)$$

The corresponding beamformer output power is given by [Pillai, 1989]

$$P = E[|Y|^2] = E[W^H X X^H W] = W^H R W \quad (1.17)$$

where  $R = E[XX^H]$  is the cross-spectral density matrix or array covariance of the sensor outputs.

If we replace the weight vector  $\mathbf{W}$  by  $\mathbf{E}(r, z, \theta)$ , the replica pressure field vector due to a narrow-band source at  $(r, z, \theta)$ , then the output of the beamformer can be expressed as

$$P_{\text{Bartlett}}(r, z, \theta) = \mathbf{E}^H(r, z, \theta) \mathbf{R} \mathbf{E}(r, z, \theta) \quad (1.18)$$

Since (1.18) has the same form as the Bartlett estimate in spectral estimation, (1.18) is also called a Bartlett processor in array processing literature. The Bartlett processor is known to be robust but offers low resolution.

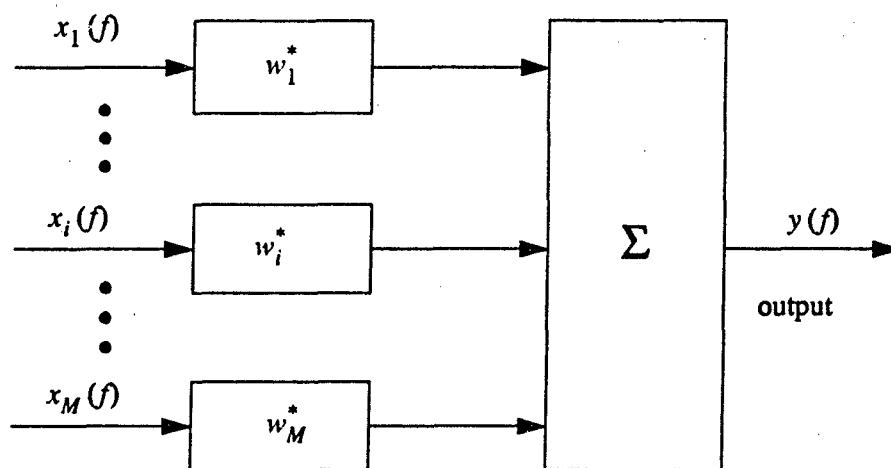


Figure 1.1 General beamformer structure.

### 1.3.2 Minimum Variance Method

Recently, studies of matched-field processing have also centered upon the use of the maximum-likelihood method by Capon [1969] (also known as the minimum variance [MV] method) for its sidelobe suppression capability and high resolution of the mainlobe. Basically, the algorithm adaptively constructs a weight vector  $\mathbf{W}$  that yields a minimum mean-square output  $\mathbf{W}^H \mathbf{R} \mathbf{W}$  to the noise field, with the constraint that signal field is passed with unity gain  $\mathbf{W}^H \mathbf{E} = 1$  when the postulated source location is equal to the true source location:

$$\underset{\mathbf{W}}{\text{minimize}} \mathbf{W}^H \mathbf{R} \mathbf{W} \quad (1.19)$$

$$\text{subject to } \mathbf{W}^H \mathbf{E} = 1 \quad (1.20)$$

In other words, the weight vector minimizes the quadratic function [Kanasewich, 1975]:

$$\underset{\mathbf{W}}{\text{minimize}} \mathbf{W}^H \mathbf{R} \mathbf{W} + \lambda [\mathbf{W}^H \mathbf{E} - 1] \quad (1.21)$$

where  $\lambda$  is an undetermined Lagrange multiplier.

If we express (1.21) as

$$\frac{\partial}{\partial \mathbf{W}} \{ \mathbf{W}^H \mathbf{R} \mathbf{W} + \lambda [\mathbf{W}^H \mathbf{E} - 1] \} = 0 \quad (1.22)$$

(1.22) can be easily reduced to

$$\mathbf{R} \mathbf{W} = \frac{-\lambda}{2} \mathbf{E} \quad (1.23)$$

Multiplying by the inverse of  $\mathbf{R}$  yields

$$\mathbf{W} = \frac{-\lambda}{2} \mathbf{R}^{-1} \mathbf{E} \quad (1.24)$$

To determine the Lagrange multiplier,  $\lambda$ , substitute  $\mathbf{W}$  into the constraint equation (1.20).

$$\lambda = \frac{-2}{\mathbf{E}^H \mathbf{R}^{-1} \mathbf{E}} \quad (1.25)$$

The optimal weight vector is derived as

$$\mathbf{W} = \frac{\mathbf{R}^{-1} \mathbf{E}}{\mathbf{E}^H \mathbf{R}^{-1} \mathbf{E}} \quad (1.26)$$

Substituting (1.26) into (1.17), the corresponding beamformer output power is

$$P_{MV}(r, z, \theta) = \frac{1}{\mathbf{E}^H \mathbf{R}^{-1} \mathbf{E}} \quad (1.27)$$

In general, the Bartlett beamformer has significant sidelobes that often are indistinguishable from the mainlobe. The MV matched-field processor has better suppression of the sidelobes and high resolution of the mainlobe, but it is more sensitive to errors in replica vectors.

### 1.3.3 Eigenvector Method

Intuitively, it appears that we could further improve the resolution properties of the minimum variance beamformer if the denominator of (1.27) could be made smaller in those locations that correspond to signals and larger in locations corresponding to noise. The eigenvector beamformer is derived based on this intuition [Johnson, 1982]. Assuming we have  $M$  sensors and  $K$  sources, it is well known that the  $K$  largest eigenvalues of the array covariance matrix  $\mathbf{R}$  are associated with the sources. The corresponding  $K$  eigenvectors span the signal subspace, that is, they are linear combinations of the signal vectors. Furthermore, the  $M-K$  remaining eigenvectors span a noise subspace orthogonal to the signal subspace. We can express  $\mathbf{R}$  in terms of its eigenvalues  $\lambda_i$  and eigenvectors  $\mathbf{V}_i$ ,  $i = 1, \dots, M$ , using the spectral theorem for a matrix:

$$\mathbf{R} = \sum_{i=1}^M \lambda_i \mathbf{V}_i \mathbf{V}_i^H \quad (1.28)$$

The inverse of  $\mathbf{R}$  has an equally simple form:

$$\mathbf{R}^{-1} = \sum_{i=1}^M \frac{1}{\lambda_i} \mathbf{V}_i \mathbf{V}_i^H \quad (1.29)$$

Next, we form a truncated or noise covariance matrix by including only the  $M-K$  eigenvectors that span the noise subspace. This matrix is denoted by  $\mathbf{R}_N$  and the inverse of  $\mathbf{R}_N$  can be expressed as

$$\mathbf{R}_N^{-1} = \sum_{i=1}^{M-K} \frac{1}{\lambda_i} \mathbf{V}_i \mathbf{V}_i^H \quad (1.30)$$

The noise covariance then is used in (1.26) to find the corresponding optimum weight vector for the eigenvector beamformer:

$$\mathbf{W} = \frac{\mathbf{R}_N^{-1} \mathbf{E}}{\mathbf{E}^H \mathbf{R}_N^{-1} \mathbf{E}} \quad (1.31)$$

The corresponding eigenvector beamformer output power is

$$P_{EV}(r, z, \theta) = \frac{1}{\mathbf{E}^H \mathbf{R}_N^{-1} \mathbf{E}} = \frac{1}{\sum_{i=1}^{M-K} \frac{1}{\lambda_i} |\mathbf{E}^H \mathbf{V}_i|^2} \quad (1.32)$$

Because vectors in the signal space are orthogonal to the noise subspace spanned by  $\mathbf{V}_i$ ,  $i = 1, \dots, M - K$ , the inner product  $\mathbf{E}^H \mathbf{V}_i$  is zero if  $\mathbf{E}$  is in the signal subspace. Thus with the assumption of uncorrelated noise, the denominator of (1.32) is equal to zero for source locations. The power at the output of the beamformer given by (1.32) therefore is infinite in those locations in the signal subspace.

A related eigenvector method called MUSIC (Multiple Signal Classification) [Schmidt, 1986] sets the small eigenvalues equal to unity in the formation of the noise covariance matrix:

$$\mathbf{R}_{N(MUSIC)}^{-1} = \sum_{i=1}^{M-K} \mathbf{V}_i \mathbf{V}_i^H \quad (1.33)$$

Equation (1.32) can be rewritten as

$$P_{MUSIC}(r, z, \theta) = \frac{1}{\mathbf{E}^H \mathbf{R}_{N(MUSIC)}^{-1} \mathbf{E}} = \frac{1}{\sum_{i=1}^{M-K} |\mathbf{E}^H \mathbf{V}_i|^2} \quad (1.34)$$

The effect of setting the small eigenvalues to unity is to "whiten" those locations that do not correspond to the source signals. The resolution capability of the MUSIC method is similar to that of the eigenvector method.

## 1.4 Summary

Matched-field processing is a generalization of plane-wave beamforming in which the plane-wave replicas are replaced by solutions to the wave equation for the environment of interest. There are two stages in applying MFP to narrowband cw data received by the array: full-wave field modeling and power estimation. Full-wave field modeling involves the use of an acoustic propagation numerical model for predicting the acoustic pressure field in a waveguide of known environmental properties. Based on the model, the acoustic replica pressure field at each sensor of the array may be computed for a source at a particular position with respect to the array. Power estimation consists of matching the replica pressure fields with the measured data. Peak in the power output with respect to range, azimuth, and depth may be taken as estimates of the position of the source within the waveguide. In this chapter, five common low-frequency acoustic propagation modeling techniques were reviewed. Area of applicability for each modeling technique was described. Three of the most commonly used array processing techniques were reviewed in the

context of matched-field processing. The Bartlett method is a conventional technique that is robust but offers low resolution; the minimum variance method is a data adaptive technique that yields higher resolution; and the eigenvector method exploits the orthogonality principal that achieves even higher resolution.

## 2. 1989 SWALLOW FLOAT EXPERIMENT

### 2.1 Introduction

Data presented in this thesis were collected by the Marine Physical Laboratory's (MPL's) Swallow floats between 8 and 9 July 1989, approximately 150 km west-northwest of Pt. Arguello, California, near 34° 50' N, 122° 20' W. A detailed trip report for the experiment is contained in [Chen et. al., 1990]. This chapter describes the Swallow float system description; a summary of the experiment; and representative data collected during the experiment.

### 2.2 Swallow Float System Description

Over the last several years, MPL has designed and developed a set of 12 acoustic sensors that are neutrally buoyant and freely drifting when deployed in the ocean. The sensors are called Swallow floats in honor of J. C. Swallow who used freely drifting floats to measure deep ocean currents. The MPL Swallow floats are used to measure acoustic energy in the very low frequency (VLF) band, which is generally defined as 1 to 25 Hz. The Swallow floats are designed to operate without tether so that their measurements are not contaminated by tether strumming noise and flow noise.

As illustrated in Figure 2.1, the Swallow float system is a 17-inch-diameter glass float containing three orthogonally oriented geophones used as the acoustic particle velocity sensor, a compass, the electronics and power supply. External to the sphere are a hydrophone for measuring VLF acoustic pressure, an 8-kHz acoustic transducer for transmitting and receiving acoustic ranging signals, an optical flash, a radio beacon, and the release ballast [D'Spain et. al., 1991].

In operation, the floats are deployed and ballasted to neutral buoyancy at the desired depths. While deployed, each float records signals from the three geophones and the hydrophone sampled at 50 Hz, the compass, and the 8-kHz range pulse arrival times. Each float continuously fills a 12-kB buffer memory, then periodically writes this buffer to tape. Float time is divided into 45-second periods consisting of 44 seconds during which the geophone and hydrophone outputs are sampled and stored in the buffer and 1 second during which the buffer contents are written to tape. No data are recorded during the 1-second data dump. Limited by tape-recorder capacity (i.e., 17 Mbytes) the data acquisition period is about 19 hours.

Suspended below the glass sphere is an acoustic transducer with source strength 192 dB re 1  $\mu$ Pa at 1 meter that generates and receives 8-kHz tone bursts. Pulses 10 ms long are transmitted by the floats in a programming sequence. A different float transmits every 45 seconds. When 12 floats are deployed, each float transmits every 9 minutes. The floats are listening whenever they are not transmitting. They receive pulses transmitted by other floats as well as surface/bottom re-

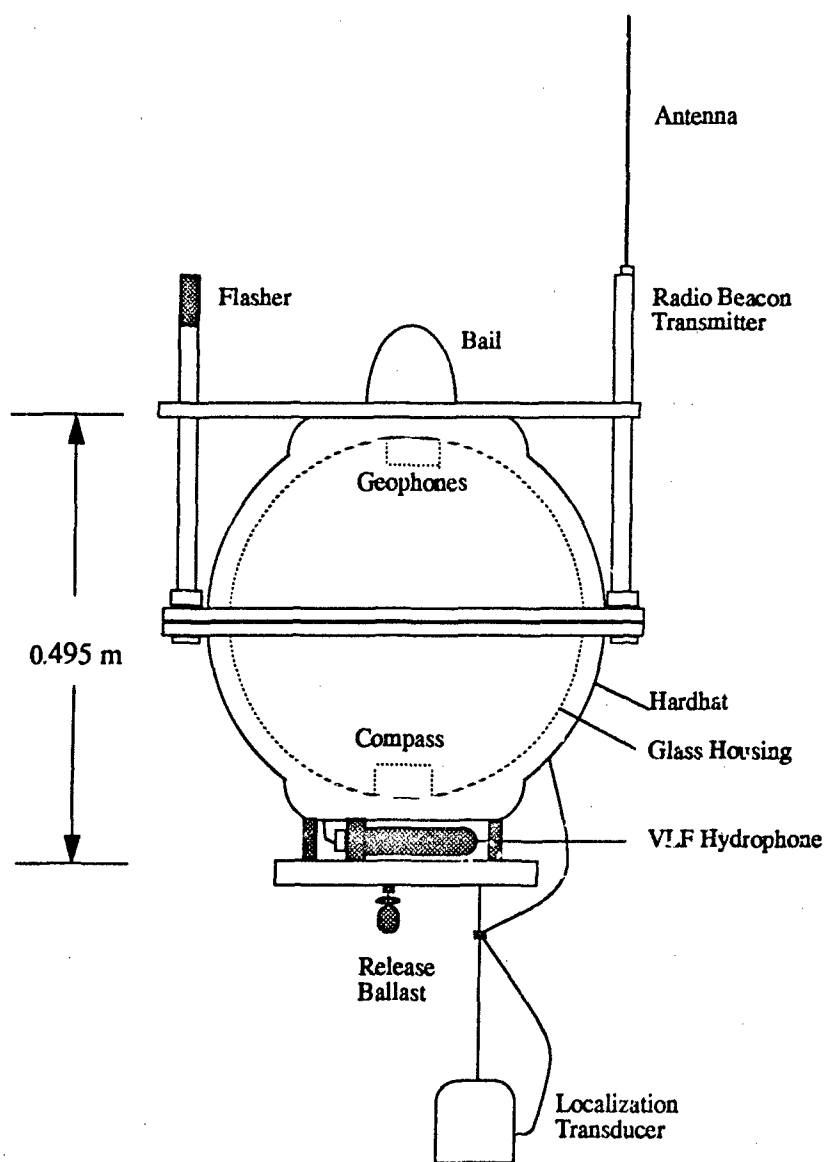


**Figure 2.1** Schematic drawing of a typical Swallow float.



flections of their own pulses. The interfloat and float-to-surface acoustic travel times can be used to localize the floats as well as to correct for float clock drift.

### 2.3 1989 Experiment Summary

The 12 Swallow floats were deployed for a 24-hour period on 8 - 9 July 1989 near 34° 50' N, 122° 20' W, about 150 km west, northwest of Pt. Arguello, California. The Swallow float deployment was a part of the Downslope Conversion experiment that has as its primary objective the study of the physics of downslope signal propagation.

Of the 12 floats, 9 were freely drifting in the water column, and 3 were tethered to the ocean bottom by 3.05-meter lines with 10- to 15- lb anchors. The three bottom-tethered floats were positioned at the corners of a triangle with sides about 6.3 km long in order to provide an absolute reference for the float localization. The nine midwater floats were deployed in a quasi-vertical line array geometry with a vertical float separation of about 400 m, starting at about 600-m depth to about 3800 m. The midwater floats were put into the water at about the geometric center of the bottom-float triangle. Figure 2.2 shows the Swallow float deployment geometry and retrieval positions of all 12 Swallow floats. The symbols used for plotting the float retrieval positions are the float identification numbers. Figures 2.3 shows the planned float deployment depths while Table 2.1 lists the planned and actual deployment depths of the Swallow floats. In this deployment, all

**Table 2.1** Planned and actual deployment depths, July 1989 experiment.

Float Number	Planned Deployment Depth (m)	Actual Achieved Depth (m)
0	500	560 - 580
1	900	995 - 1010
2	1300	1375 - 1395
3	1700	1660 - 1680
4	2100	2080 - 2100
5	2500	2495 - 2510
6	2900	2915 - 2940
7	3300	3350 - 3365
8	3700	3770 - 3780
9	bottom	4039
10	bottom	4051
11	bottom	4041

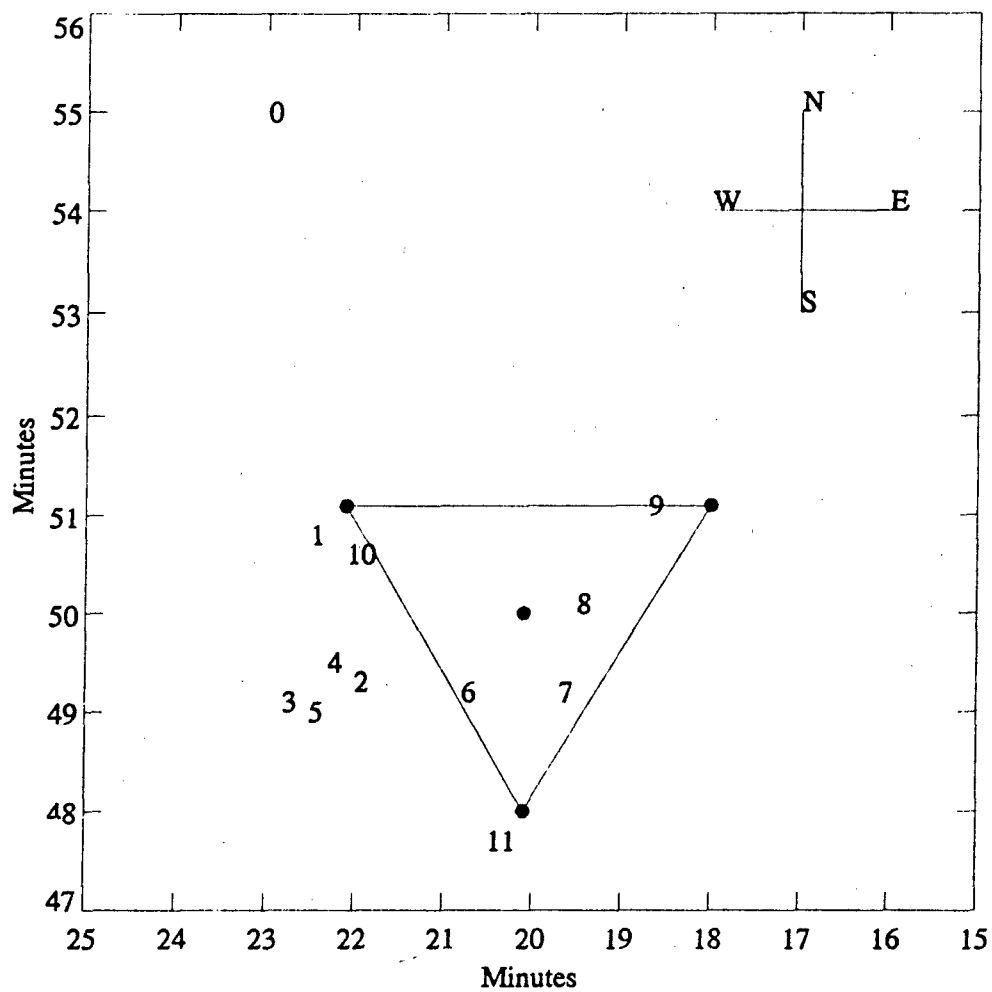
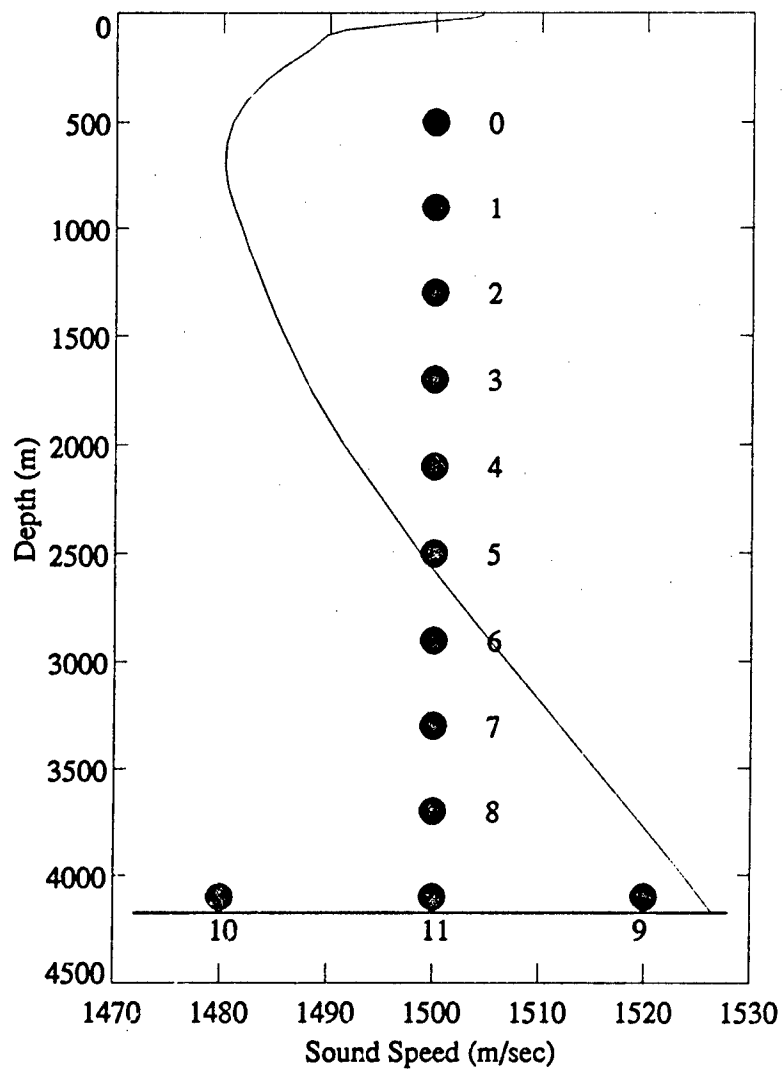


Figure 2.2 Swallow floats deployment geometry and float retrieval positions, July 1989, 34° N, 122° W.



**Figure 2.3** Planned Swallow float deployment depth. Also plotted in this figure is the sound speed profile based on historical temperature and salinity data.

12 floats that were taken on the trip were deployed, and all recorded full data tapes except float 4, which quit recording about 4 hours earlier than expected due to a cassette tape defect. Also, float 5's time release occurred at 08:00, 9 July, rather than at 08:00, 10 July, due to a programming error that caused the float to ascend back to the surface prematurely. In all, 95 percent of the potential number of records that could have been recorded by 12 properly functioning floats were recorded.

## 2.4 Data Description

### 2.4.1 8-KHz Range Data

As discussed in section 2.2, the floats transmit and receive 10-msec, 8-kHz pulses in order to measure interfloat and float-to-surface acoustic travel times. A given float receives pulses transmitted by other floats as well as its own arrivals (surface echoes, bottom bounces, or mixtures of both). Since only direct path pulses between floats and surface echo pulses from one float to itself are of interest, an edge detector program was used to detect and extract such pulses that correspond to the first arrivals in a narrow range time window [Hodgkiss and Anderson, 1983; Culver and Hodgkiss, 1988].

Figure 2.4 shows the leading edge of float 1's detection of its own surface echo 8-kHz pulses and pulses transmitted by other floats according to its own clock as a function of time during the July 1989 experiment. The vertical axis is converted from travel times in seconds to range (or depth) in meters, i.e., the direct pulses arrival times are converted to range by using a speed of sound of 1500 m/s and the self surface echo returns are converted to depth by using half of a speed of sound). The horizontal axis is time in units of Swallow float records. Each Swallow float record equals 45 seconds. The horizontal dotted line around 1000 m indicates the approximate depths at which float 1 stabilized.

### 2.4.2 Acoustic VLF Data

The power spectral estimates from data collected by float 1's hydrophone during records 1040 to 1680 (00:28 and 08:28 PST, 9 July 1989) are presented in Figure 2.5 in spectrogram format. The spectral estimates were made by dividing a 40.96-second piece of data, gotten from the 44 seconds of data in each record after skipping the first 3.04 seconds in order to reduce tape recorder contamination, into seven 512-point segments (each segment is 10.24 seconds long) with a 50 percent overlap between segments. The segments were Fourier transformed after being windowed with a Kaiser-Bessel window of  $\alpha = 2.5$ . The seven spectra were then incoherently averaged in order to reduce the variance of the power spectral estimates. Prominent features of this data set include

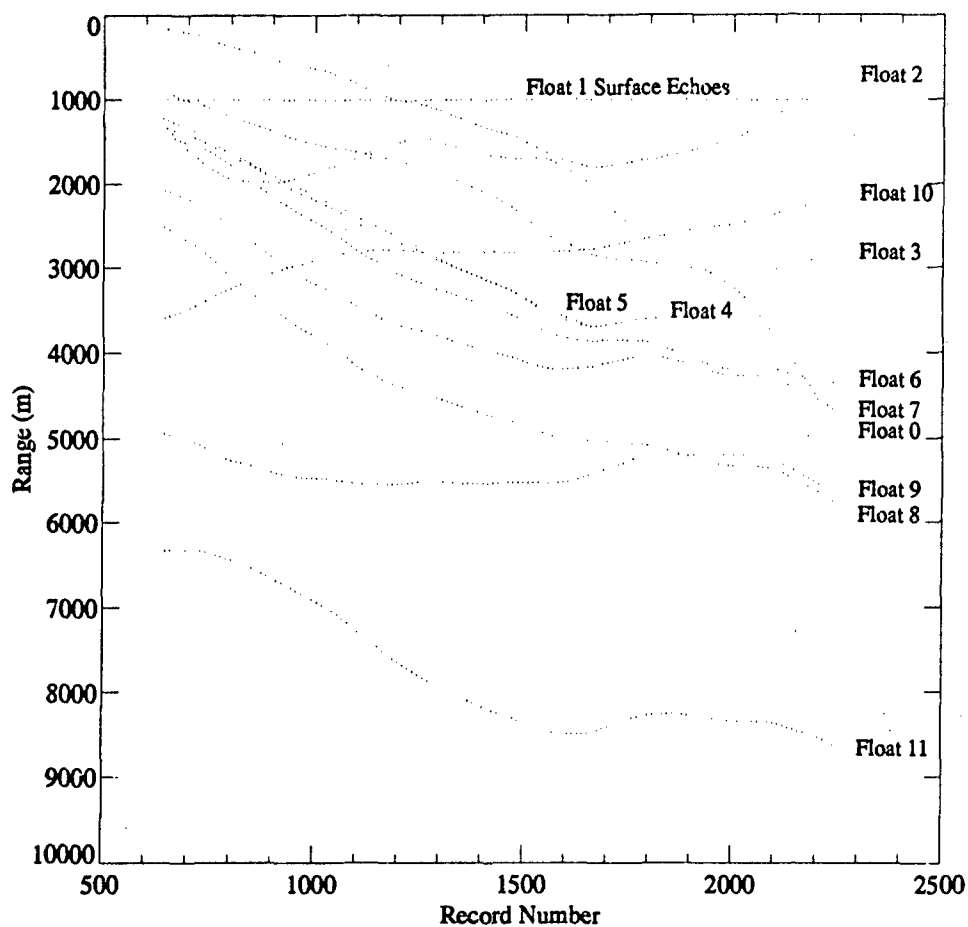


**Figure 2.4** 8-kHz acoustic range pulses received by float 1 (freely drifting) as a function of time during the July 1989 experiment. The horizontal axis of the figure gives the time in units of Swallow float record number. Eighty records represent 1 hour.

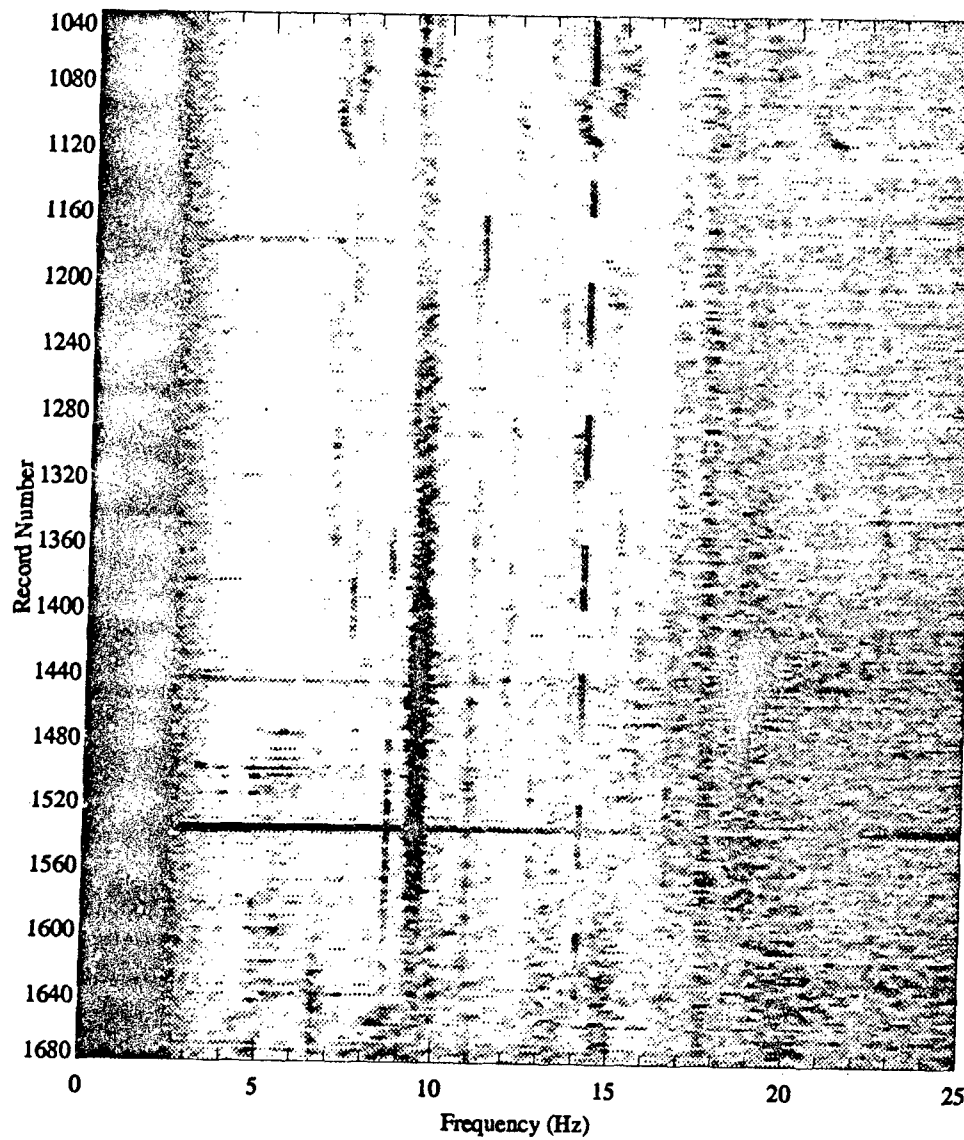


**Figure 2.5** VLF acoustic spectrogram of float 1, 00:28 - 08:28 PST, 9 July 1989. The vertical axis of the figure gives the time in units of Swallow float record number. Eighty records represent 1 hour.

1. **MARK VI Source Deployed from R/V Aloha:** As part of a companion experiment being conducted concurrently with the Swallow float deployment, a MARK VI source was towed at an average speed of 8 knots and at a depth of about 90 meters by the R/V Aloha. This source ship was located about 2500 km and 10° north of due west from the Swallow float array during their recording period. Figure 2.6 shows the MARK VI source relative to the Swallow float deployment site. The broadcast plan of the R/V Aloha was to transmit 14 Hz for a half-hour, then 8 Hz for a half-hour, then 14 Hz, then 11 Hz and then repeat the pattern. Three tonals in the Swallow float frequency band, at 8 Hz, 11 Hz, and 14 Hz, are visible that are believed to be generated by the MARK VI source. Evidently, the Swallow floats can see quite clearly the 14-Hz line projected by the MARK VI source and, at times, the 11-Hz and the 8-Hz lines.
2. **Earthquake:** Around record 1535 (06:39, 9 July) the Swallow float detected the local Richter magnitude 4.1 earthquake that occurred along the Calaveras fault in central California.
3. **Ship-Generated Signals:** Harmonic line sets broadcast by commercial ships, generated by cavitation resulting from the low pressure of the props that provide the ship's thrust, are a well-known contributor to the infrasonic sound field [Ross, 1976; D'Spain et. al., 1991]. The Swallow float deployment site, just west of the mouth of the Santa Barbara channel, is an area of very heavy shipping traffic. The 7-, 9.4-, and 18- to 19-Hz spectral lines are believed to be generated by surface ships.

### 2.4.3 Environmental Data

A large amount of environmental data was collected during the experiment [Olivera, 1990]. The swell was observed to be 10 to 13 feet in height, coming from 330° magnetic. The temperature was in the low sixties in Fahrenheit. The weather in this part of the ocean comes from the northwest, and the wind speed is around 10 to 15 knots.

Water temperature and salinity measurements, collected during the Downslope Conversion and a companion experiment, relevant to this study include (1) Twelve expendable bathythermograph (XBT) probes, launched near the Swallow float experiment site during 8 to 10 July, reached a depth of approximately 1800 meters; (2) One conductivity-temperature-depth measurement (CTD) was collected on 11 July 1989, at the center of the float-triangle where all the freely drifting floats were put into the water. The CTD station sampled from surface to bottom so that a complete sound speed profile for the entire water column could be obtained; (3) One CTD measurement to the depth of 2000 meters was made at 33° 48' N, 141° 03' W on 11 July 1989; and (4) 116 air-launched bathythermographs (AXBT), designed to reach a depth of 800 meters, were dropped by a P-3 aircraft between 8 - 10 July 1989, along the path between 32° N, 150° W and 35° N, 122° W as shown in Figure 2.6 marked with the Δ's. Figure 2.7 is the complete sum-

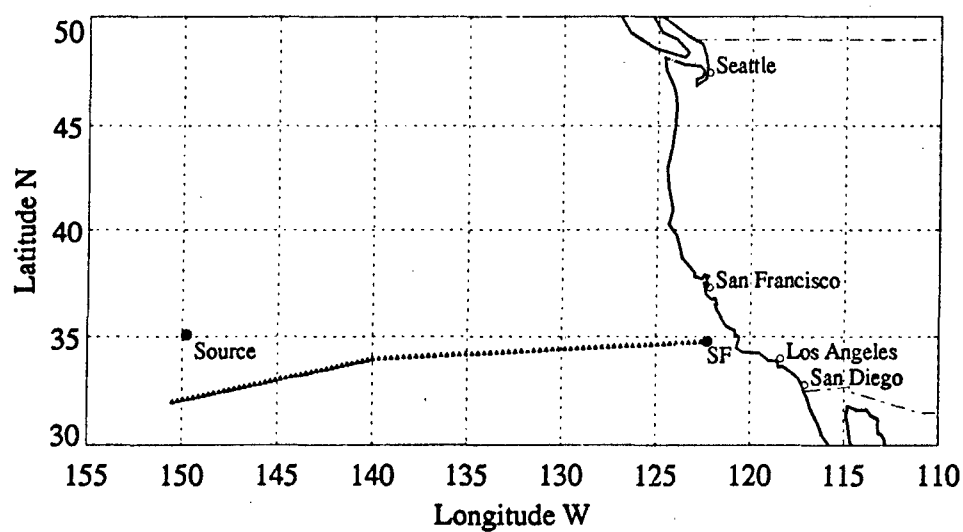
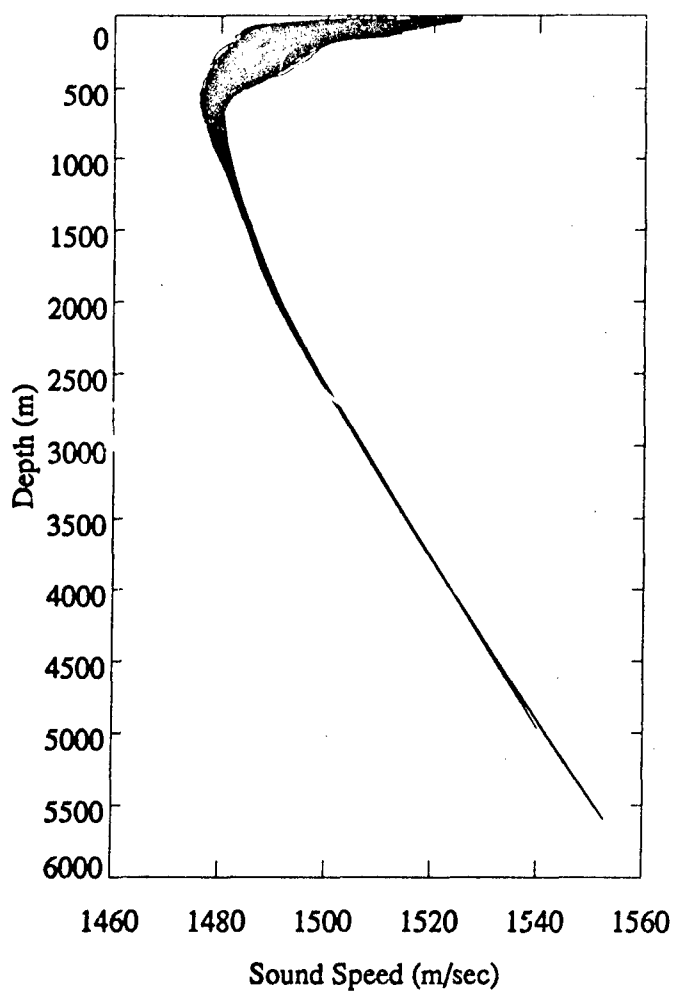


Figure 2.6 MARK VI source - Swallow float array geometry, 9 July 1989. The line of triangles marks the AXBT measurements taken between 8 - 10 July 1989.





**Figure 2.7** Sound speed profiles collected during the 1989 experiment.

mary of all sound speed profiles derived from the measurements taken by both the Downslope Conversion and a companion experiment during 8 - 11 July 1989.

## 2.5 Summary

This chapter described the Swallow float system and summarized the Swallow experiment conducted on 8 - 9 July 1989. MPL's 12 Swallow floats were deployed for a 24-hour period near  $34^{\circ} 50' \text{ N}$ ,  $122^{\circ} 20' \text{ W}$ , approximately 150 km west-northwest of Pt. Arguello, California. Of the 12 floats, 9 were freely drifting in the water column while 3 were anchored to the ocean bottom to provide an absolute reference for the float navigation. The freely drifting floats were deployed to span the water column of 4100-m depth with a vertical float separation of about 400 m, starting at about 600-m depth to about 3800 m. Data collected during the experiment included (1) range data: Floats transmitted and received 8-kHz pulses in a preprogrammed schedule to measure interfloat and float-to-surface travel times from which the float positions could be determined with a postprocessing float localization technique based on the least-squares method; (2) VLF acoustic data: Floats recorded acoustic data in the 1- to 25-Hz band. Of particular interest in the data set was a 14-Hz tonal generated by the MARK IV source deployed by the R/V Aloha, a source ship involved in a companion experiment located about 2500 km and  $10^{\circ}$  north of due west from the Swallow float array. The tonal was clearly heard by the floats through most of the experiment; and (3) environment data: A large volume of environmental data such as AXBT, XBT, and CTD measurements was collected between  $34^{\circ} 50' \text{ N}$ ,  $122^{\circ} 20' \text{ W}$  and  $32^{\circ} 00' \text{ N}$ ,  $150^{\circ} 00' \text{ W}$  during 8 - 10 July 1989.

### 3. SWALLOW FLOAT LOCALIZATION

#### 3.1 Introduction

The Swallow float array's geometry must be determined before the VLF acoustic data can be coherently combined to form a beamformer. As described in last chapter, the float transmits and receives 10-msec, 8-KHz pulses in a preprogrammed sequence to measure the interfloat and surface echo travel times. Figure 3.1 is a conceptual diagram depicting a realization of the geometry

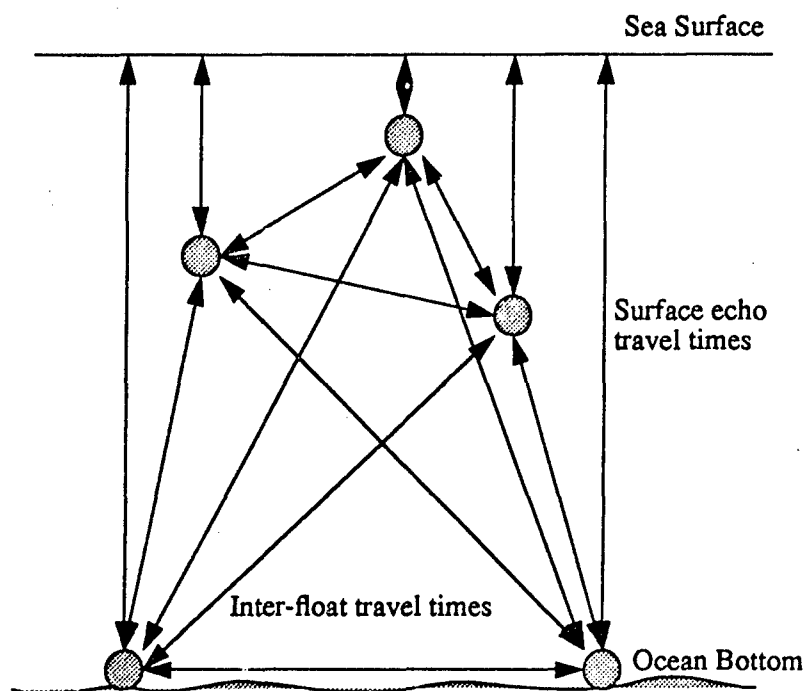


Figure 3.1 Swallow float array geometry conceptual diagram.

of the freely drifting array. The arrow lines represent the travel time measurements between two floats and the float-to-surface echoes, while the circles represent the Swallow floats. The focus of this chapter is to estimate the Swallow float array geometry in a 3-D coordinate system from the travel time measurements as a function of time during the July 1989 experiment.

This chapter is organized as follows. Following this introductory section, Section 3.2 reviews the theoretical basis for float localization techniques. The desire here is to provide the necessary background for discussion in the subsequent sections. Section 3.3 describes the inputs to the float localization filters, while Sections 3.4 and 3.5 discuss approaches to filter tuning and the outputs

from the filters, respectively. Lastly, a summary of the float localization results is given in Section 3.6. Detailed information about the float localization is documented in [Chen and Hodgkiss, 1990].

## 3.2 Float Localization Techniques

The function of the float localization filter is to algorithmically compute float positions from noisy range measurements in a statistical sense depending on the optimality criterion chosen. In this section, two such filters developed at MPL are reviewed from the performance criteria point of view.

### 3.2.1 Least-Squares Filter

The generalized (or weighted) least-squares filter [Gelb, 1974; Sorenson, 1980] involves using the current set of range measurements,  $Z_n$ , that are related to the set of float positions  $X_n$  by the expression

$$Z_n = h(X_n) + V_n \quad (\text{measurement model}) \quad (3.1)$$

where  $h$  is the nonlinear function that gives the ideal (noiseless) connection between the range measurements and the float positions, and  $V_n$  is the set of range measurement errors that are also known as the residuals. The least-squares method is concerned with determining the most probable set of float positions that are defined as the set of float positions that minimizes the weighted sum of the squares of the residuals:

$$\underset{X_n}{\text{minimize}} [Z_n - h(X_n)]^T W_n [Z_n - h(X_n)] \quad (3.2)$$

where  $W_n$  is the weighting matrix chosen as the inverse of the range covariance matrix  $R_n$ , defined as

$$E[V_n V_n^T] = R_n \delta_{nm} \quad (\text{measurement statistics}) \quad (3.3)$$

Thus, the least-squares filter estimates current float positions by using only the current set of measurements and an estimate of the measurement error statistics.

### 3.2.2 Kalman Filter

The Kalman filter [Gelb, 1974; Brown, 1983; Sorenson, 1985; Culver and Hodgkiss, 1988] attempts to estimate float positions better by taking advantage of the knowledge of float dynamics

and incorporating a fading memory of past data into the estimator structure. In addition to the measurement model (3.1) and statistics (3.3), the Kalman filter also uses the system model (float dynamics), the system statistics, and the initial conditions. The system model is given by

$$\mathbf{X}_n = \Phi \mathbf{X}_{n-1} + \Gamma \ddot{\mathbf{X}}_{n-1} \quad (\text{system model}) \quad (3.4)$$

where  $\Phi$  is the state transition matrix that relates  $\mathbf{X}_{n-1}$  to  $\mathbf{X}_n$ ,  $\Gamma$  is the matrix that relates the accelerations to the float positions, and  $\ddot{\mathbf{X}}_{n-1}$  is the set of accelerations with zero means and second-order statistics described by

$$\mathbf{E}[\ddot{\mathbf{X}}_n \ddot{\mathbf{X}}_m^T] = \mathbf{Q}_n \delta_{nm} \quad (\text{system statistics}) \quad (3.5)$$

The initial conditions are

$$\hat{\mathbf{X}}_0 = \mathbf{E}(\mathbf{X}_0) \quad (3.6)$$

$$\mathbf{P}_0 = \mathbf{E}[(\mathbf{X}_0 - \hat{\mathbf{X}}_0)(\mathbf{X}_0 - \hat{\mathbf{X}}_0)^T] \quad (3.7)$$

where  $\hat{\mathbf{X}}_0$  is the estimate of the initial float positions, and  $\mathbf{P}_0$  is the estimate of the error variance in the initial float positions.

The operation of the Kalman filter can be viewed as a predictor-corrector process [Candy, 1988]. First, suppose we have available to us the previous float position estimates  $\mathbf{X}_{n-1}$  and associated position covariance matrix  $\mathbf{P}_{n-1}$ :

$$\mathbf{P}_{n-1} = \mathbf{E}[(\mathbf{X}_{n-1} - \hat{\mathbf{X}}_{n-1})(\mathbf{X}_{n-1} - \hat{\mathbf{X}}_{n-1})^T] \quad (3.8)$$

and we would like to obtain the best estimate of the current float positions based on the previous estimate. We are in the "prediction phase" of the process. The system model (3.4) is used to predict the float positions and the associated position covariance matrix:

$$\hat{\mathbf{X}}_n(-) = \Phi \hat{\mathbf{X}}_{n-1} \quad (3.9)$$

$$\mathbf{P}_n(-) = \Phi \mathbf{P}_{n-1} \Phi^T + \Gamma \mathbf{Q} \Gamma^T \quad (3.10)$$

The "minus" is introduced here (following the notation in reference [Gelb, 1974]) as a reminder that this is our best estimate prior to incorporating the measurement. We now seek to use the measurement  $\mathbf{Z}_n$  to improve the estimate  $\hat{\mathbf{X}}_n(-)$ . We choose a linear blending of the noisy measurement and the  $\hat{\mathbf{X}}_n(-)$  in accordance with the equation:

$$\hat{X}_n = \hat{X}_n(-) + K_n [Z_n - h(\hat{X}_n(-))] \quad (3.11)$$

The optimal choice of  $K_n$ , the Kalman gain, is to minimize a scalar sum of the diagonal elements of the position covariance matrix  $P_n$ :

$$\underset{K_n}{\text{minimize}} \{ \text{trace} [P_n] \} \quad (3.12)$$

where

$$P_n = E \left[ (X_n - \hat{X}_{n-1}) (X_n - \hat{X}_{n-1})^T \right] \quad (3.13)$$

$K_n$  is obtained as

$$K_n = P_n(-) H_n^T [H_n P_n(-) H_n^T + R_n]^{-1} \quad (3.14)$$

or in a simpler form

$$K_n = P_n H_n^T R_n^{-1} \quad (3.15)$$

where

$$H_n = \left. \frac{\partial}{\partial X} h(X_n) \right|_{X_n = \hat{X}_n(-)} \quad (3.16)$$

We then use the current set of range measurements  $Z_n$  to determine the innovations. The innovation is defined as  $Z_n - h[\hat{X}_n(-)]$ , where  $h$  is the difference between the actual range measurement and the predicted range measurement (3.9). Now we enter the "correction phase" of the process. That is, we correct or update the predicted positions based on the new information in the range measurements -- the innovation. The innovation is weighted by the Kalman gain  $K_n$  to correct the predicted positions  $\hat{X}_n(-)$  as described in (3.11). The associated position covariance matrix (3.10) is corrected as well:

$$P_n = [I - K_n H_n] P_n(-) \quad (3.17)$$

The predictor-corrector process then repeats until all measurements are consumed.

A useful interpretation [Gelb, 1974] of the Kalman gain (3.15) is that the gain is "proportional" to the uncertainty in the position estimates, and "inversely proportional" to the range measurement noise. In other words, if the range measurement errors are large and the predicted position

errors are small, the innovation is due chiefly to the noise, and only a small change in the predicted positions should be made. On the other hand, small measurement noise and large uncertainty in the position estimates suggest that the innovation contains considerable information about errors in the position estimates. Therefore, the difference between the actual and the predicted range measurement will be used as a basis for strong corrections to the position estimates.

In short, the Kalman filter estimates float positions by weighting a current set of measurements against previous position estimates propagated forward in time using an equation of motion. Thus, the Kalman filter uses all of the following: current measurements as well as past measurements in a fading memory fashion, estimates of the measurement error statistics and acceleration error (process noise) statistics, and the float dynamics. It has been shown [Culver and Hodgkiss, 1988] that the Kalman filter outperforms the least-squares filter in the presence of high measurement noise and when the process noise is low because of its ability to track float motion and effectively smooth noisy measurements.

### **3.3 Inputs to the Localization Filter**

This section presents the inputs to both filters using data from the July 1989 experiment. Based on the discussion in the previous section, input data fall under four categories: measurement data, measurement statistics, initial estimates, and process noise.

#### **3.3.1 Measurement Data**

Range measurements used by the filters are derived quantities computed from the 8-kHz pulse travel time measurements between floats (or from float to surface) using an estimate of the sound speed. Thus, measurement data include travel time estimates and sound speed estimates.

##### **3.3.1.1 Travel Time Estimates**

Measurement of pulse travel times has received a great deal of attention during the process of the Swallow float system development in the past few years. References [Hodgkiss and Anderson, 1983; Culver et. al., 1989] have addressed this subject in detail. In brief, each float is equipped with an acoustic transducer that transmits and receives 8-kHz pulses. Pulses are transmitted by the floats in a preprogrammed sequence. A different float transmits every 45 seconds; 12 floats were deployed in this experiment, and each float transmits every 9 minutes. A given float receives pulses transmitted by other floats as well as its own arrivals (surface echoes, bottom bounces, or mixtures of both). Since only direct path pulses between floats and surface echo pulses from one float to itself are of interest, an edge detector program was used to detect and extract such pulses that correspond to the first arrivals in a narrow range time window.

Surface echo travel time measurements are obtained by subtracting outgoing pulse transmit times from pulse arrival times, whereas interfloat travel time measurements are obtained by subtracting pulse transmit time according to the transmitting float from pulse arrival times at the receiving float. Since two time bases are involved, interfloat travel time measurements contain a bias due to variation in the float clock rates. It has been shown [Culver and Hodgkiss, 1989] that the bias can be reduced significantly by averaging reciprocal path interfloat travel time measurements. Because interfloat measurements were not made simultaneously, travel time measurements must be interpolated by a factor of 12 before reciprocal path measurements may be averaged.

Figures 3.2 and 3.3 show the typical direct path pulse detections between two freely drifting floats (2 and 8) whereas Figure 3.4 shows the interfloat travel time estimates calculated by averaging interpolated reciprocal path measurements. Figure 3.5 shows the leading edge of each float's detection of its own transmitted and surface echo 8-kHz pulses. The vertical axis in the figure has been scaled from travel time to depth, using half of 1500 m/s for sound speed. The lines of dots correspond to each float's detection of the incoming pulses, i.e., surface echo pulses. Note in Figure 3.5 that the lines of dots for floats 4 and 5 terminate prematurely. This is due to the fact that float 4 stopped recording data 4 hours too early, and float 5's automatic ballast release time was set incorrectly (as indicated in section 2.3). Figure 3.6 is the enlarged version of the surface echo travel time measurements for the bottom float 9. As pointed out in [Culver and Hodgkiss, 1989], the bottomed floats' surface measurements like these are expected to be approximately constant because the floats themselves are approximately stationary; they are tethered to the ocean bottom by 3.05-meter lines. Noise in the surface echo pulse arrival time is thought to be caused by scattering of the pulse at the rough, moving sea surface and destructive interference among multiple arrivals at the receiver. Since filter performance can be improved by substituting a constant for the actual measurements, the most probable value, i.e., the mode of the travel time measurements as shown in Figure 3.7 (5.402 seconds for float 9; 5.422 seconds for float 10; and 5.404 seconds for float 11) will be used as the travel time estimates. Table 3.1 lists the modes of the surface echo travel time estimates for the bottomed floats.

**Table 3.1** Surface echo travel time estimates for bottomed floats.

Float Number	Surface Echo Estimate (msec)
9	5402
10	5422
11	5404



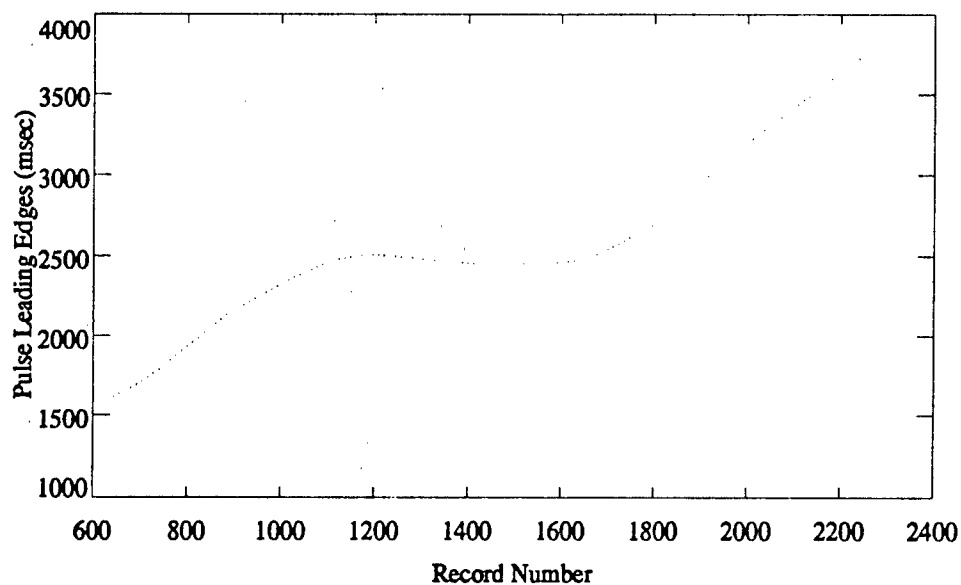


**Figure 3.2** Float 2 listening to float 8, July 1989 experiment. The horizontal axis of the figure gives the time in units of Swallow float record number. Eighty records represent 1 hour.

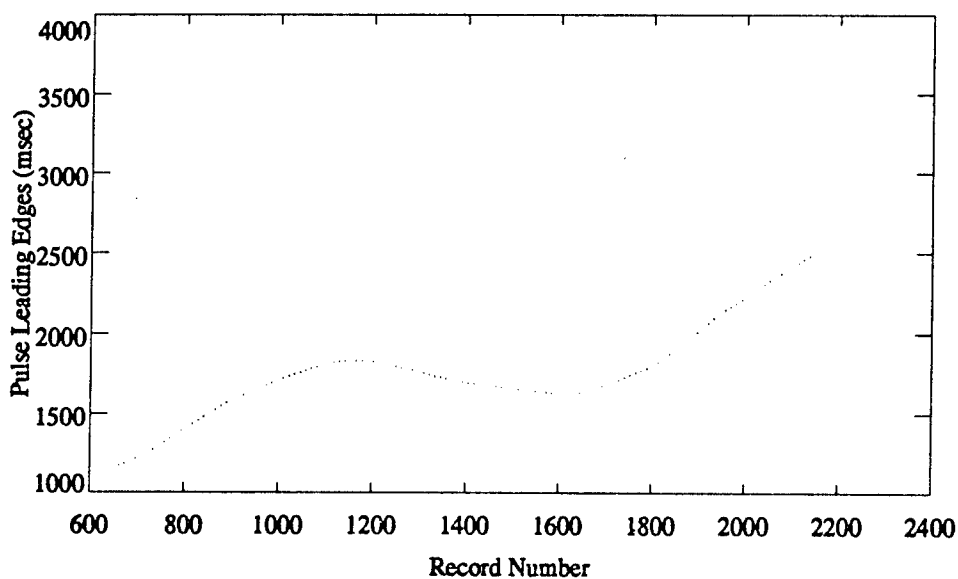


**Figure 3.3** Float 8 listening to float 2, July 1989 experiment. The horizontal axis of the figure gives the time in units of Swallow float record number. Eighty records represent 1 hour.

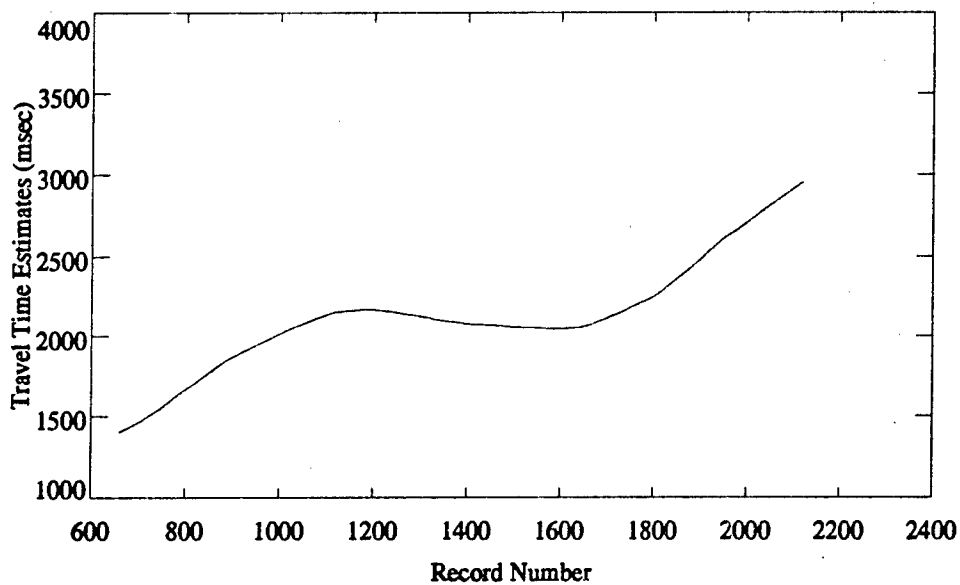


**Figure 3.4** Travel time estimates between two freely drifting floats (2 and 8). The horizontal axis of the figure gives the time in units of Swallow float record number. Eighty records represent 1 hour.

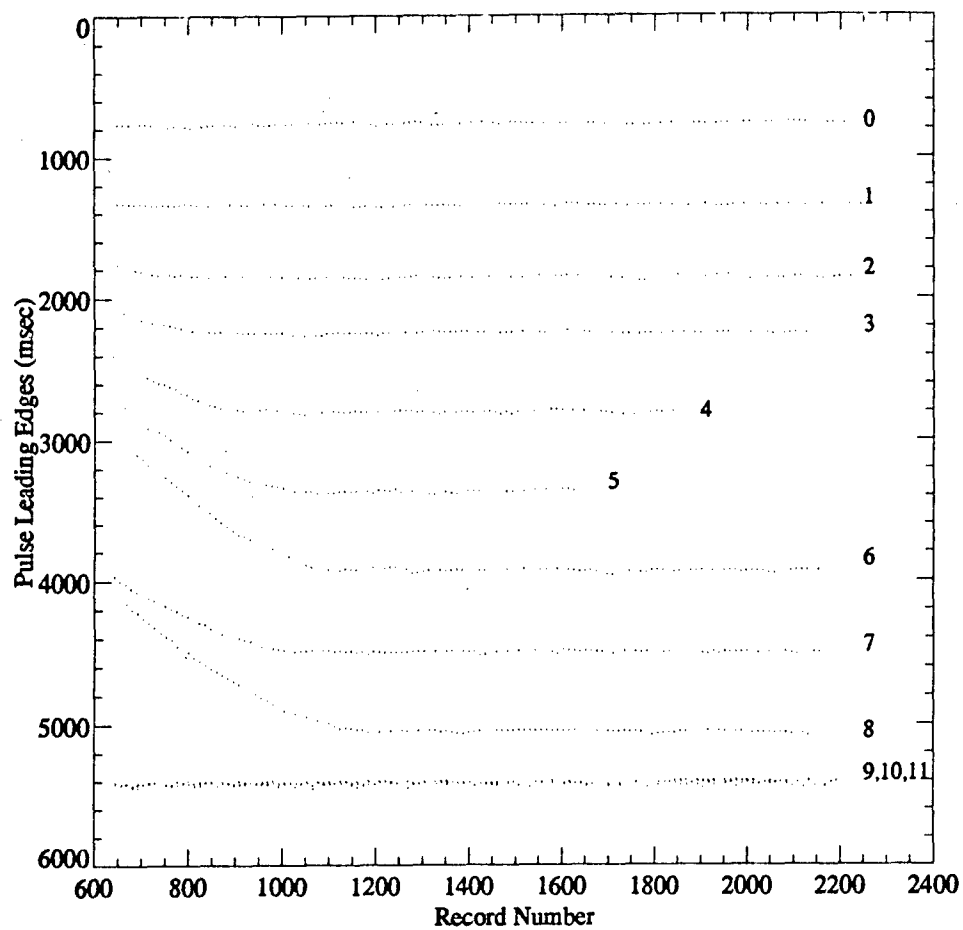


**Figure 3.5** Leading edges of each float's detection of its own surface echo pulses. The horizontal axis of the figure gives the time in units of Swallow float record number. Eighty records represent 1 hour.

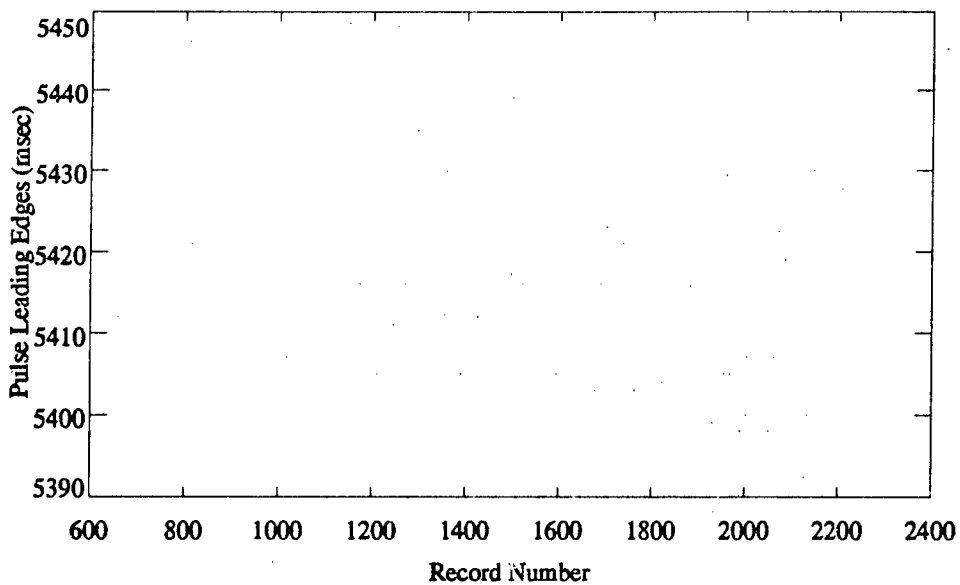


**Figure 3.6** Float 11 surface echo pulses, July 1989 experiment. The horizontal axis of the figure gives the time in units of Swallow float record number. Eighty records represent 1 hour.

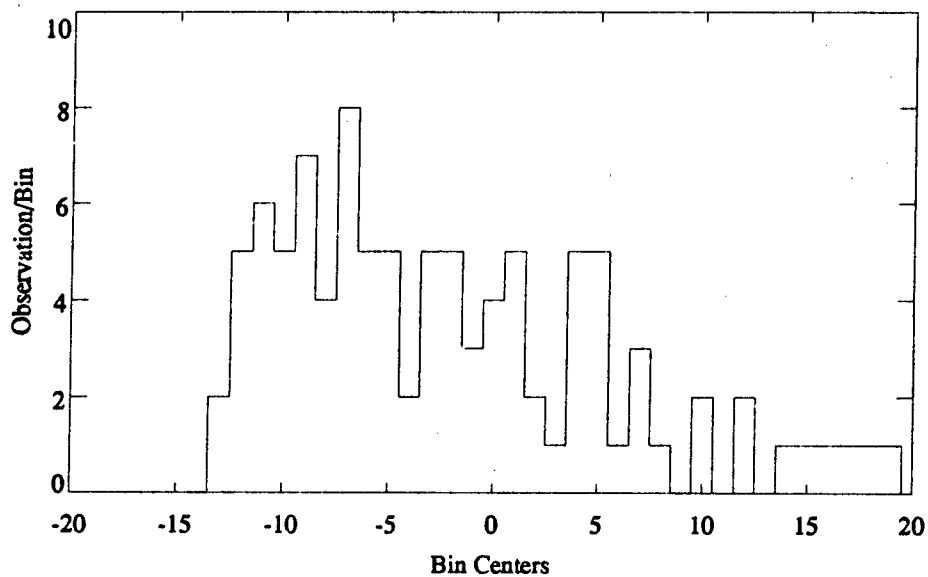


**Figure 3.7** Histogram of float 11 surface echoes minus the mean 5411 msec (binwidth is one msec), July 1989 experiment.

Figures 3.8 and 3.9 show the surface reflected pulse detections between the bottomed floats, 9 and 11. The direct path pulses between the bottomed floats were not detected because the sound speed gradient bends nearly all of the sound energy upward over the 6.3-km distance that separates the floats. Direct path travel times can be calculated from surface reflection travel times [Culver and Hodgkiss, 1989]:

$$[\tau_{ij}^n]_{\text{direct path}}^2 = \frac{c_{\text{hmss}}^2}{c_{ij}^2} \left[ [\tau_{ij}^n]_{\text{surface reflection}}^2 - \tau_{ii}\tau_{jj} \right] \quad (3.18)$$

where  $\tau_{ij}^n$  is the interfloat travel time,  $\tau_{ii}$  and  $\tau_{jj}$  are the individual float surface echo travel times,  $c_{\text{hmss}}$  is the harmonic mean sound speed [Polvani, 1984] for a vertical path from the surface to the bottom, and  $c_{ij}$  is the sound speed at the depth of floats  $i$  and  $j$ .

Like the bottom float surface echo travel times, the interfloat travel time between two bottom floats should be approximately constant because the floats are approximately stationary. Figure 3.10 shows the direct path travel time estimates, calculated using equation (3.18) and the constant value (mode) estimates of the averaged interpolated reciprocal surface reflection travel times between the bottom floats 9 and 10. Because the underlying direct path travel time must be approximately constant, the modes of the direct path travel time estimates will be used as the direct path travel times estimates as shown in Figure 3.11. Table 3.2 lists the modes of the direct path travel times between the bottomed float pairs.

**Table 3.2** Direct path travel time estimates between bottomed floats.

Float Path	Direct Path Estimate (msec)
9-10	4025
9-11	4157
10-11	4132

### 3.3.1.2 Sound Speed Estimates

The sound speed profile for the upper 1000 meters was derived from five expendable bathythermograph (XBT) measurements made from the R/V New Horizon near the deployment site. The measurements were made at various times during the Swallow float experiment and historical salinity data archived by the National Oceanographic Data Center [Churgin and Halminski, 1974] for area 24, 3rd quarter of the year, in the upper 1000 meters were used in deriving the sound speed profiles. The sound speed profile for the lower 3100 meters was obtained from a con-

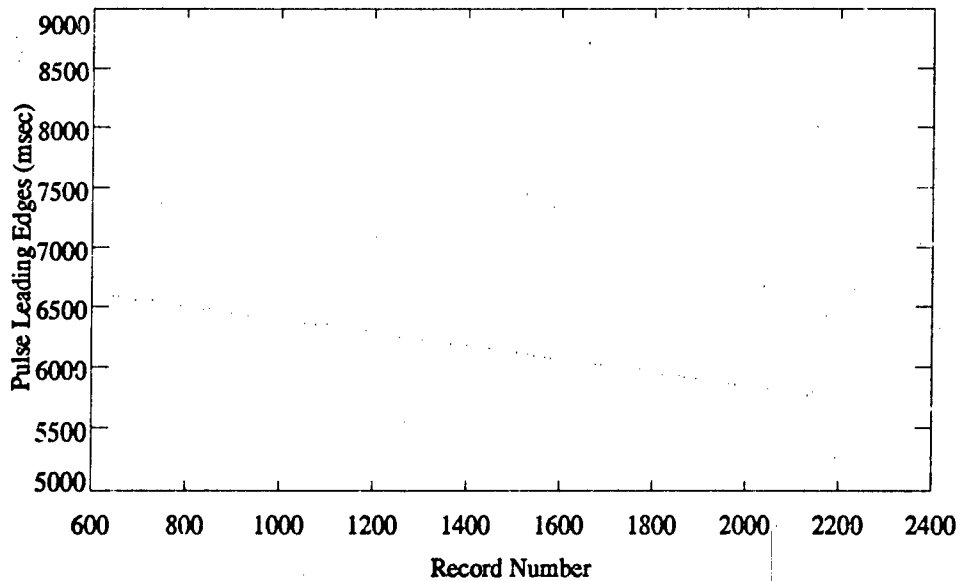


**Figure 3.8** Float 9 listening to float 11, July 1989 experiment. The horizontal axis of the figure gives the time in units of Swallow float record number. Eighty records represent 1 hour.

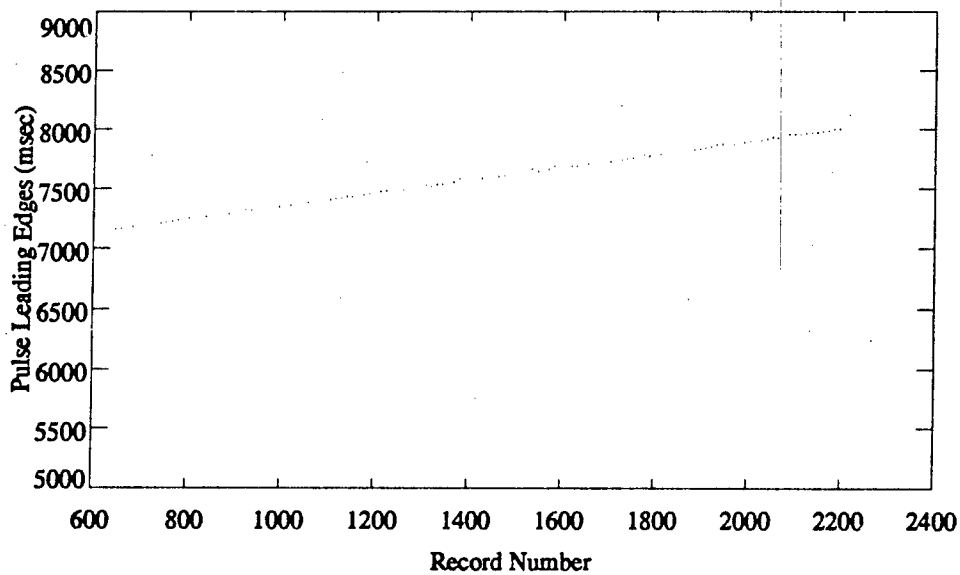


**Figure 3.9** Float 11 listening to float 9, July 1989 experiment. The horizontal axis of the figure gives the time in units of Swallow float record number. Eighty records represent 1 hour.

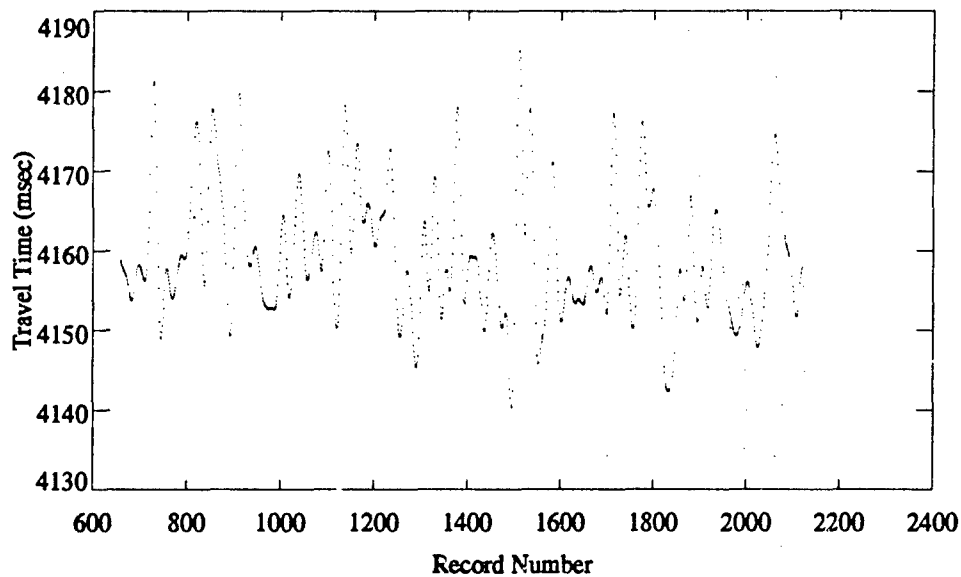


**Figure 3.10** Direct path travel time estimates between bottomed floats 9 and 11, calculated using constant mode values of surface echo travel times, July 1989 experiment. The horizontal axis of the figure gives the time in units of Swallow float record number. Eighty records represent 1 hour.

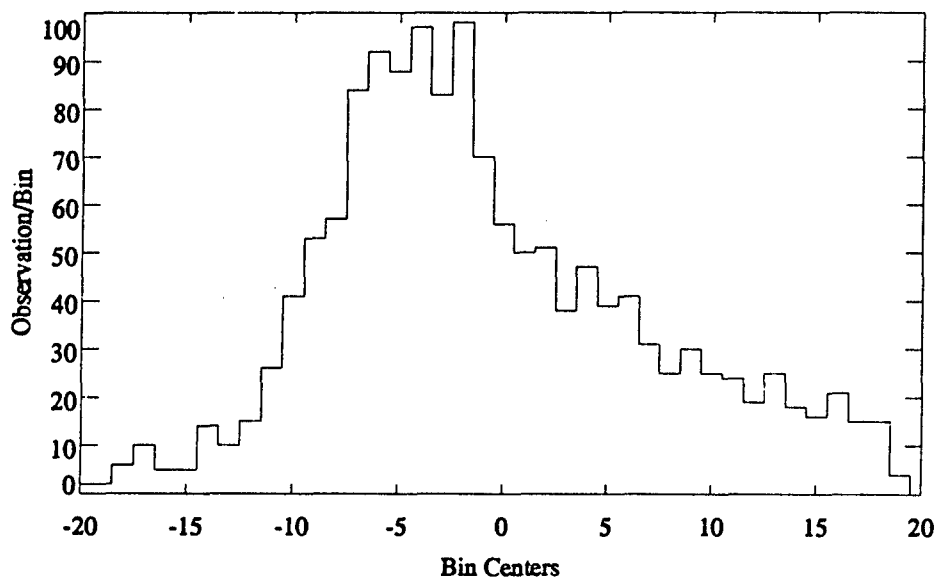


**Figure 3.11** Histogram of direct path travel time estimates minus the mean 4159 msec (binwidth is one msec), July 1989 experiment.

ductivity-temperature-depth CTD station [Olivera, 1990] carried out on July 11, 1989, near the center of the float-triangle where all the freely drifting floats were put into the water. Using the equation given by Mackenzie [Mackenzie, 1981], the composite sound speed profile was calculated. Harmonic mean sound speeds for each interfloat and float to surface path were also calculated and are given in Appendix A.

### 3.3.2 Measurement Statistics

The measurement error variance estimates are used to weight the measurements so that greater weight is given to measurements with a smaller error variance. Since travel time measurement error and sound speed estimate error are assumed to be uncorrelated, the measurement error variance for float pair  $ij$  can be expressed as [Culver, 1988]:

$$\sigma_{r_{ij}}^2 = (\hat{\tau}_{ij}^n)^2 \sigma_{c_{ij}}^2 + (\hat{c}_{ij})^2 \sigma_{\tau_{ij}}^2 \quad (3.19)$$

where  $\hat{\tau}_{ij}^n$  is the estimated travel time between float  $i$  and  $j$ ,  $\sigma_{c_{ij}}^2$  is the sound speed error variance in  $\hat{c}_{ij}$ ,  $\hat{c}_{ij}$  is the estimated harmonic sound speed between float  $i$  and  $j$ , and  $\sigma_{\tau_{ij}}^2$  is the travel time error variance between float  $i$  and  $j$ .

#### 3.3.2.1 Travel Time Variances

It has been shown [Culver et. al., 1989] that the variance of a bottomed float's surface echo travel time measurements can be used as an estimate of the variance of the measurement error, because the true surface echo times are approximately constant. Subtracting the means from the surface echo travel time estimates produces estimates of the travel time estimate errors. The variances of the error time series are given in Table 3.3.

**Table 3.3** Estimated variance of bottomed float travel time, July 1989 experiment.

Float Number	Float Number	Variance (msec <sup>2</sup> )
9	9	115
10	10	110
11	11	97
9	10	78
9	11	64
10	11	142



In the previous section, the bottomed float surface echo travel time measurements were ruled too noisy to be used directly in estimating the float positions, and the mode of the travel time measurements was taken as the travel time estimate. The variance of the error in the constant estimate (mode) is expected to be much smaller than the variance of the error in the measurement. Based upon the predicted maximum vertical movement of a tethered bottom float and wave height in the sea surface during the deployment (about 3 meters), the error in the mode is taken to be mean zero and to have a variance of  $6 \text{ msec}^2$ . By the same token, the interfloat travel time variance is taken to be  $4 \text{ msec}^2$  [Culver and Hodgkiss, 1989] based upon the predicted maximum horizontal movement of a bottom float. Table 3.4 summarizes the estimated error variances of the bottomed float travel time estimates.

**Table 3.4** Estimated variance of bottomed float travel time based on predicted float movement, July 1989 experiment.

Float Number	Float Number	Variance, $\text{msec}^2$
9	9	6
10	10	6
11	11	6
9	10	4
9	11	4
10	11	4

The surface echo travel time estimate error for the freely drifting floats cannot be estimated directly. Because these floats were deployed shallower than the bottom floats, their variances are expected to be lower than the values in Table 3.3 but higher than those in Table 3.4. An arbitrary, yet logical choice of error variances for the freely drifting float surface echo travel time estimates is listed in Table 3.5.

Travel time error variance for float pairs in which one of the floats is not stationary can be estimated from the difference between reciprocal path travel time measurements [Culver et. al., 1989]. The difference in clock rates causes the travel time difference to be a linear function of time. The difference also appears to contain second-order time dependence due to the difference in clock accelerations. Subtracting a second-order fit from the travel time difference produces an estimate of the error in the travel time estimates. Figures 3.12 and 3.13 contain the interfloat travel time differences for floats 2 and 8 along with second-order curves fitted to the differences and the corresponding error estimate time series. The variances of the error time series for all float pairs are summarized in Appendix B.

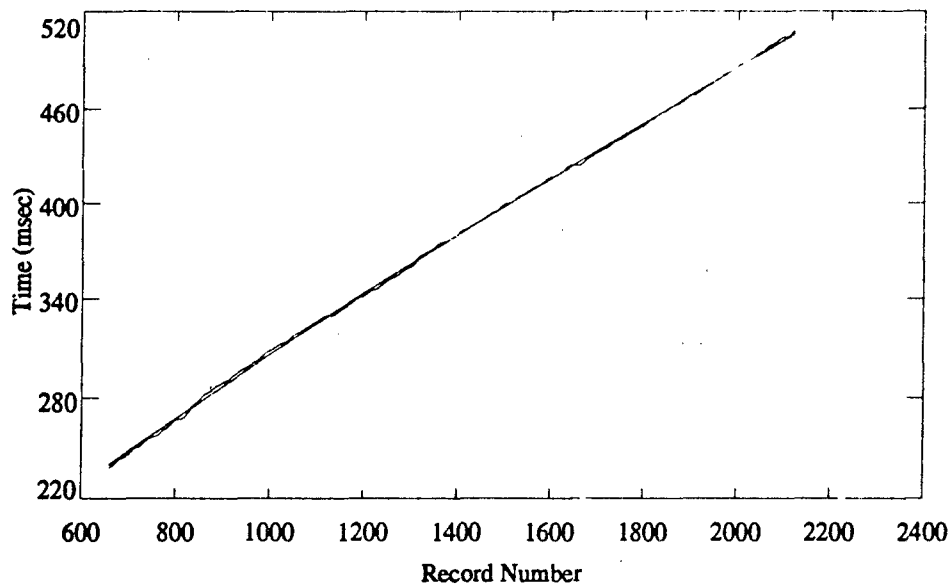


**Figure 3.12** Travel time difference between floats 2 and 8 and a second-order fit, July 1989 experiment. The horizontal axis of the figure gives the time in units of Swallow float record number. Eighty records represent 1 hour.

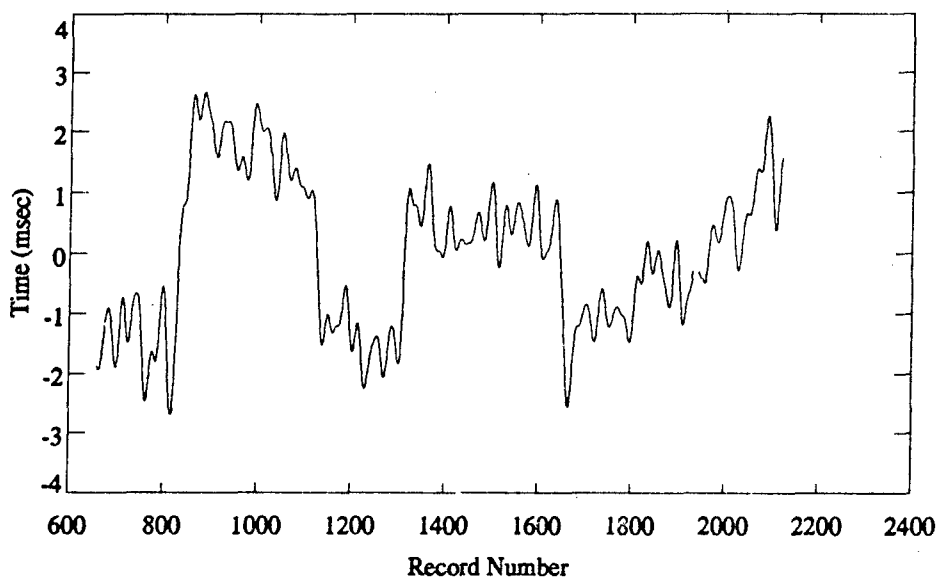


**Figure 3.13** Travel time difference (floats 2 and 8) minus second-order fit, July 1989 experiment. The horizontal axis of the figure gives the time in units of Swallow float record number. Eighty records represent 1 hour.

**Table 3.5** Estimated variance of freely drifting float travel time, July 1989 experiment.

Float Numbers	Float Number	Variance, msec <sup>2</sup>
0	0	6
1	1	10
2	2	20
3	3	30
4	4	40
5	5	50
6	6	60
7	7	70
8	8	80

### 3.3.2.2 Sound Speed Variances

It has been shown [Culver, 1988; Culver and Hodgkiss, 1989] that the variance of the sound speed estimate at a particular depth is just under  $0.4 \text{ (meter/sec)}^2$  in the North Pacific Ocean. The variance of the harmonic mean sound speed for a given path would be expected to be less than that in the sound speed at a particular depth due to the averaging effect. The error in the harmonic mean sound speed is estimated to be  $0.1 \text{ (meter/sec)}^2$  for the 1989 experiment.

### 3.3.3 Initial Estimates

The MPL implementation of the filters requires an initial estimate of the float positions. Additionally, the Kalman filter requires an initial estimate of the float velocities and the initial position and velocity variance estimates. Before estimating the initial positions, we must first define a coordinate system. The coordinate system for the float localization is established in which the origin lies at the surface directly above float 9. The Z axis is vertical, positive downwards and extends through float 9, and the X axis is oriented such that float 10 lies in the XZ plane. The positions of floats 9, 10, and 11 are taken to be the ship's position when the floats were launched into the water. Figure 3.14 shows a plane view of the coordinate system. The locations of the freely drifting floats will be estimated relative to these axes.

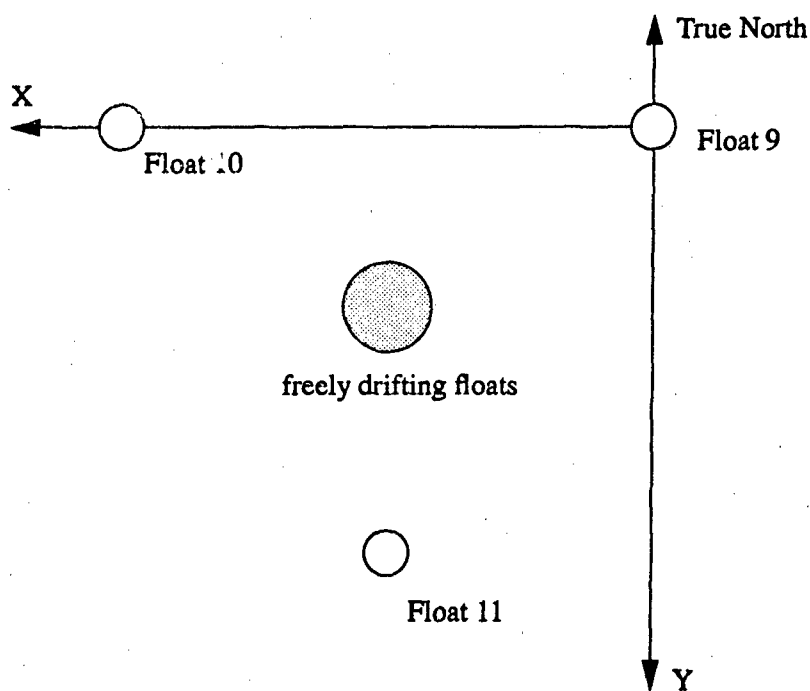


**Figure 3.14** Plane view of coordinate system used for float localization.

### 3.3.3.1 Initial Position Estimates

The time for the initial float position chosen for float localization is record 1003, 00:00 July 9 1989, at which seven of the nine freely drifting floats had reached equilibrium depth. The MPL implementation of the least-squares filter requires a rough initial-position estimate to bootstrap the filter. Using depths taken from Figure 3.5, we estimated the rough initial positions to be the ship's position relative to the coordinate system when the floats were launched into the water. Table 3.6 lists the rough initial-position estimate.

**Table 3.6** Rough initial-position estimate, record 1003, 00:00 July 9 1989.

Float Number	X (meters)	Y (meters)	Z (meters)
9	0	0	4050
10	6150	0	4050
11	3075	5500	4050
0	3075	2750	570
1	3075	2750	990
2	3075	2750	1380
3	3075	2750	1670
4	3075	2750	2080
5	3075	2750	2490
6	3075	2750	2840
7	3075	2750	3350
8	3075	2750	3650

Using the rough-initial position estimates in Table 3.6; the travel time estimates for record 1003; the travel time variance estimates given in Tables 3.4, and 3.5, and Appendix B; and the sound speeds and sound speed variances given in Appendix A, the least-squares filter produced the position estimate given in Table 3.7. It has a root mean squared (rms) residual of 2.67 meters. Since an initial-position estimate is determined to be satisfactory when the least-squares filter converges to a position estimate that results in an rms residual of less than 7.5 meters [Culver and Hodgkiss, 1989], the position estimate at record 1003 is taken as a good initial-position estimate and will be used by the Kalman filter.

### 3.3.3.2 Initial Velocity Estimates

Using the good initial-position estimates, the least-squares filter was again run for the first 13 records (9-minute period) from records 1003 to 1015. The position estimates produced by the filter were used to calculate the position change rates, i.e.,  $(X_{n+1} - X_n) / 45$  meters/second. Twelve such successive position change rates were then averaged to produce the initial velocity estimates. Table 3.8 lists the velocity estimates for record 1003, 00:00, 9 July 1989.

**Table 3.7** Initial-position estimate produced by the least-squares filter for record 1003, 00:00, July 9 1989.

Float Number	X (meters)	Y (meters)	Z (meters)
9	0	0	4039
10	6131	0	4051
11	3103	5518	4041
0	3779	-1456	574
1	4887	82	999
2	3885	162	1380
3	4425	969	1674
4	4110	1398	2081
5	4092	1482	2489
6	3870	1754	2841
7	2875	2085	3353
8	2824	1871	3650

**Table 3.8** Initial velocity estimate (in meters/second), record 1003, 00:00, July 1989 experiment.

Float Number	X (m/s)	Y (m/s)	Z (m/s)
9	0.0	0.0	0.0
10	0.0	0.0	0.0
11	0.0	0.0	0.0
0	0.061	-0.040	-0.004
1	0.025	-0.058	0.005
2	-0.015	-0.040	0.001
3	0.028	-0.027	0.006
4	0.003	0.001	0.013
5	-0.003	0.001	0.015
6	0.002	0.017	0.027
7	-0.010	0.021	0.005
8	-0.036	-0.003	0.025

### 3.3.3.3 Initial Position and Velocity Variance Estimates

The estimate of the variances in the initial positions and velocities is also needed by the Kalman filter. The estimate suggested by [Culver and Hodgkiss, 1989] will be used and is listed in Table 3.9.

The last piece of information required by the Kalman filter is the float acceleration variance, also known as the process noise, described in equation (3.5). The process noise is a parameter used by the Kalman filter to determine how much weight to give to its own track of the float relative to the measurements. When the model (i.e., filter) process noise matches the true process noise experienced by the float during the experiment, the Kalman filter is performing optimally and will have more estimates falling inside the predefined confidence interval [Bar-Shalom and Fortman, 1988]. However, there is no easy way of estimating the true process noise. One approach suggested by [Culver and Hodgkiss, 1989] is to run the filter several times, each time with a different process noise value, and the one that minimizes the innovation power will be selected as the candidate. We will use this matched processing technique with values ranging from  $10^{-12}$  to  $5 \times 10^{-8}$  (meter/second<sup>2</sup>)<sup>2</sup> in search of the true process noise.

**Table 3.9** Estimate of initial position and velocity variance used by the Kalman filter, July 1989 experiment.

Float Number	Pos. Var. X (m <sup>2</sup> )	Pos. Var. Y (m <sup>2</sup> )	Pos. Var. Z (m <sup>2</sup> )	Vel. Var. X (m/sec) <sup>2</sup>	Vel. Var. Y (m/sec) <sup>2</sup>	Vel. Var. Z (m/sec) <sup>2</sup>
9	0.0	0.0	0.01	0.0	0.0	0.0
10	0.01	0.0	0.01	0.0	0.0	0.0
11	0.01	0.01	0.01	0.0	0.0	0.0
0	0.01	0.01	0.01	0.0001	0.0001	0.00001
1	0.01	0.01	0.01	0.0001	0.0001	0.00001
2	0.01	0.01	0.01	0.0001	0.0001	0.00001
3	0.01	0.01	0.01	0.0001	0.0001	0.00001
4	0.01	0.01	0.01	0.0001	0.0001	0.00001
5	0.01	0.01	0.01	0.0001	0.0001	0.00001
6	0.01	0.01	0.01	0.0001	0.0001	0.00001
7	0.01	0.01	0.01	0.0001	0.0001	0.00001
8	0.01	0.01	0.01	0.0001	0.0001	0.00001

### 3.4 Filter Tuning

#### 3.4.1 Least-Squares Filter

Using the good initial positions given in Table 3.7, the sound speeds and sound speed variances given in Appendix 1, the travel time estimates for records 1003 to 2120, and the travel time variances given in Tables 3.4 and 3.5 and Appendix 2, the least-squares filter produced position estimates with an average rms of 2.7 meters. The residual is low and indicates that the position estimate is acceptable. However, a close inspection of the residual sequences  $[Z_n - h(X_n)]$  reveals that

$$E[z_{\text{direct path between 9 \& 10}} - h(x_{\text{direct path between 9 \& 10}}^n)] = 1.3 \text{ meters} \quad (3.20)$$

$$E[z_{\text{direct path between 9 \& 11}} - h(x_{\text{direct path between 9 \& 11}}^n)] = 3.0 \text{ meters} \quad (3.21)$$

$$E[z_{\text{direct path between 10 \& 11}} - h(x_{\text{direct path between 10 \& 11}}^n)] = 1.2 \text{ meters} \quad (3.22)$$

$$E[z_{\text{float 9 surface echo}} - h(x_{\text{float 9 surface echo}}^n)] = 1.5 \text{ meters} \quad (3.23)$$

$$E[z_{\text{float 10 surface echo}} - h(x_{\text{float 10 surface echo}}^n)] = 4.9 \text{ meters} \quad (3.24)$$

$$E[z_{\text{float 11 surface echo}} - h(x_{\text{float 11 surface echo}}^n)] = 0.6 \text{ meters} \quad (3.25)$$

By definition, residuals in the measurement model are to be mean zero:

$$E[V_n] = E[Z_n - h(X_n)] = 0 \quad (3.26)$$

The bias contained in the residual sequences (3.20) - (3.25) is an indication that the mode values selected as the travel time estimates may not be the optimal choice for the July 1989 data set. In order to improve the filter performance, trends in the residual sequences must be removed. An iterative procedure was developed to achieve this and is described as follows:

1. Compute  $\Delta\tau_{ij} = \frac{E[z_{ij} - h(x_{ij}^n)]}{c_{ij}}$  where  $i = 9, 10, 11$  and  $j = 9, 10, 11$ .
2. Update  $\tau_{ij} = \tau_{ij} - \Delta\tau_{ij}$ .
3. Rerun the least-squares filter.
4. If all  $|E[z_{ij} - h(x_{ij}^n)]| < 1$  meter then stop; otherwise go to step 1.



The procedure was applied to the July 1989 data set. After 10 iterations, all 6 expected residuals converged to within 1 meter, and the least-squares filter produced the position estimate with an average rms of 2.3 meters. The residual is lower than 2.7 meters and indicates that the position estimate for records 1003 to 2120 is closer to the true float positions. The constant value estimates used in the 10th run listed in Table 3.10 will replace the mode values as the new travel time estimates and will be used by the Kalman filter.

**Table 3.10** Bottomed float surface echo and direct path between bottomed floats travel time estimate, July 1989 experiment.

Float-Path	Travel Time Estimate (msec)
9-10	4028 (was 4025)
9-11	4152 (was 4157)
10-11	4130 (was 4132)
9-9	5401 (was 5402)
10-10	5409 (was 5422)
11-11	5405 (was 5404)

### 3.4.2 Kalman Filter

The measurements, sound speed and variance estimates, and the initial estimates were applied to the Kalman filter. Using process noise values ranging from  $10^{-12}$  to  $5 \times 10^{-8}$  (meters/second)<sup>2</sup>, the Kalman filter was run 24 times. Table 3.11 lists the mean innovation power resulting from each run.

It has been shown using simulations [Culver and Hodgkiss, 1989] that the process noise that minimizes the power in the innovations sequence produces a position estimate with the smallest true rms error. The minimum is seen to occur at  $10^{-9}$ , which is the same found for the 1987 experiment [Culver and Hodgkiss, 1989]. Thus, process noise for the July 1989 experiment is estimated to be  $10^{-9}$  (m/s<sup>2</sup>)<sup>2</sup>.

Table 3.11 Mean innovation power produced by the Kalman filter, July 1989 experiment.

Process Noise ((meters/ second <sup>2</sup> ) <sup>2</sup> )	Mean Innovation Magnitude (meters)
$1 \times 10^{-12}$	7.0671
$2 \times 10^{-12}$	6.0969
$3 \times 10^{-12}$	5.6302
$5 \times 10^{-12}$	5.1290
$7 \times 10^{-12}$	4.8450
$1 \times 10^{-11}$	4.5793
$2 \times 10^{-11}$	4.1538
$3 \times 10^{-11}$	3.9536
$5 \times 10^{-11}$	3.7460
$7 \times 10^{-11}$	3.6335
$1 \times 10^{-10}$	3.5331
$2 \times 10^{-10}$	3.3866
$3 \times 10^{-10}$	3.3269
$5 \times 10^{-10}$	3.2753
$7 \times 10^{-10}$	3.2546
$1 \times 10^{-9}$	3.2435
$2 \times 10^{-9}$	3.2539
$3 \times 10^{-9}$	3.2808
$5 \times 10^{-9}$	3.3401
$7 \times 10^{-9}$	3.3974
$1 \times 10^{-8}$	3.4770
$2 \times 10^{-8}$	3.6933
$3 \times 10^{-8}$	3.9648
$5 \times 10^{-8}$	6.8216

### 3.5 Localization Results

In this section, the outputs from the localization filters are discussed. Of interest are RMS position error estimate, RMS residual/innovation, float position estimate, distance difference between filters, float depth variation, and float speed estimate.

The curves shown in Figure 3.15 are the mean innovation power, or the Kalman filter's estimate of the rms position error, and the least-squares filter's estimate of the rms position error. The vertical axis is rms error or mean innovation magnitude in meters. The horizontal axis is the estimate of process noise given to the Kalman filter as a parameter. Simulations [Culver, 1988] have shown that the true rms error in the Kalman filter's position estimate was always bracketed by the mean magnitude of the innovation and the filter's estimate of the rms error. Therefore, the rms error in the Kalman filter estimate is thought to be less than 3.3 meters. The least-squares filter's estimate of rms float position error is 2.3 meters. Simulation results have indicated that the true rms error in the least-squares filter's position estimate is no more than about twice the estimated error. Accordingly, the rms error in the least-squares filter estimate is thought to be less than 4.6 meters.

The rms residual for the least-squares estimates and the rms innovation for the Kalman filter estimates are shown as a function of measurement (Swallow float record) number in Figure 3.16. Both rms residual and innovation contain large spikes around records 1600 and 1700. These spikes are due to missing surface echo travel time measurements in floats 6 and 8's data, and the values determined by the adaptive linear predictor must still contain large errors.

Figure 3.17 shows the least-squares filter's float horizontal position estimates between records 1003 and 2120. The position estimates indicate that the freely drifting floats dispersed away from the center of the float triangle with floats 0 and 1 moving to the north west, floats 2 and 3 to the west, float 4 to the southwest, and floats 5, 6, 7, and 8 to the southeast. The drifting pattern was probably due to the complex water movement (including eddies, wind-driven surface currents, and the California Current) near the experiment site. The least-squares filter's float depth estimates are also plotted in Figure 3.18.

The distance between the two filters' position estimates is relatively small for all floats with an rms difference less than 3 meters for most of the experiment. Figures 3.19 show the enlarged version of the Kalman filter's float depth estimates as a function of record number. The floats oscillate irregularly and slowly, with periods of 30 to 90 minutes, which correspond roughly to internal wave periods. The slowly increasing depth trend, except for float 0, is probably caused by gradual compression of the float as it gets colder.

The float speed estimates derived from the Kalman filter's X, Y, and Z velocity component estimates are plotted in Figure 3.20. The float speeds appear to be rather unsteady (i.e., high process noise) throughout the experiment. The large-scale speed oscillation with periods of 4 to 12 hours,

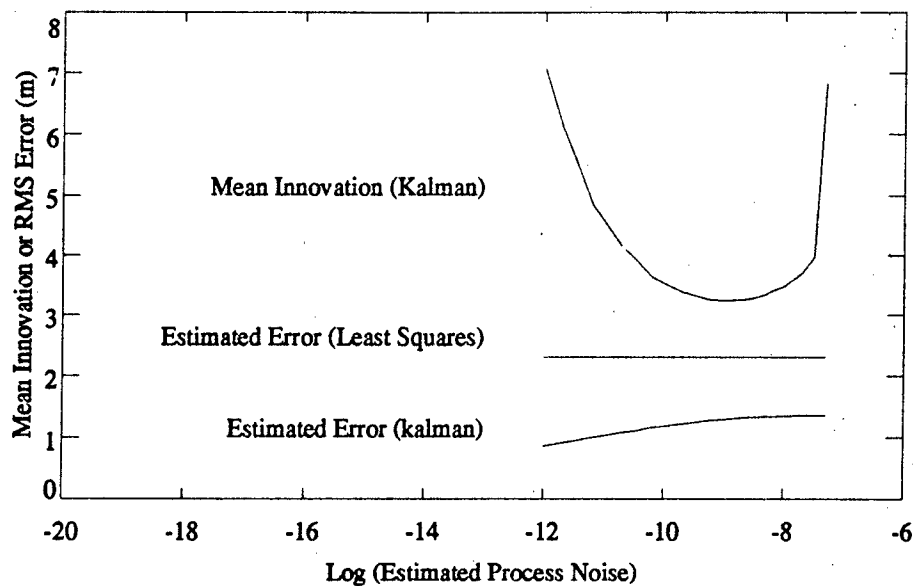


Figure 3.15 Mean innovation and RMS error of the Kalman and least-squares filters, July 1989 experiment.

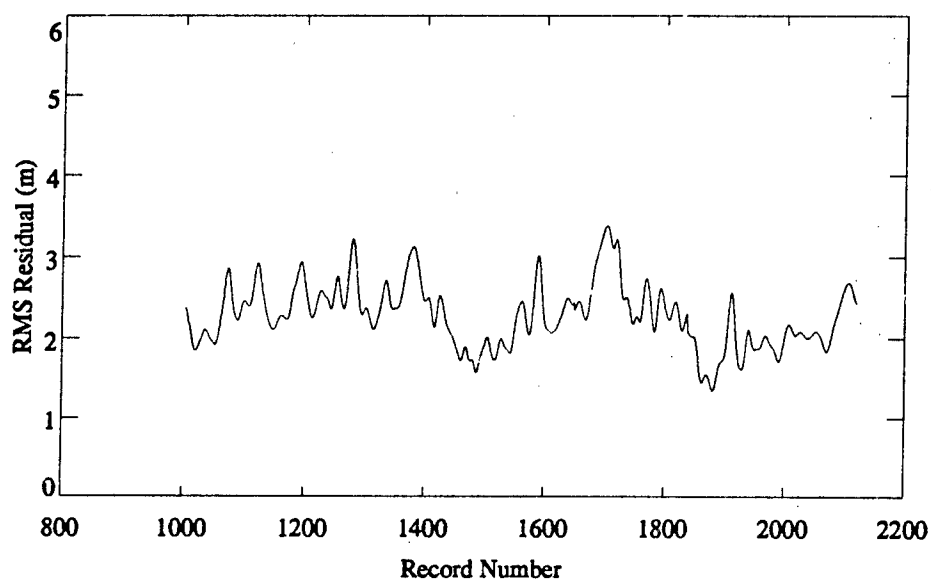
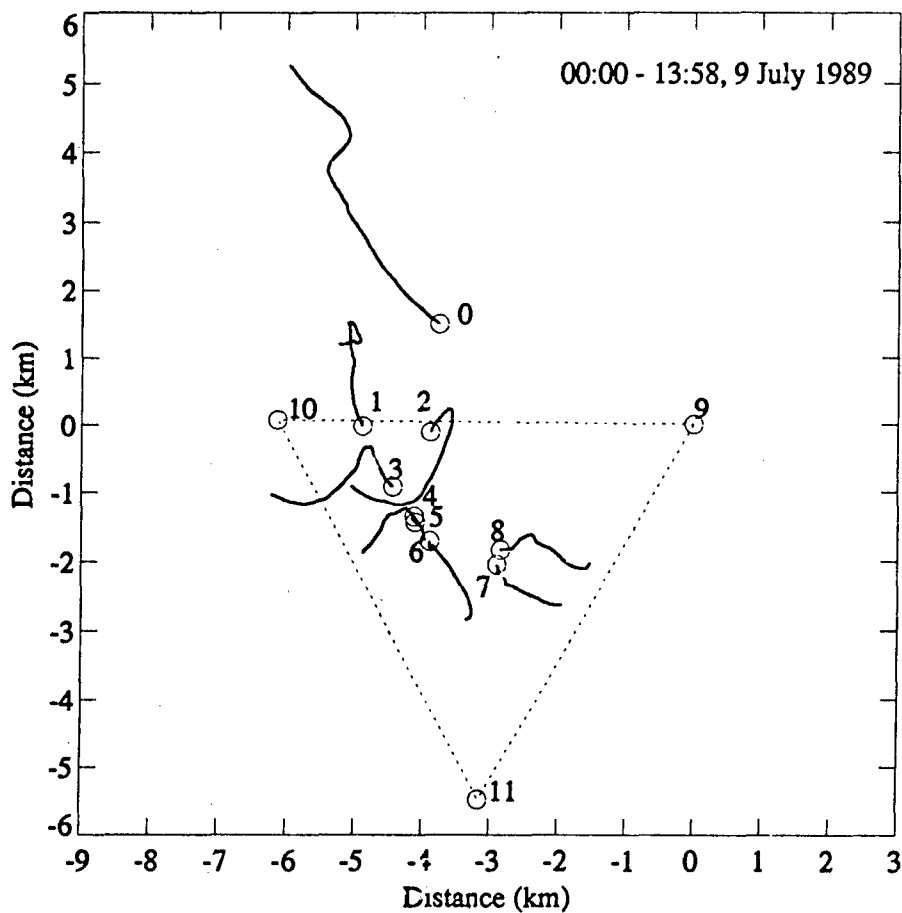
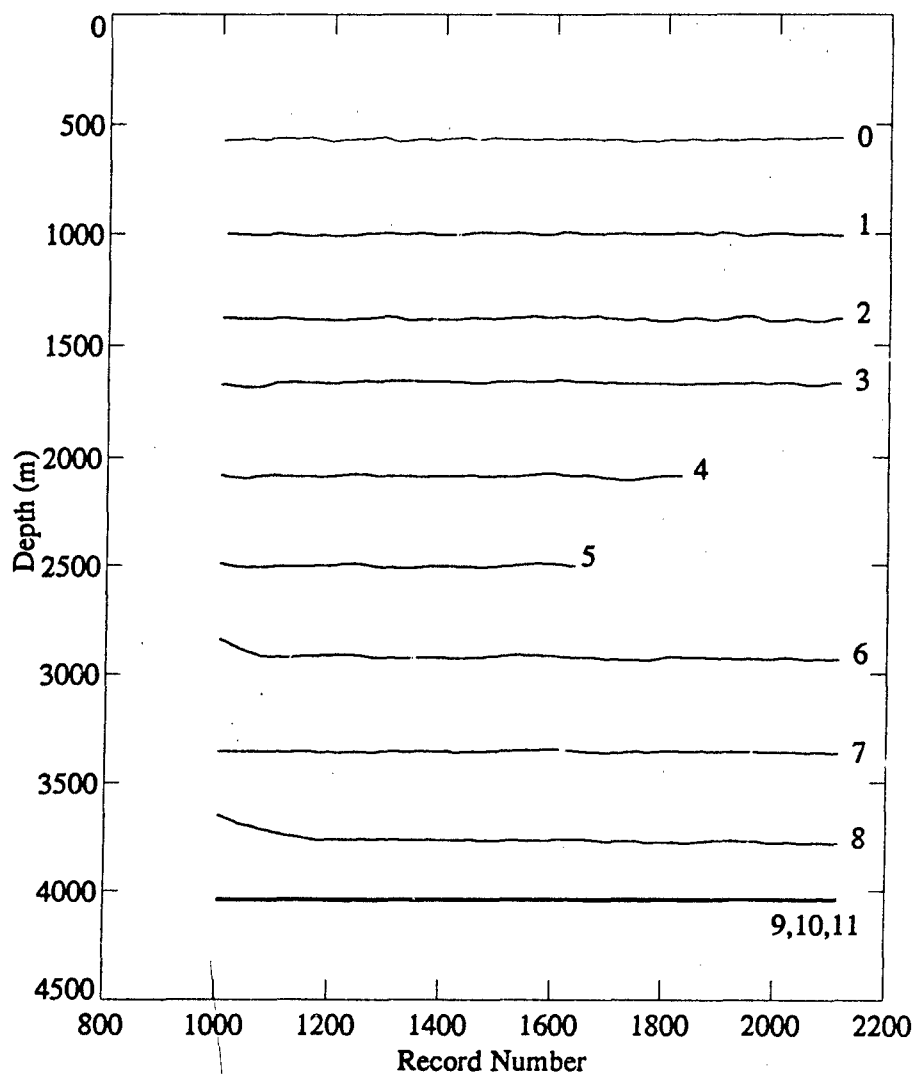


Figure 3.16 RMS residual of least-squares filter position estimates, July 1989 experiment. The horizontal axis of the figure gives the time in units of Swallow float record number. Eighty records represent 1 hour.



**Figure 3.17** Float horizontal displacement estimates using least-squares filter during the July 1989 experiment. The circles mark the starting positions.



**Figure 3.18** Float depth estimates using least-squares filter, July 1989 experiment. The horizontal axis of the figure gives the time in units of Swallow float record number. Eighty records represent 1 hour.

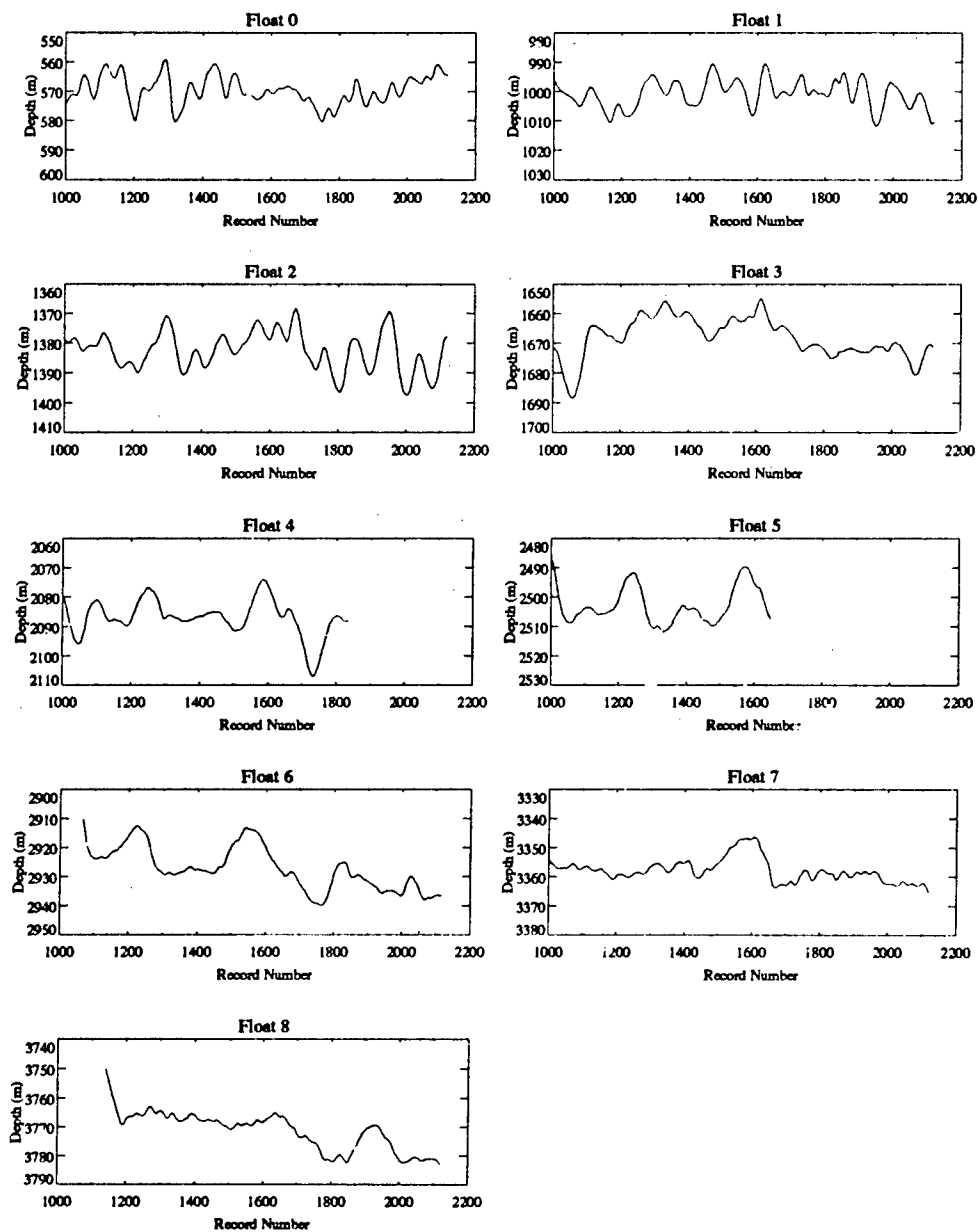


**Figure 3.19** Float depth estimates using Kalman filter, July 1989 experiment. The horizontal axes of the figure give the time in units of Swallow float record number. Eighty records represent 1 hour.

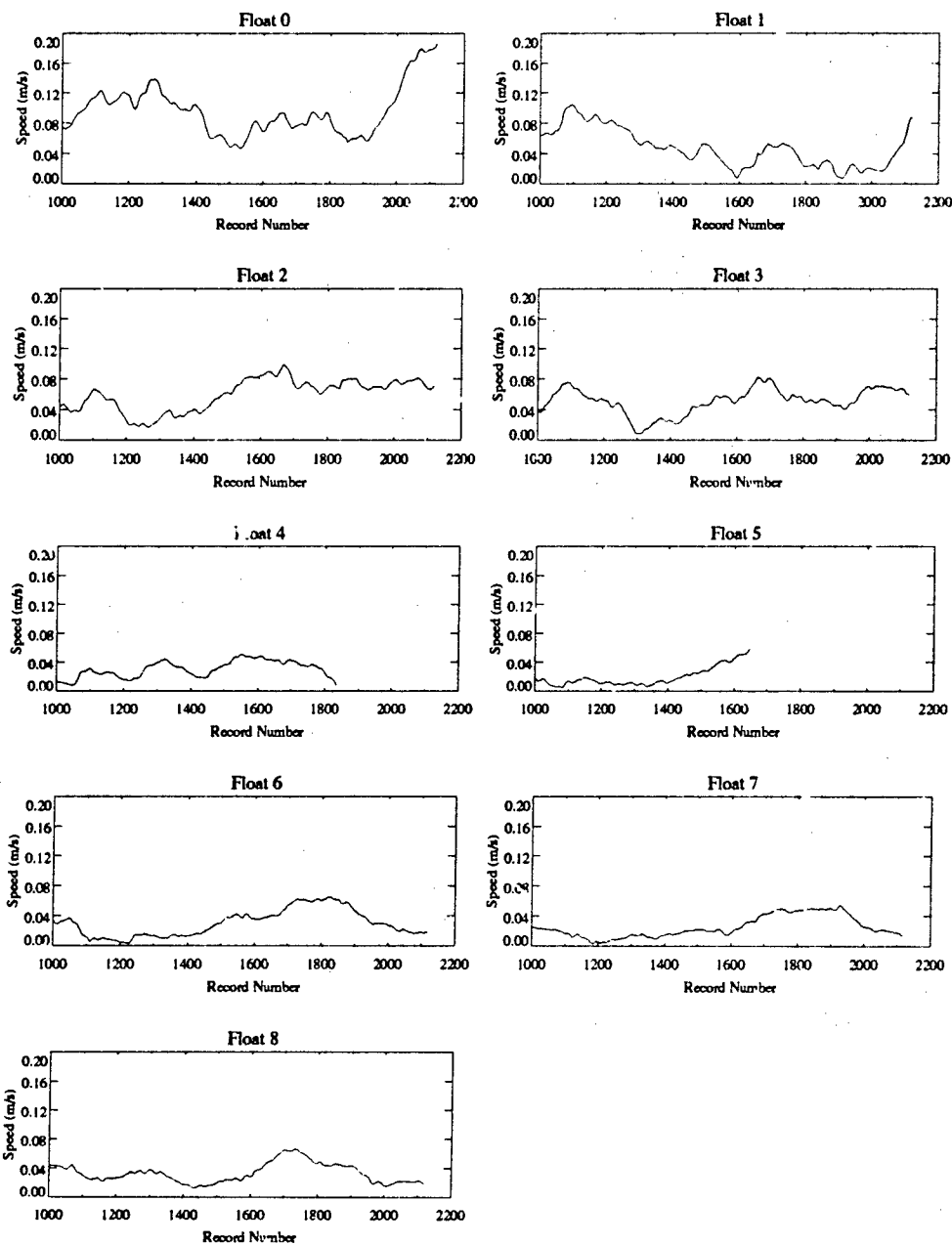


Figure 3.20 Float speed estimates derived from the Kalman filter's X, Y, and Z velocity estimates, July 1989 experiment. The horizontal axes of the figure give the time in units of Swallow float record number. Eighty records represent 1 hour.



depending on float equilibrium depth, is thought to be caused by the tidal currents. Average float speeds for the freely drifting floats are listed in Table 3.12.

### 3.6 Summary

In this chapter, two localization methods, generalized least-squares filter and Kalman filter, were reviewed from the performance-criteria point of view. The inputs to both filters using data from the July 1989 experiment were described in detail. The procedures for tuning the filters were described, and the results from both filters were discussed and compared. The rms position error was estimated to be less than 3.3 m for the Kalman filter and less than 4.6 m for the least-squares filter. Due to the high process noise experienced by the floats during the experiment and the quasi-vertical-line-array deployment geometry [Culver and Hodgkiss, 1988], the two filters performed comparably. The two position estimates had an rms difference of less than 3 m for most of the experiment. Both methods appeared to be capable of estimating float positions to within the desired accuracy of one-tenth of a wavelength at the highest frequency of interest 20 Hz (7.5 m) in order to effectively beamform the VLF acoustic data.

**Table 3.12** Average float speed, July 1989 experiment.

Float Number	Average Speed (meters/hour)
0	350
1	170
2	220
3	180
4	80
5	40
6	110
7	90
8	120

## 4. SOURCE LOCALIZATION WITH SWALLOW FLOAT ARRAY

### 4.1 Introduction

This chapter presents the results from matched-field processing of a 14-Hz-tone propagation collected during the July 1989 Swallow float experiment in the North-East Pacific. There are three steps involved in the matched-field processing as depicted in Figure 4.1. The first step is the estimation of array covariance matrix at the source frequency; the second is the prediction of replica vectors for all assumed source locations; and the last step is the computation of ambiguity surfaces: a peak in the ambiguity surfaces indicates a likely source location. The fundamental and theoretical backgrounds of MFP technique were given in chapter 1.

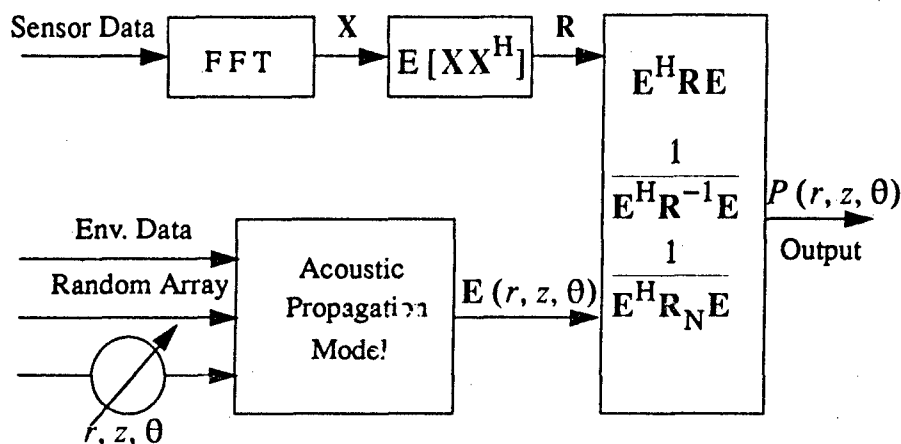


Figure 4.1 Matched-field processing block diagram.

This chapter is organized as follows. Section 2 describes the preparation of VLF acoustic data collected during the 1989 experiment and the estimation of the array covariance matrix for the selected time interval. Section 3 describes the acoustic environment of the oceanic channel between the MARK VI towed source and the Swallow float array and presents the modeling the replica pressure field. Section 4 presents the MFP results on experimental data using Bartlett, Minimum Variance, and MUSIC processors, while section 5 gives the controlled MFP simulation to aid in interpreting the MFP results from experimental data. Lastly, section 6 provides a summary of the chapter.

## 4.2 VLF Acoustic Data Preparation

Although each Swallow float collects three channels of geophone data and one channel of hydrophone data, only the omnidirectional hydrophone data are studied and analyzed in this study. The goal of preparing the acoustic data is to process the acoustic time series to a form from which the cross-spectral density matrix or array covariance matrix can be estimated. This section discusses the essential steps needed to estimate the array covariance matrix.

### 4.2.1 Aligning Float Time Bases

Since each float contains its own clock for timing, the first step in processing the acoustic data is to align the time bases. If we denote time according to float  $j$ 's clock as  $T_j$  and true elapsed time as  $t$ . Then,

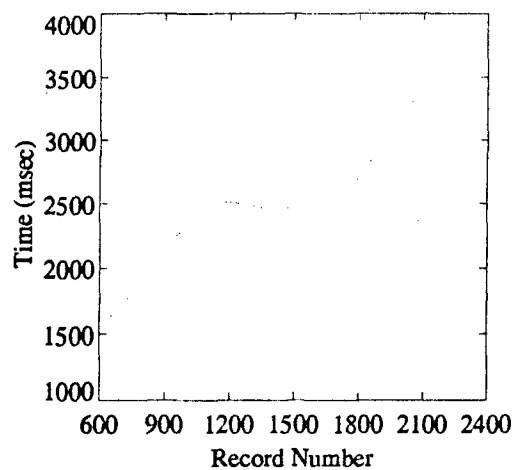
$$T_j(t) = h_j t^2 + g_j t + a_j \quad (4.1)$$

where  $h_j$  is the float clock acceleration,  $g_j$  is the float clock rate, and  $a_j$  is the float clock offset, all of which are constants unique to each float. Note that  $g_j$  is dimensionless, and the units of  $h_j$  and  $a_j$  are  $\text{time}^{-1}$  and time, respectively. Ideally,  $h_i$  and  $a_i$  are equal to 0, and  $g_i$  is unity. The direct approach to the time base problem is to solve equation (4.1) for true time  $t$  in terms of  $T_j$ ,  $h_j$ ,  $g_j$ , and  $a_j$  provided  $h_j$ ,  $g_j$ , and  $a_j$  are known. The float time base can then be aligned to true time. The  $h_j$ ,  $g_j$ , and  $a_j$  can be determined by (1) using a satellite synchronized clock on board ship to frequently communicate with the floats in real time to get  $T_j$ 's and (2) fitting the  $T_j$ 's with a second-order curve, the coefficients of the fitted curve give the  $h_j$ ,  $g_j$ , and  $a_j$ .

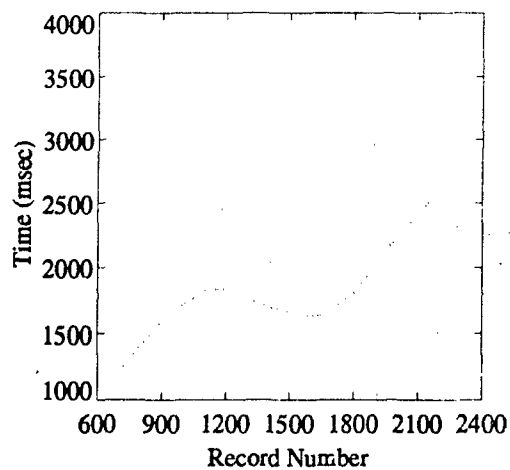
An alternative approach to the time-base alignment problem is to estimate the relative clock acceleration, clock rate, and the offset,  $(h_i - h_j)$ ,  $(g_i - g_j)$ , and  $(a_i - a_j)$ , respectively. Once these quantities are known, we may choose one float as a reference whose time base will not be shifted and shift the time base of the rest of the floats' time series to align them with the reference float's time base. It has been shown [Culver et. al., 1989] that the reciprocal path travel times can be combined to estimate the relative clock acceleration, clock rate, and the offset differences,  $(h_i - h_j)$ ,  $(g_i - g_j)$ , and  $(a_i - a_j)$ . That is,

$$\Delta T_{ij}^n \approx (45 \times n)^2 (h_i - h_j) + (45 \times n) (g_i - g_j) + (a_i - a_j) \quad (4.2)$$

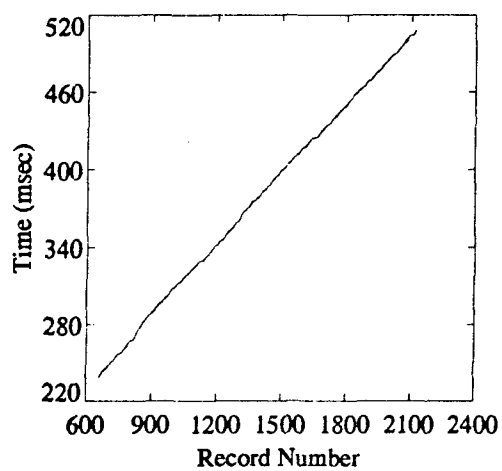
where  $n$  is the record number (each record lasts 45 seconds), and  $\Delta T_{ij}^n$  is approximately equal to one-half the difference between the two reciprocal measurements  $(\tau_{ji}(n) - \tau_{ij}(n)) / 2$ . As in the first approach, the curvature, slope, and intercept of the second-order curve fitted to the travel time differences provide estimates of the differences between the float clock accelerations, rates, and offsets. In this study, we have adopted the latter approach to align the float time bases. Figure 4.2



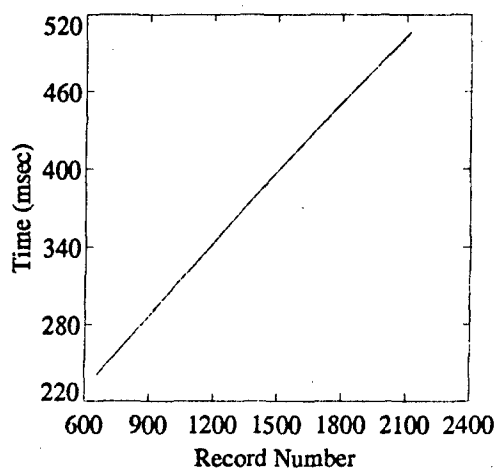
(a)



(b)



(c)



(d)

**Figure 4.2** (a) Float 2 listening to float 8, (b) Float 8 listening to float 2, (c) Travel time difference between floats 2 and 8, and (d) Second-order fit of (c).

illustrates the relative clock acceleration, clock rate, and offset estimates between floats 2 and 8. Appendix C summarizes the coefficients of the second-order curves fitted to the travel time differences for all float pairs.

#### 4.2.2 Selecting Data Records

To ensure the quality of the array covariance matrix estimate, the data records need to be qualified and selected with care. Two criteria used in selecting the data record are described.

##### 4.2.2.1 Signal-to-Noise Ratio

The first criterion in selecting data records is to observe pressure power spectral estimates of the time series for signal-to-noise ratio at the frequency of interest. The power spectra, computed between 0 and 25 Hz and plotted in Figure 4.3 are obtained by processing 3 minutes of data (records 1143 to 1146). The power spectra are derived from incoherently averaging 28, 50 percent overlapped, 512-point FFTs (97-mHz bin width). A Kaiser-Bessel window with  $\alpha$  parameter of 2.5, yielding a sidelobe level of -57 dB [Harris; 1978], weights the data prior to each FFT. Power values are calibrated in dB re 1  $\mu$ Pa. The 90 percent confidence level in these spectra is about  $\pm 1$  dB. The 14 Hz was being transmitted during the time when data records 1120 through 1160 were collected. A line at 14 Hz, about 10 to 15 dB above the background noise, can be clearly seen in all freely drifting floats' pressure spectra. The high S/N at 14 Hz observed in the power spectra illustrates the good quality of the 1989 Swallow float data sets.

##### 4.2.2.2 Spatial Coherence

The second criterion in selecting the data is to estimate the spatial coherence between floats. Coherence is a measure of the causality and similarity between a pair of signals received by two different sensors. Given two stationary zero-mean random processes  $x(t)$  and  $y(t)$ , the coherence, or more precisely, the magnitude-squared coherence (MSC) is defined as

$$|\gamma_{xy}(f)|^2 = \frac{|S_{xy}(f)|^2}{S_{xx}(f)S_{yy}(f)} \quad (4.3)$$

where  $S_{xy}(f)$  is the cross-spectral density at frequency  $f$  between  $x(t)$  and  $y(t)$  with power spectra  $S_{xx}(f)$  and  $S_{yy}(f)$ . The MSC function evaluated at  $f$  is a real value, conveniently normalized to lie between zero and unity. High coherence of a line frequency harmonic among all float pairs not only indicates the signals originate from the same source but assures high array gain when the individual sensor outputs are combined to form a beamformer. Figure 4.4 shows the magnitude-squared coherence and the phase difference between floats 0 and 2 during records 1040-1240, while appendix D lists the MSC value between all elements of the freely drifting array during

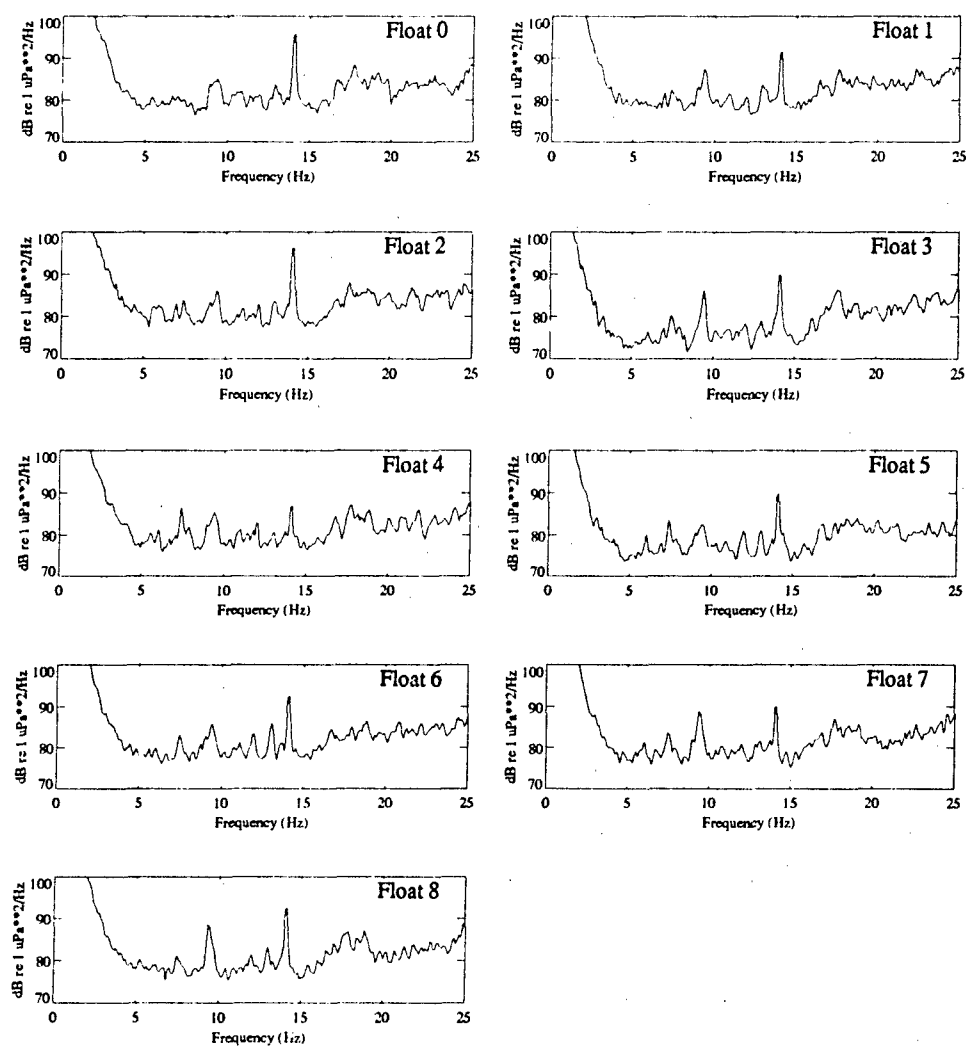


**Figure 4.3** Acoustic pressure power spectra for midwater floats.

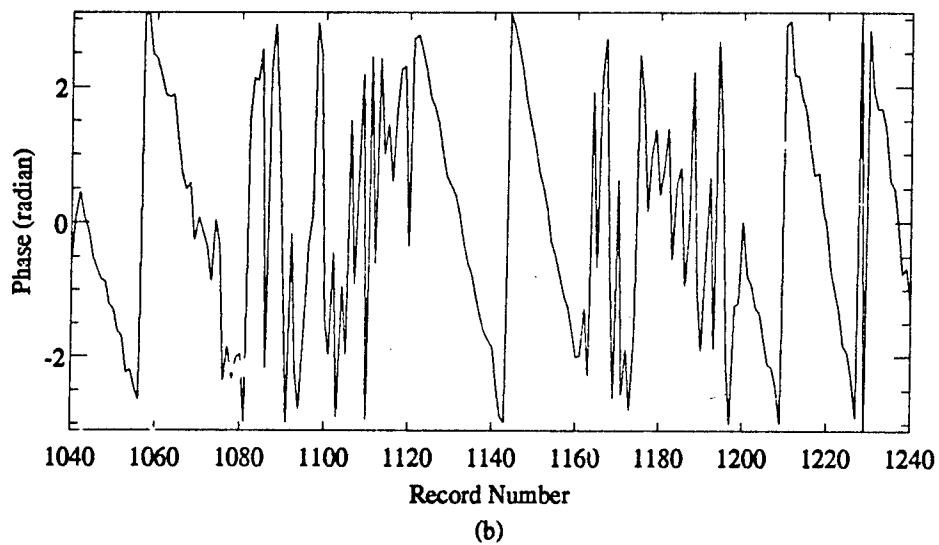
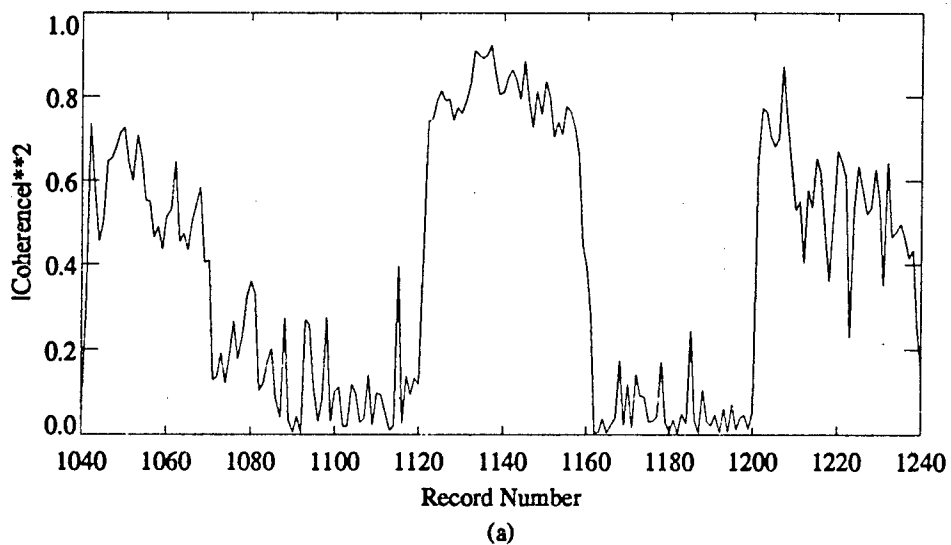


**Figure 4.4** (a) Spatial coherence at 14 Hz and (b) Phase difference between floats 0 and 2 at 14 Hz during records 1040 - 1240.

record 1145. The MSC functions are calculated by averaging over 40.96 seconds of data, 128-point FFT's with 50 percent overlap, providing 31 averages. The high coherence during records 1120 to 1160 is a confirmation that the signal originates from the same source, and the exhibition of the smooth measure of the phase differential qualifies the 1989 Swallow float data set for beam-forming application.

#### 4.2.3 Estimating the Array Covariance Matrix

The problem of estimating the array covariance matrix is required by all three processors as discussed in chapter 2. The array covariance matrix  $\mathbf{R}$  can be estimated from the measurement data and is given by

$$\mathbf{R} = \frac{1}{K} \sum_{i=1}^K \mathbf{X}_i \mathbf{X}_i^H \quad (4.4)$$

where  $\mathbf{X}_i$  is the vector of Fourier coefficients across the array at the frequency of interest  $f$  corresponding to the time snapshot  $i$ . Frequency bins of 0.4-Hz width centered at 14 Hz were extracted from 128-point FFT's (2.56 seconds of data) using a Kaiser-Bessel (with  $\alpha = 2.5$  for first sidelobe levels of -57 dB) window and 50 percent overlap for each of the nine floats over a 40.96-second data record. This results in a  $K = 31$  dyad products ( $\mathbf{X}_i \mathbf{X}_i^H$ ) being averaged for the covariance matrix estimate. In practice, the number of averages required to produce a reliable covariance matrix estimate is about twice to three times the number of sensors in the array. In our case, 31 averages will suffice.

#### 4.2.4 Inverting the Array Covariance Matrix

Since the matrix must be inverted for the MV processor, it should be well conditioned and of full rank. It is well known that as many dyads as sensors must be averaged to ensure full rank. Although a large number of snapshots (i.e., 31) used in (4.4) to compute the array covariance matrix  $\mathbf{R}$  ensures the invertibility of the covariance matrix in theory, the condition number of the matrix given by the ratio of the smallest to the largest eigenvalue is below  $10^{-6}$ , and additional effort is required [Tran, 1990].

The two most commonly used techniques in handling the ill-conditioned covariance matrix are the eigenstructure decomposition method and the white-noise stabilization method. The eigenstructure method uses the spectral theorem to express the array covariance matrix  $\mathbf{R}$  and its inverse as summations of outer products of the eigenvectors (assuming  $\mathbf{R}$  is positive definite and Hermitian).



$$\mathbf{R} = \sum_{i=1}^N \lambda_i \mathbf{V}_i \mathbf{V}_i^H \quad (4.5)$$

$$\mathbf{R}^{-1} = \sum_{i=1}^N \frac{1}{\lambda_i} \mathbf{V}_i \mathbf{V}_i^H \quad (4.6)$$

If  $\mathbf{R}$  is not full rank, i.e., the  $N$  sensor array covariance matrix  $\mathbf{R}$  with  $K < N$  nonzero eigenvalues, then we can express the inverse in (4.6) as

$$\mathbf{R}^+ = \sum_{i=1}^K \frac{1}{\lambda_i} \mathbf{V}_i \mathbf{V}_i^H \quad (4.7)$$

$\mathbf{R}^+$  is also called the pseudo-inverse [Penrose, 1955]

Another approach to this problem is white-noise stabilization, which is a procedure of stabilizing the covariance matrix with spatial white noise to allow for matrix inversion. This method is also called "diagonal loading" [Carlson, 1988]. In essence, this method adds to the main diagonal of  $\mathbf{R}$  the quantity

$$\gamma \frac{\text{tr}(\mathbf{R})}{M}$$

where  $\gamma$  is a fraction of noise with typical values between  $10^{-3}$  and  $10^{-1}$ , and  $\text{tr}$  is the trace operator. Since the white-noise stabilization method requires less computation, it is used in this thesis. The covariance matrix  $\mathbf{R}$  is stabilized by adding to the main diagonal the quantity  $10^{-1} (\text{tr} \mathbf{R} / M)$ . Using a stabilization factor  $\gamma$  of 0.1 corresponds to introducing in the system an uncorrelated sensor noise 10 dB below the average sensor power level [Tran and Hodgkiss, 1991].

### 4.3 Acoustic Propagation Modeling

The second step toward matched-field processing is the calculation of the replica vectors. To predict the acoustic pressure field received by a sensor due to an assumed source, one must model the acoustic environment between the source and the sensor. This section describes the environmental data collected during the 1989 experiment; presents the modeling of the acoustic environment between the MARK VI source and Swallow float array; and provides the assumptions made in computing the replica vectors.

#### 4.3.1 Environmental Data

As discussed in chapter 2, a large quantity of environmental data was taken during the 1989 experiment, including CTD (conductivity, temperature, and depth) casts, XBTs (ship deployed expendable temperature profilers), and AXBTs (air deployed expendable temperature probes). Plotted in Figure 4.5 is a series of sound speed profiles derived from the CTDs, the XBTs and the AXBTs taken along the approximate path between the source and the Swallow float array within 48 hours of the Swallow float experiment. The sound speed profiles taken near the source and Swallow float deployment site are enlarged and plotted in Figure 4.6. The profiles are typical for middle latitudes in the North Pacific Ocean and are characterized by [Burdic, 1991] (1) a surface layer that extends from the surface to perhaps 100 m, (2) a layer that extends down to perhaps 600 to 800 m and is characterized by a negative gradient, and (3) a deep layer where sound speed increases gradually with depth with positive gradient. All of the profiles along the propagation path exhibit a depth excess that is a necessary condition for long range-propagation [Urlick, 1983].

The meso-scale change in the ocean temperature structure across range on the order of several thousand kilometers results in range-dependent variations in the sound speed profile as shown in Figure 4.5. The slowly varying sound speed structure variation, especially in the upper water column between 120° W and 135° W, is believed to be influenced by the cold waters of the California Current coming down from the north. The sound speed structure between 140° W and 150° W remains relatively stable; this part of the ocean is known to be environmentally benign.

#### 4.3.2 Modeling with Adiabatic Normal Modes

The adiabatic approximation of the normal mode model provides a simple solution to the problem of acoustic propagation in a slowly range-varying ocean (refer to section 1.2.2.1). In this thesis, we use the adiabatic mode theory to model the acoustic pressure field. Recall that the adiabatic mode theory solution in a 2-D environment is:

$$P(r, z) = A \sum_{m=1}^M u_m(z_o; 0) u_m(z; r) \frac{\exp\left(i \int_0^r \xi_m(s) ds\right)}{\sqrt{\xi_m(r) r}} \quad (4.8)$$

The modal sum is over the number of propagating modes,  $M$ , that exist between source and the receiver. The sum involves the depth eigenfunctions at the source  $u_m(z_o; 0)$ , and the receiver  $u_m(z; r)$ , as well as the horizontal wave numbers function  $\xi_m(s)$  reflecting the range dependence of the medium along the path between the source and the receiver. In this study, the implementation strategy for  $\int \xi_m(s) ds$  is to divide the full range into a number of segments; the horizontal wave numbers are calculated at a discrete sets of ranges where sound speed measurements are available.

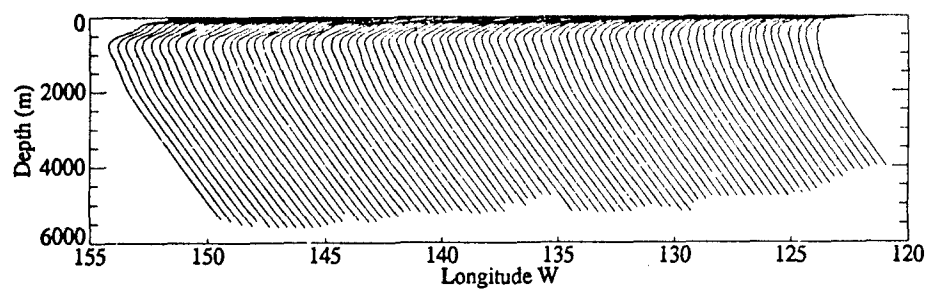


Figure 4.5 Sound speed profiles between 150°W and 122°W.

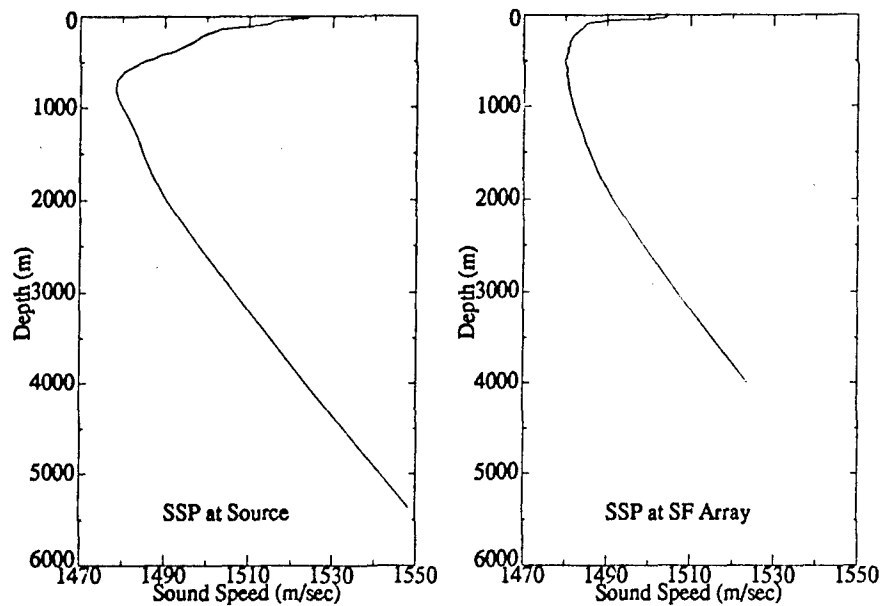


Figure 4.6 Sound speed profiles at the source and Swallow float array.

To determine the number of propagating modes,  $M$ , for the oceanic waveguide formed by the source and the Swallow float array, we need to examine the modal depth eigenfunctions.

#### 4.3.2.1 Depth Eigenfunctions

The mode depth functions  $u_m$  are determined by the source frequency, the nature of the sound speed profile, the water depth, and the boundary conditions at the surface and the bottom. The modal depth eigenfunctions at a frequency of 14 Hz for the environment near the Mark VI source and the Swallow float deployment site are computed with the ATLAS normal mode model [Gordon and Bucker, 1984]. The first 30 modal depth eigenfunctions are gray-leveled and displayed in Figure 4.7. Examining the upper portion of the figure that corresponds to the environment where the source is located, we see that there are about 22 modes trapped in the water column and they are non-bottom interacting; also, for the source depth at 90 m, the first 6 modes are very weakly excited. For the low-order modes to be strongly excited, the source would have to be placed between its turning points where the mode peaks up. The lower portion of the figure corresponds to the environment at the array site; given the water depth at this location, non-bottom interacting modes are limited to the first 16 modes. Now let us examine the pressure field modeled by the adiabatic mode theory, i.e., equation (4.8). Note that the depth functions enter into the pressure field calculation as product  $u_m(z_o;0) u_m(z;r)$  where the one depth function is evaluated at source depth and the other depth function is evaluated at the receiver depth. As result of the product  $u_m(z_o;0) u_m(z;r)$ , and assuming the bottom interacting modes are unable to propagate out to long range due to bottom attenuation, only the first 16 trapped modes will be used in the calculation of the acoustic pressure field.

To get a visualization of the propagation of the trapped modes, we apply the sound speed profiles collected near the source to a ray acoustic model RASP [Palmer and Powell, 1989]. Figure 4.8 shows a ray trace for a source depth of 90 meters. Only those rays that are refracted in the water column are shown. The rays that reflected off the bottom (the bottom bounce rays that are equivalent to the bottom interacting modes) are omitted from the ray trace since they will not be able to propagate out to the Swallow float array about 2500 km away from the source due to multiple bottom encounters. Because of the shallow source and the depth excess in the sound speed profile, the rays are either refracted-refracted (RR) rays that are trapped in a deep sound channel or refracted, surface-reflected (RSR) rays that do not intersect the bottom and periodically return to the sea surface on the far side of the convergence zone (approximately 50 km), and serve to extend the ranges of good transmission. Table 4.1 lists the equivalent source angles for modes trapped in the water column at a frequency of 14 Hz.

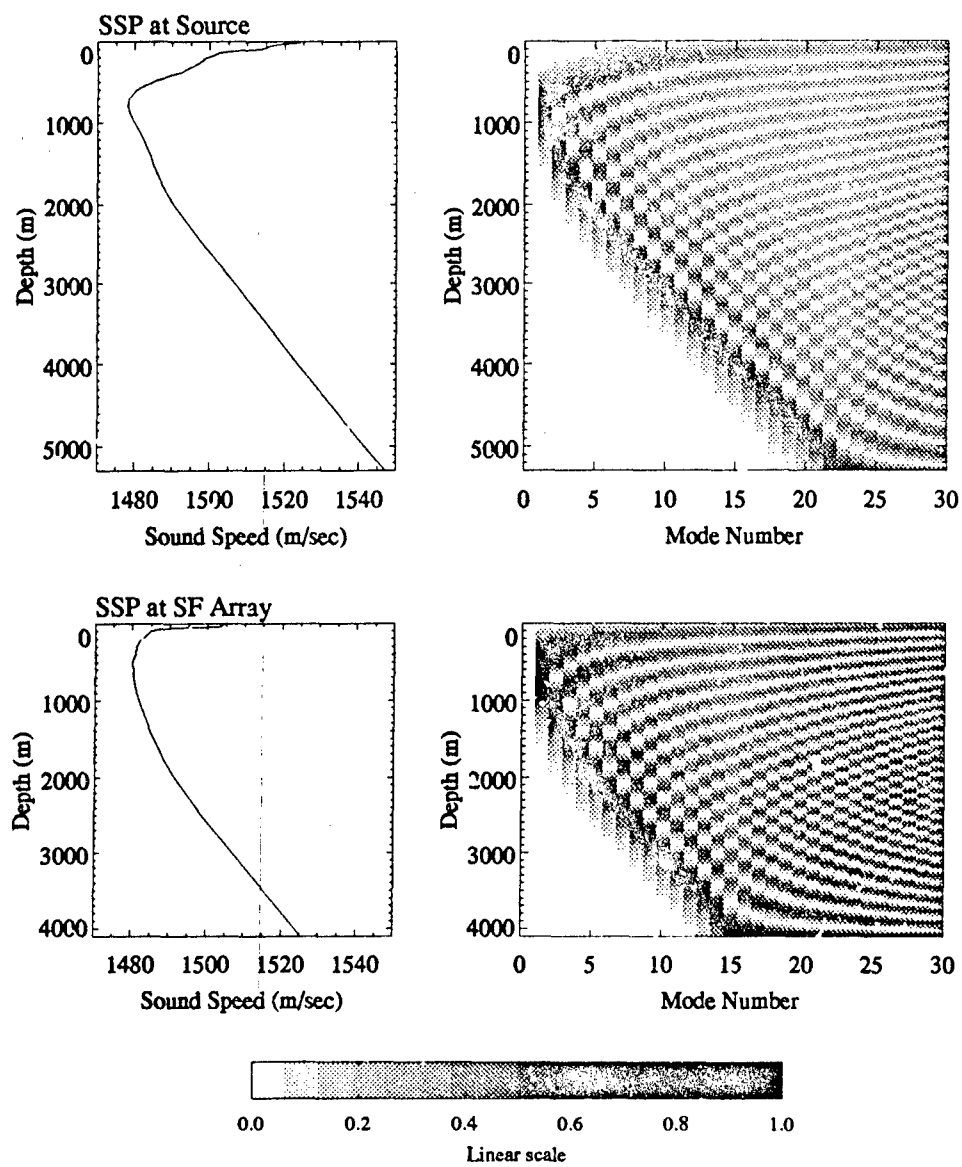


Figure 4.7 Modal eigenfunctions at frequency of 14 Hz.

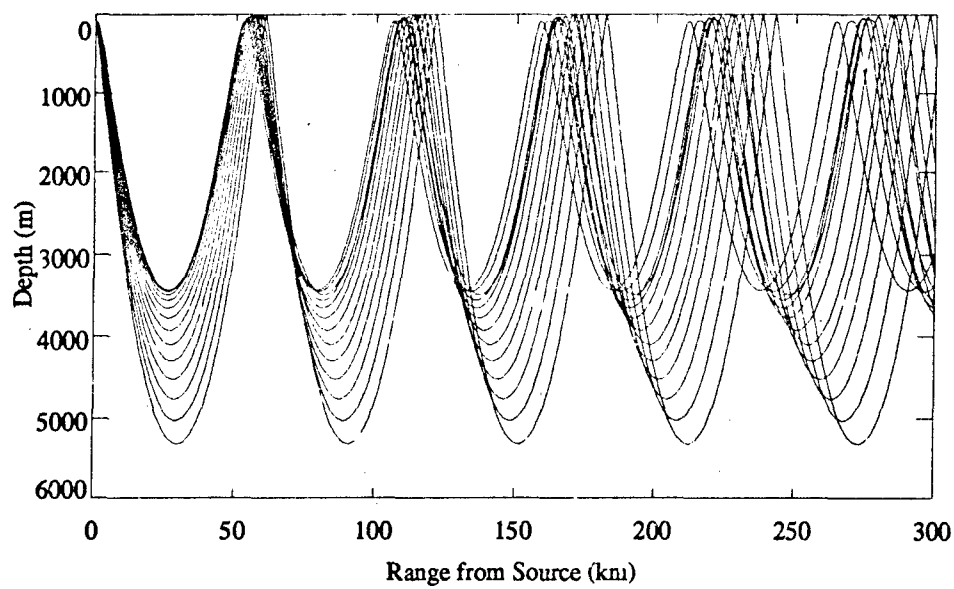


Figure 4.8 Ray traces for source at 90 m.

#### 4.3.2.2 Horizontal Wave Numbers

Like the mode depth eigenfunctions, the eigenvalues or modal horizontal wave numbers  $\xi_m$  are also determined by the frequency, the nature of the sound speed structure (and hence water depth), and the boundary conditions at the surface and bottom. In this study, we use ATLAS to calculate the horizontal wave numbers for the discrete segments (each approximately 30 km) along the path of signal propagation. Table 4.2 gives the eigenvalues for three representative locations along the path between the source and the array for the first 16 modes.

**Table 4.1** Equivalent source angles for modes trapped in the water column at a frequency of 14 Hz.

Mode Number	Source Angle (degree)
1	2.0
2	5.0
3	6.4
4	7.5
5	8.5
6	9.3
7	10.0
8	10.7
9	11.3
10	11.9
11	12.5
12	13.0
13	13.5
14	13.9
15	14.4
16	14.8

**Table 4.2** Eigenvalues for modes trapped in the water column at a frequency of 14 Hz.

Mode Number	Eigenvalues at source (rad/m)	Eigenvalues at 140° W (rad/m)	Eigenvalues at SF (rad/m)
1	0.0593778	0.0593764	0.0593557
2	0.0591910	0.0592177	0.0592227
3	0.0590471	0.0590707	0.0590927
4	0.0589048	0.0589325	0.0589622
5	0.0587666	0.0587980	0.0588299
6	0.0586510	0.0586674	0.0586971
7	0.0585233	0.0585401	0.0585663
8	0.0583968	0.0584139	0.0584366
9	0.0582721	0.0582893	0.0583082
10	0.0581492	0.0581663	0.0581831
11	0.0580283	0.0580445	0.0580601
12	0.0579092	0.0579245	0.0579396
13	0.0577918	0.0578062	0.0578219
14	0.0576766	0.0576898	0.0577127
15	0.0575628	0.0575750	0.0576024
16	0.0574503	0.0574618	0.0574595

#### 4.3.2.3 3-D Field Approximation

As pointed out in chapter 1, range-dependent propagation modeling using the adiabatic normal mode model is a 2-D implementation from which the field at a particular range and depth can be computed, giving the bathymetry and the sound speed measurements along the path between the source and receiver. In this thesis, the 3-D replica pressure field was approximated by evaluating the adiabatic model along a series of  $N$  bearings in the range-dependent environment assuming the environment is azimuth-invariant, to give an  $N \times 2$ -D description of the field. This assumption, which is important for computational efficiency and assumes the sound paths in the range-azimuth plane are taken to be linear, can nonetheless provide a good approximation of the true 3-D field [Perkins and Baer, 1982].



#### 4.4 Experimental Data-Processing Results

After aligning the float time bases and performing data quality checks, the array covariance matrix for record 1145 was estimated, and the replica vectors for the matched-field processors were generated using (4.8). The problem of grating lobes in beamforming using a sparse array was not addressed in this study; we therefore limited our focus to a region of interest. The replica vectors were thus computed for a hypothetical source in a spatial window extending in range from 2300 km to 2700 km, in depth from 0 to 300 m, and in azimuth from  $166^\circ$  to  $176^\circ$  (refer to Figure 3.14; we use the mathematical convention with -X pointing  $0^\circ$  as reference and rotating counterclockwise). The sampling intervals in range, depth, and azimuth were 1000 m, 10 m, and  $0.1^\circ$ , respectively. Matched-field processing was performed with all three processors: Bartlett, MV, and MUSIC. The peak value in the region of interest was recorded and normalized to yield power in dB re  $\mu\text{Pa}$ . Table 4.3 summarizes the results of matched-field processing on the experimental data.

Table 4.3 Matched field processing results.

	Bartlett Processor	MV Processor	MUSIC Processor
Depth of Max.	10 m	130 m	10 m
Range of Max.	2659 km	2659 km	2659 km
Azimuth of Max.	$172.1^\circ$	$172.1^\circ$	$172.1^\circ$
Power of Max.	82.7 dB	73.2 dB	-

Note that power levels were reported for the Bartlett and MV processors only since the MUSIC method did not yield the true power. Figures 4.9, 4.10, and 4.11 present the matched-field ambiguity surfaces. The upper panel in each figure was the range-azimuth ambiguity surface evaluated at the depth where the highest peak occurred while the lower panel was the range-depth ambiguity surface evaluated at the azimuth where the highest peak occurred. In each case, the surface was normalized to its highest peak and was marked with this symbol, \*. For comparison, the true source location was marked with a  $\Delta$ . While mismatch existed, all three processors were in good agreement except for their depth estimates. In fact, all three lacked the depth resolving power. The highest peak in the ambiguity surface differs from the true location by  $0.6^\circ$  in azimuth and 166 km in range. The large number of sidelobes observed in the ambiguity surfaces was thought to be due to imperfect modeling and the sparseness of the array. The MV and MUSIC processors suffered large losses due to mismatch since the replica were imperfect. Ambiguities in range, which have been referred to as sidelobes, were the result of the repetitive structure of the acoustic field in a convergence zone environment.

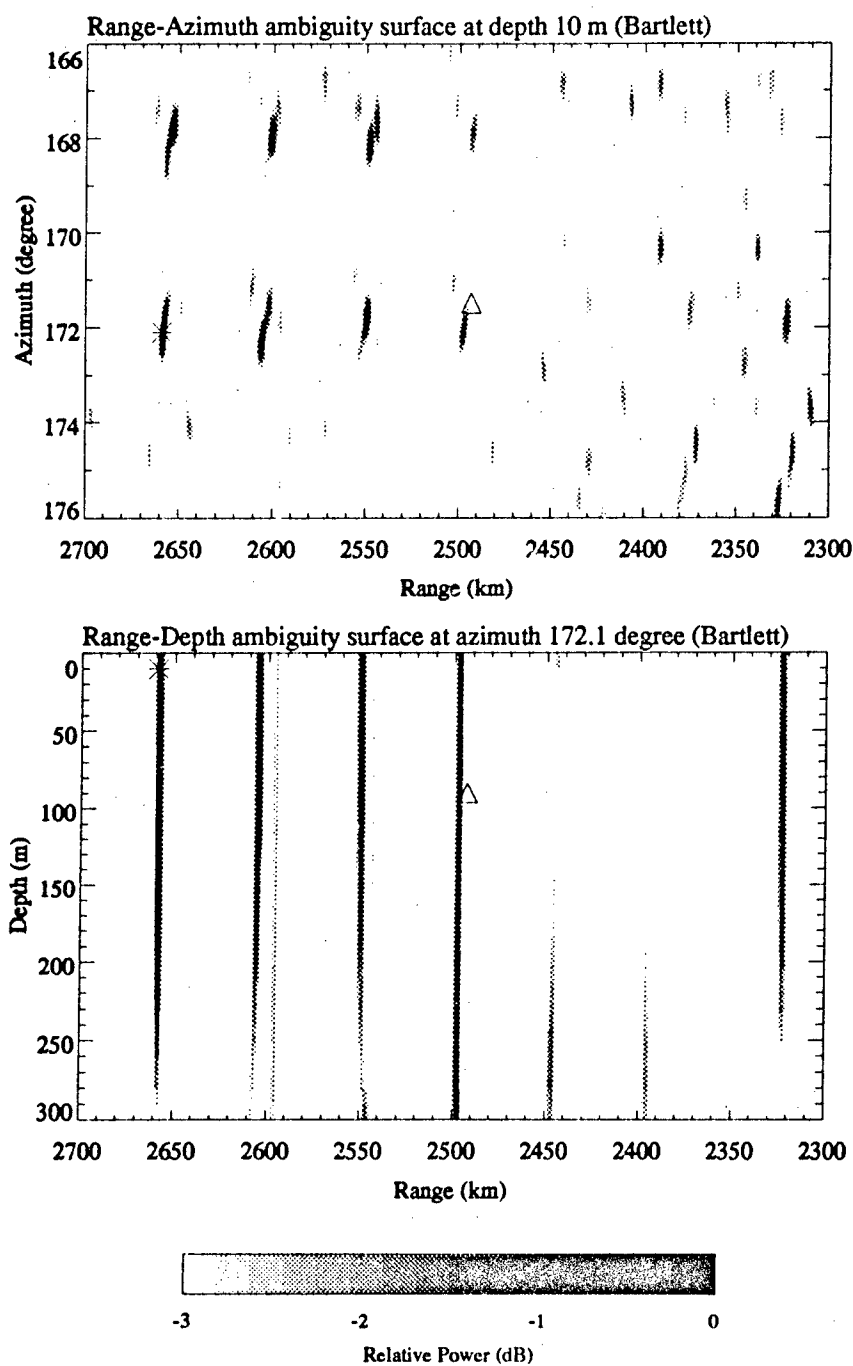


**Figure 4.9** Matched-field processing results using the Bartlett method for the 14-Hz source during record 1145.

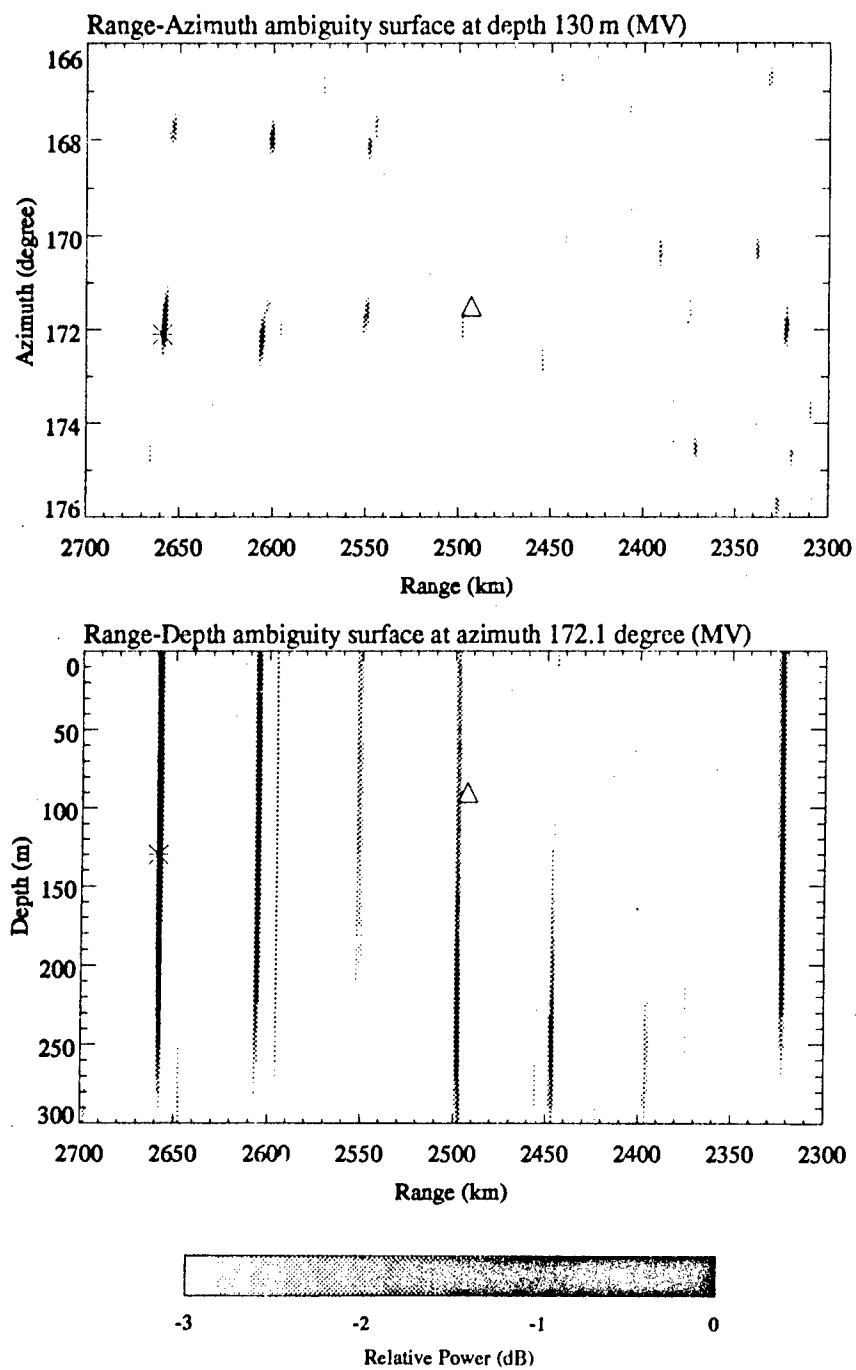


**Figure 4.10** Matched-field processing results using the MV method for the 14-Hz source during record 1145.

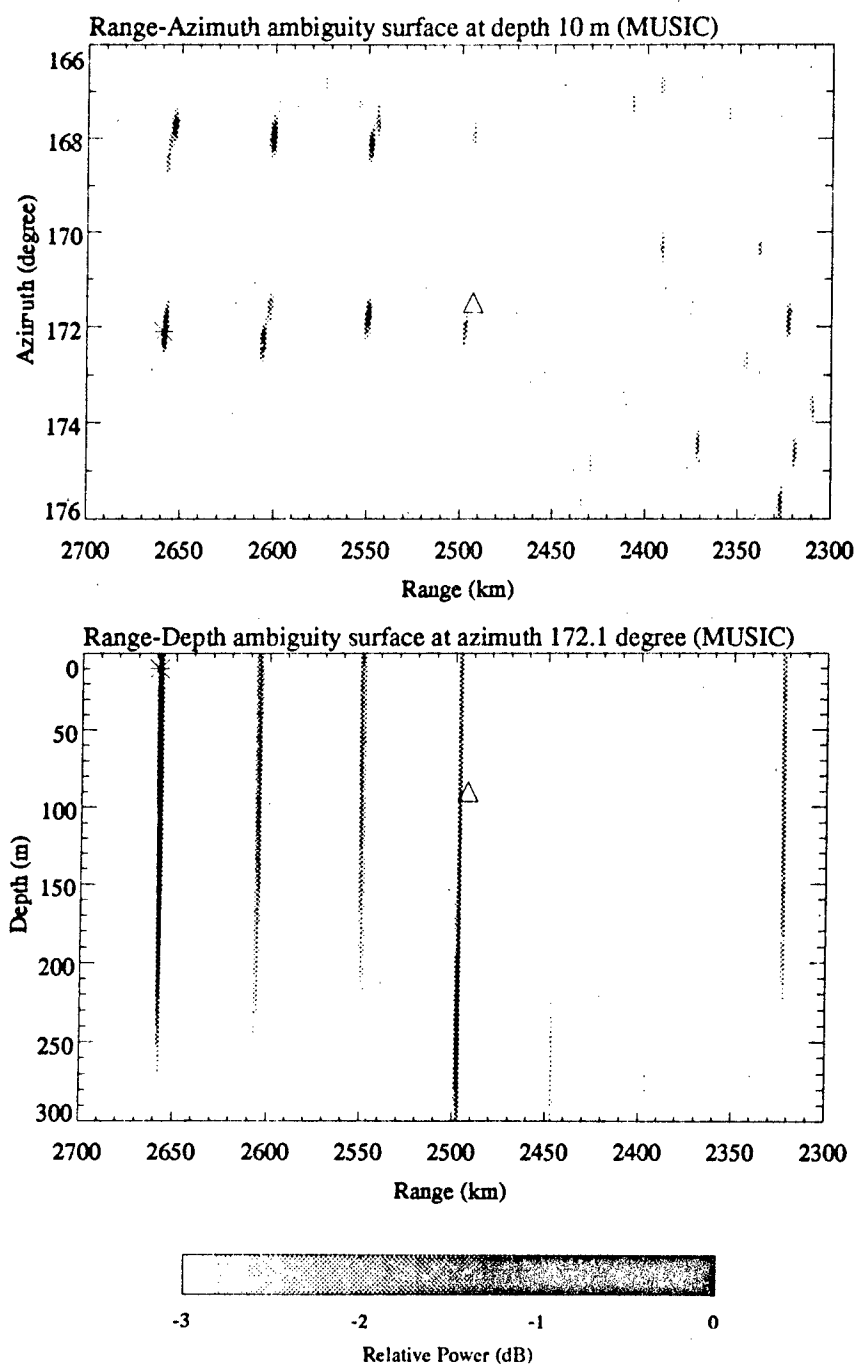


Figure 4.11 Matched-field processing results using the MUSIC method for the 14-Hz source during record 1145.

In addition to the localization performance computed in Table 4.3, the array signal gain was also investigated. Several array performance measures for matched-field processing have been proposed in the literature. In this thesis, we define array signal gain as the ratio of matched-field processor output S/N divided by the average input S/N on the floats. However, the signal level was expected to be nonuniform over the array, so an alternative choice of denominators such as median float input S/N (signal level) and maximum float input S/N (signal level) were also computed. Table 4.4 lists the array gain for various choices of definition using the Bartlett processor for record 1145. Note that the theoretical array gain assuming white noise at the sensor output for a nine sensor array is  $10 \log 9 = 9.54$ .

**Table 4.4** Matched-field processing array gain.

Bartlett Processor	Array Gain (dB)
Max. input S/N	2.6
Ave. input S/N	5.9
Med. input S/N	6.8

## 4.5 Controlled Simulation

While source localization in azimuth was somewhat successful, localization in range and depth seemed to be a problem. Simulations are presented here in an effort to understand the experimental ambiguity surfaces. Three simulation cases were studied: the ideal simulation, uncertainty in float positions, and uncertainty in sound speed structure.

### 4.5.1 No Mismatch Simulations

Assuming there was no mismatch and input S/N was 10 dB, the simulated "acoustic data" and replica vectors were generated using the same environment model. A 14-Hz source was simulated at a range of 2493 km, an azimuth of  $171.5^\circ$ , and a depth of 90 m, which is the true source location at record 1145 according to the R/V Aloha source log. The ambiguity functions for all three processors were evaluated at a depth of 90 m and an azimuth of  $171.5^\circ$  degrees and plotted in Figures 4.12, 4.13, and 4.14, respectively. As expected, the source was correctly localized. Since there was no mismatch, the dynamic range of the ambiguity surfaces was much larger than in the case of the real data. The Bartlett processor produced a large number of sidelobes; the MV processor had better suppression of sidelobes and higher resolution of the main lobe; and the MUSIC processors produced a single peak in the range-depth cell of the simulated source.

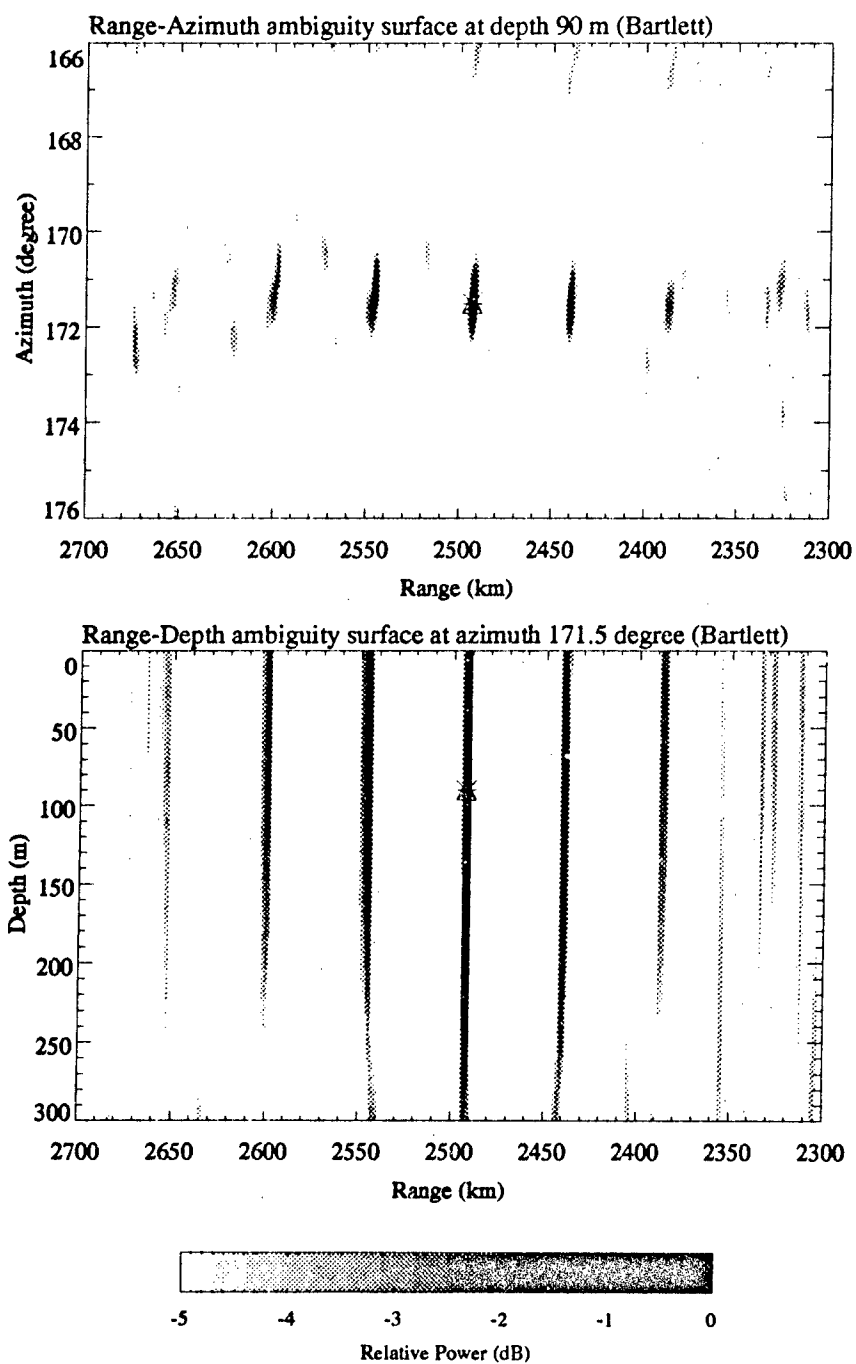


Figure 4.12 Matched-field processing simulation results (no mismatch) using the Bartlett method.

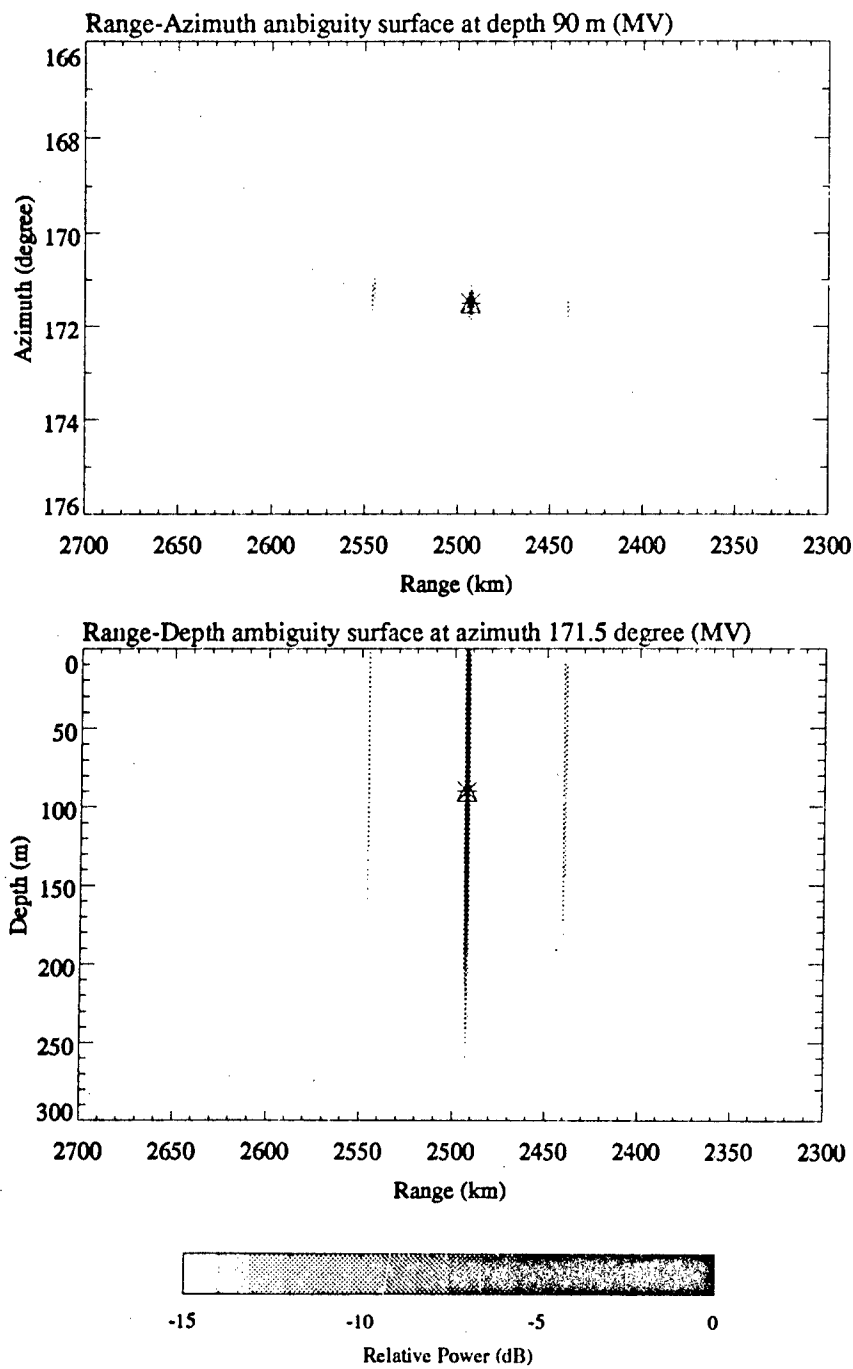


Figure 4.13 Matched-field processing simulation results (no mismatch) using the MV method.

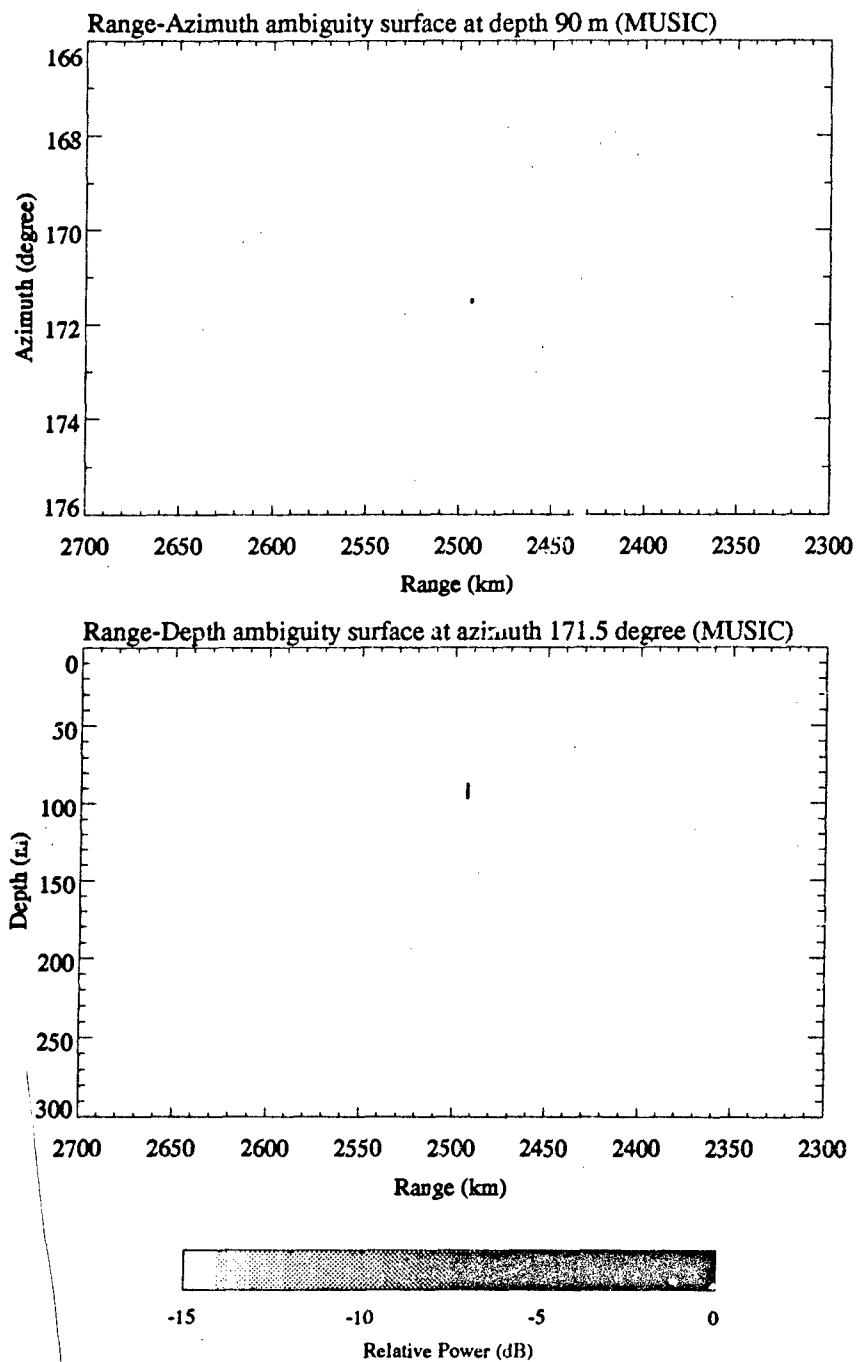


Figure 4.14 Matched-field processing simulation results (no mismatch) using the MUSIC method.



The high sidelobes found predominately for the ambiguity surfaces produced by the Bartlett processor were believed to be due to the nature of the processor and the array geometry. Also, the pressure field calculated using the adiabatic normal mode model was composed of only the first 16 low-order, water-borne modes. Thus, the acoustic pressure field was less complex or less unique at the simulated source location.

The poor depth resolution observed in the Bartlett and MV ambiguity surfaces was thought to be due to the combination of few propagating modes and the low source depth (90 m) to wavelength (105 m) ratio. Not too surprisingly, the MUSIC processor yields excellent depth resolution due to exploitation of the orthogonality principle.

#### 4.5.2 Uncertainty in Float Positions

The sensitivity to sensor position mismatch was then investigated. Assuming there were no position errors, the replica field were generated using the same conditions as in the real data case. However, the simulated "acoustic data" was computed using the array geometry that incorporates random perturbations of 7 meters to each sensor position. The impact of mismatch due to float position error was investigated again in a 10-dB input S/N case. The ambiguity surface is plotted in Figures 4.15, 4.16 and 4.17 and the matched-field processing results are summarized in Table 4.5.

**Table 4.5** Matched-field simulation of sensor position errors.

	Bartlett Processor	MV Processor	MUSIC Processor
Depth of Max.	110 m	110 m	110 m
Range of Max.	2493 km	2493 km	2493 km
Azimuth of Max.	171.7°	171.7°	171.7°
Power of Max.	-0.16 dB	-7.25 dB	-

The sidelobe structures were very similar to those of ideal simulation, but the peak value for the MV and for the MUSIC processor was much reduced from that of the ideal simulation. Although the mismatch reduces the dynamic range of the MV and MUSIC processors tremendously, the source was successfully located in range and azimuth with reduced power. The estimated source range was identical to the "true" source range with a minor discrepancy in the azimuth estimate. Unfortunately, the MUSIC processor failed to maintain the depth resolving power as in the ideal case. These simulated results suggest that slight float position error, i.e., less than one-tenth of the wavelength (10.7 m) might be the cause of the mismatch in depth and azimuth but cannot be held responsible for the mismatch in range.

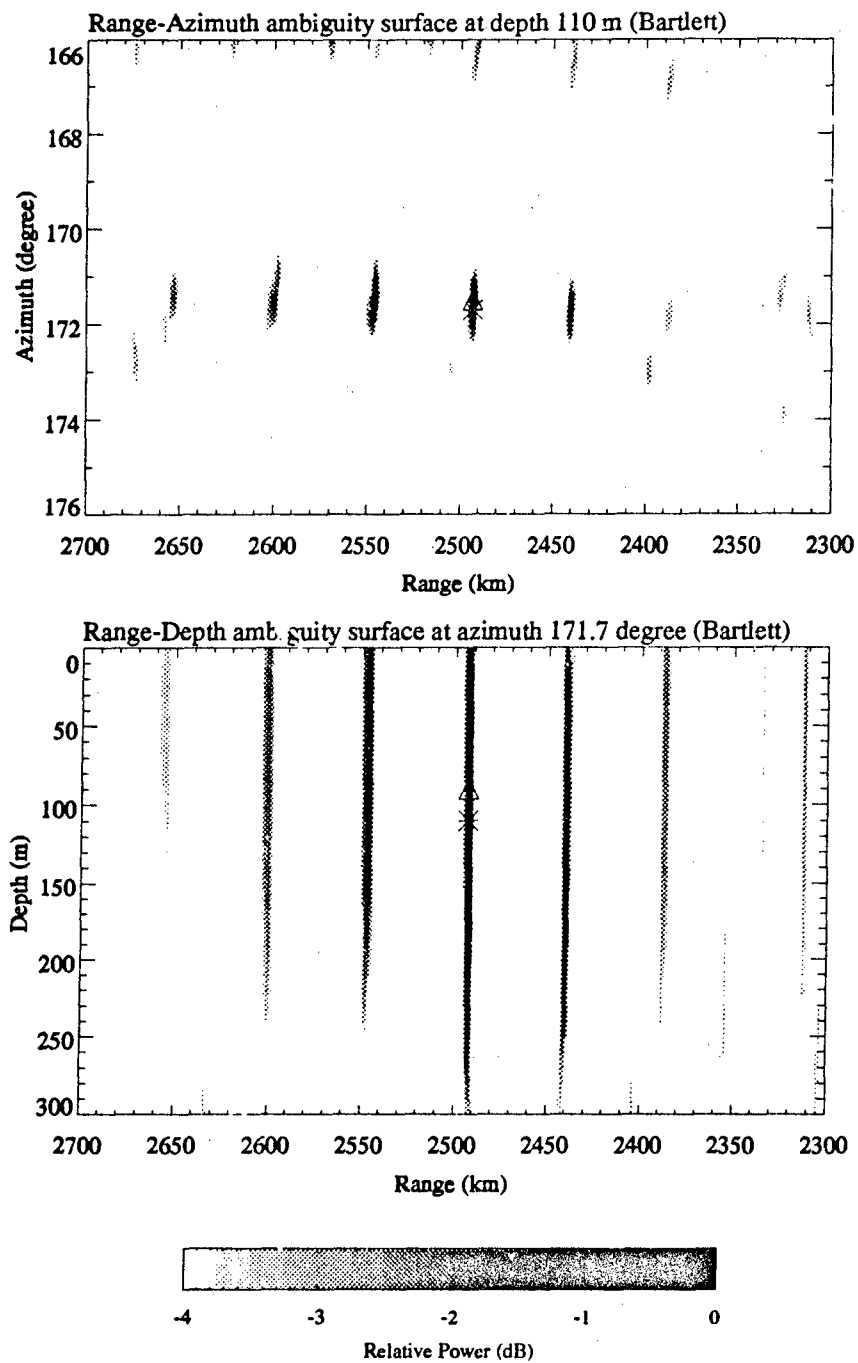


**Figure 4.15** Matched-field processing simulation of uncertainty in sensor positions using the Bartlett method.

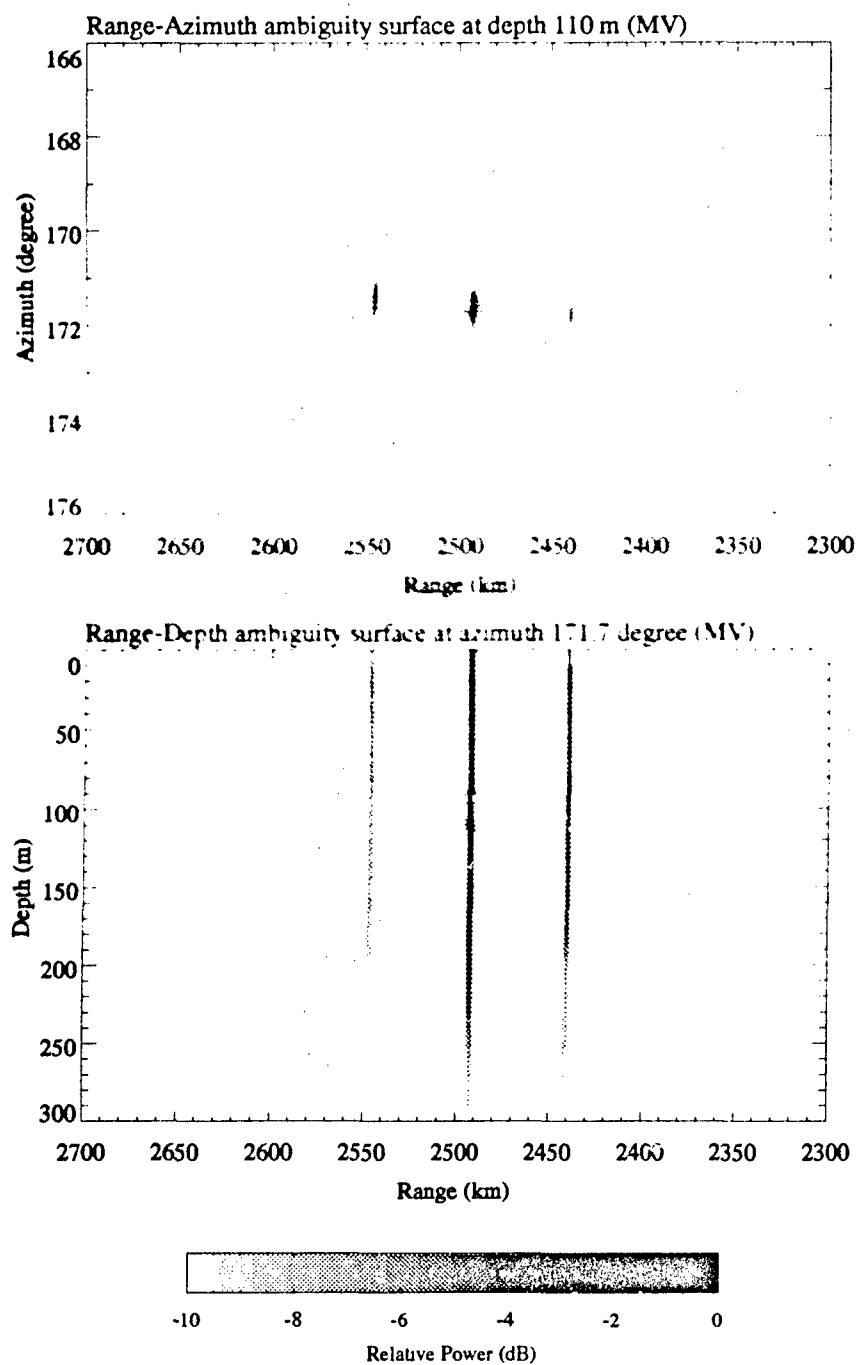


**Figure 4.16** Matched-field processing simulation of uncertainty in sensor positions using the MV method.

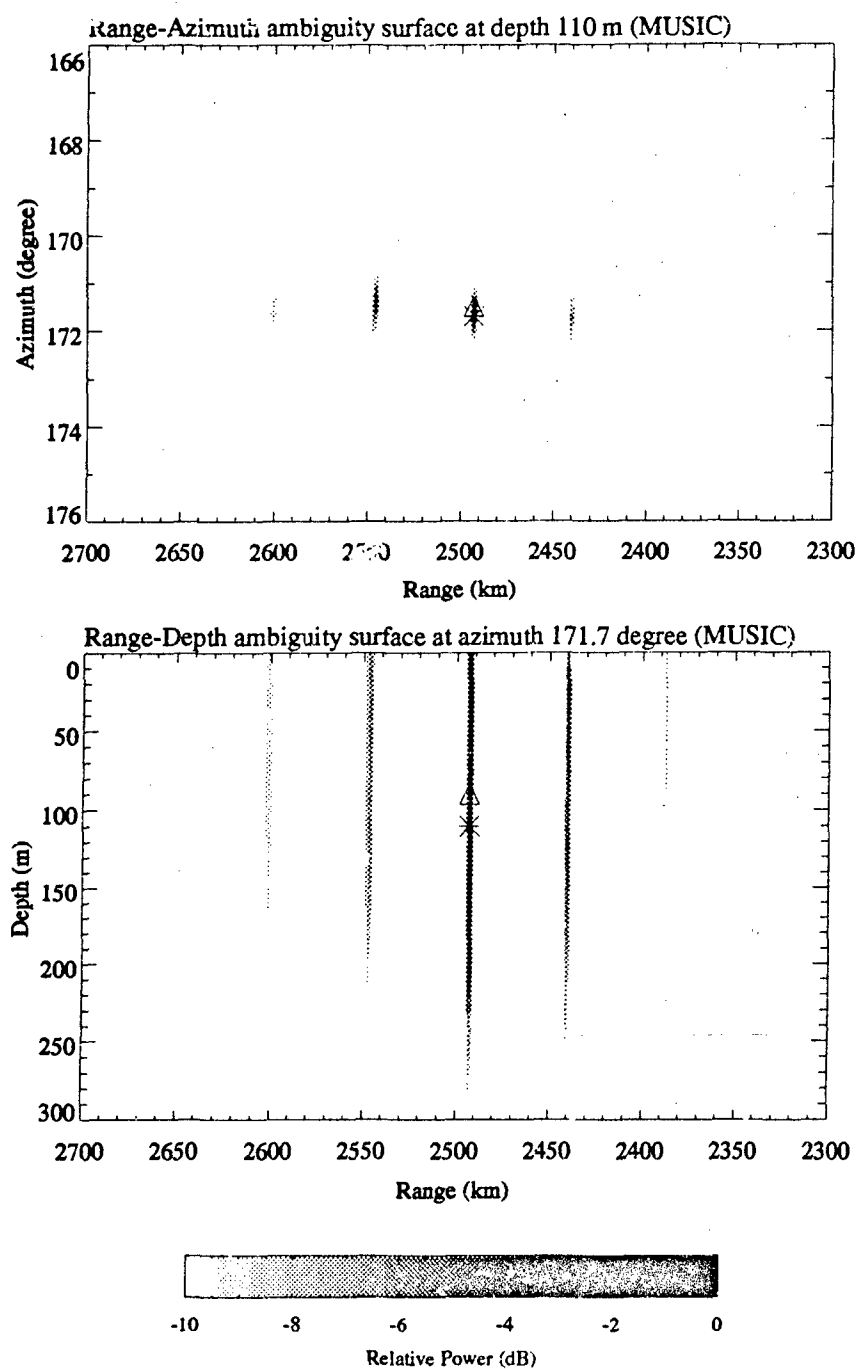


**Figure 4.17** Matched-field processing simulation of uncertainty in sensor positions using the MUSIC method.

#### 4.5.3 Uncertainty in Sound Speed Structure

We next studied the simulation of sound speed mismatch. The sound speed profiles collected during the experiment (refer to Figure 4.5) were modified by adding a linear function of the form [Porter et. al., 1937]:

$$\Delta c(z) = \frac{\delta(D-z)}{D} \text{ meter/second} \quad (4.9)$$

to the sound speed profiles collected between 140° W and 150° W. In this simulation, we used  $\delta = -3$  and  $D = 2000$  m so that at the surface, the sound speed was decreased by 3 meters/second, while below 2000 m, there was no change. This modification was justified by the fact that the sound speed profiles collected in this track were off the signal propagation path (refer to Figure 2.6). The replica vectors were generated using the original profiles while the simulated "acoustic data" were generated using the modified sound speed profiles reflecting (4.9).

The ambiguity surfaces for the sound speed mismatch simulation are plotted in Figures 4.18, 4.19 and 4.20, and the matched-field processing results are summarized in Table 4.6. The ambiguity

**Table 4.6** Matched-field simulation of sound speed mismatch.

	Bartlett Processor	MV Processor	MUSIC Processor
Depth of Max.	110	110	110
Range of Max.	2610	2610	2610
Azimuth of Max.	171.4°	171.4°	171.4°
Power of Max.	-0.5 dB	-10.7 dB	-

ity surfaces show the source peak shifted in range with much reduced power for the MV and MUSIC processors. The estimated source range is off by 117 km from the "true" source range, and the source azimuth is slightly shifted by 0.1°. These simulated results confirmed that uncertainty in sound speed structures can be held responsible for the large mismatch observed in the real-data ambiguity surfaces, particularly the range error.

#### 4.6 Summary

This chapter presented the results from the matched-field processing of data from 14-Hz cw collected by MPL's Swallow float array in a 1989 experiment. The data used to estimate the array covariance matrix were selected at time intervals during which the signal-to-noise ratio at the out-

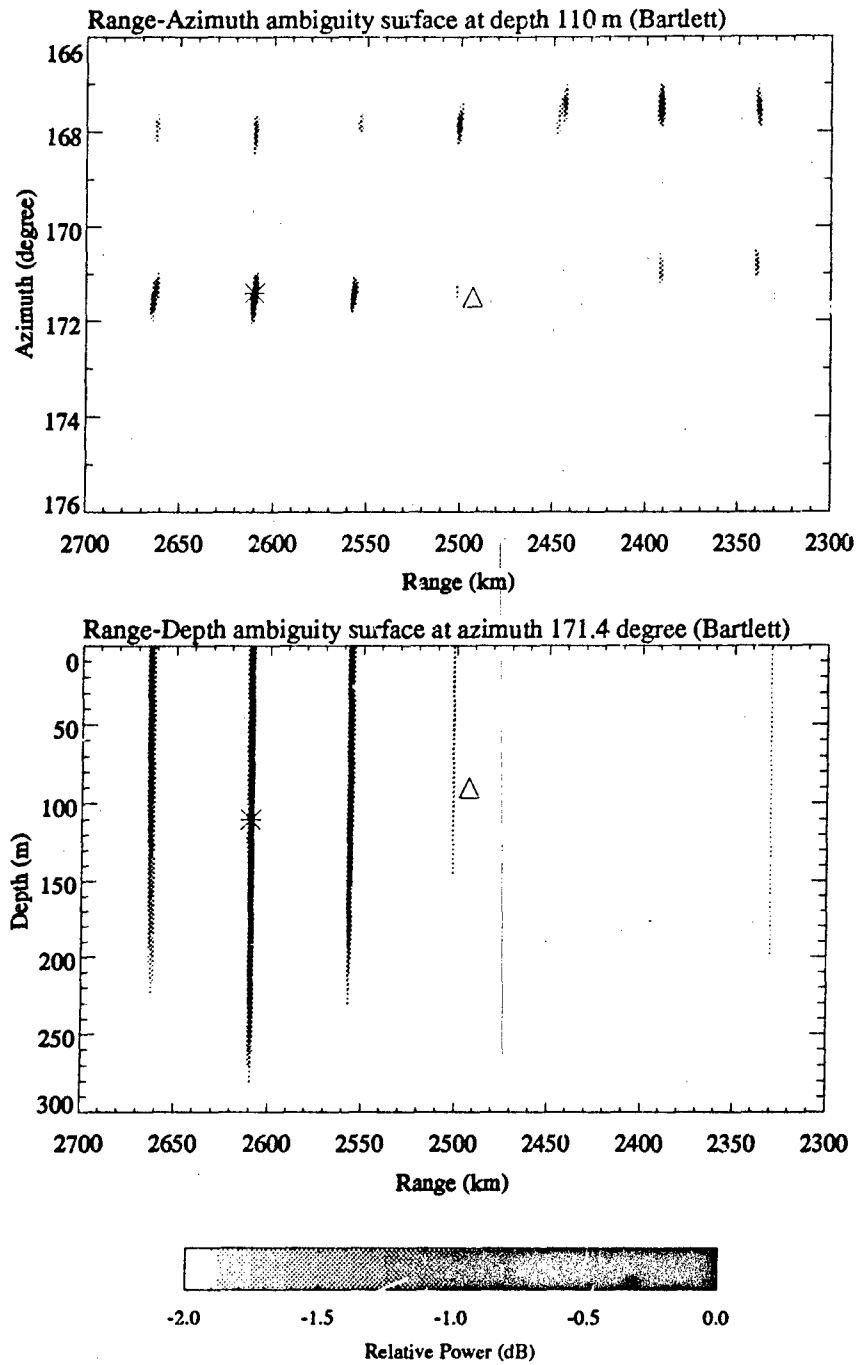


Figure 4.18 Matched-field processing simulation of uncertainty in sound speed structure using the Bartlett method.

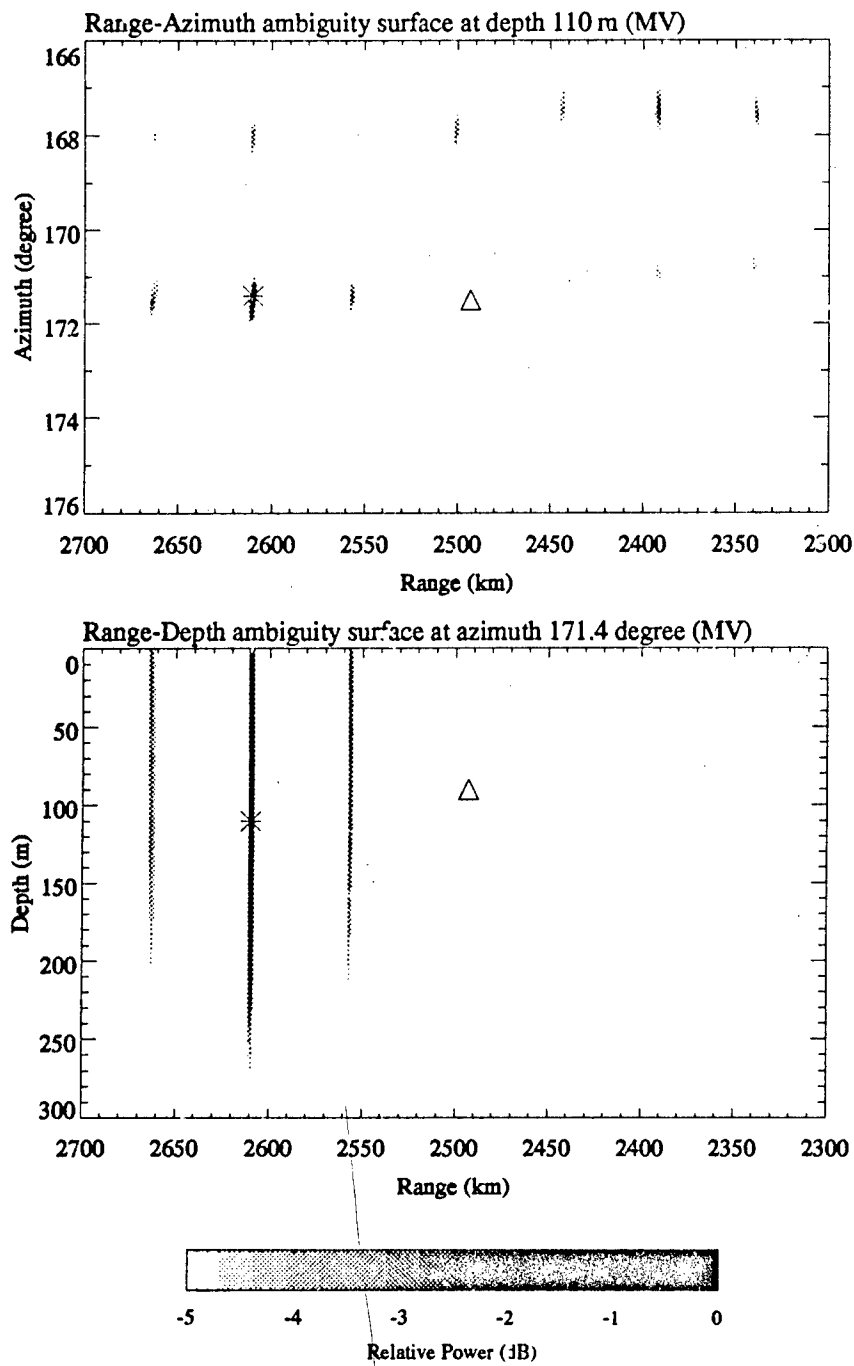
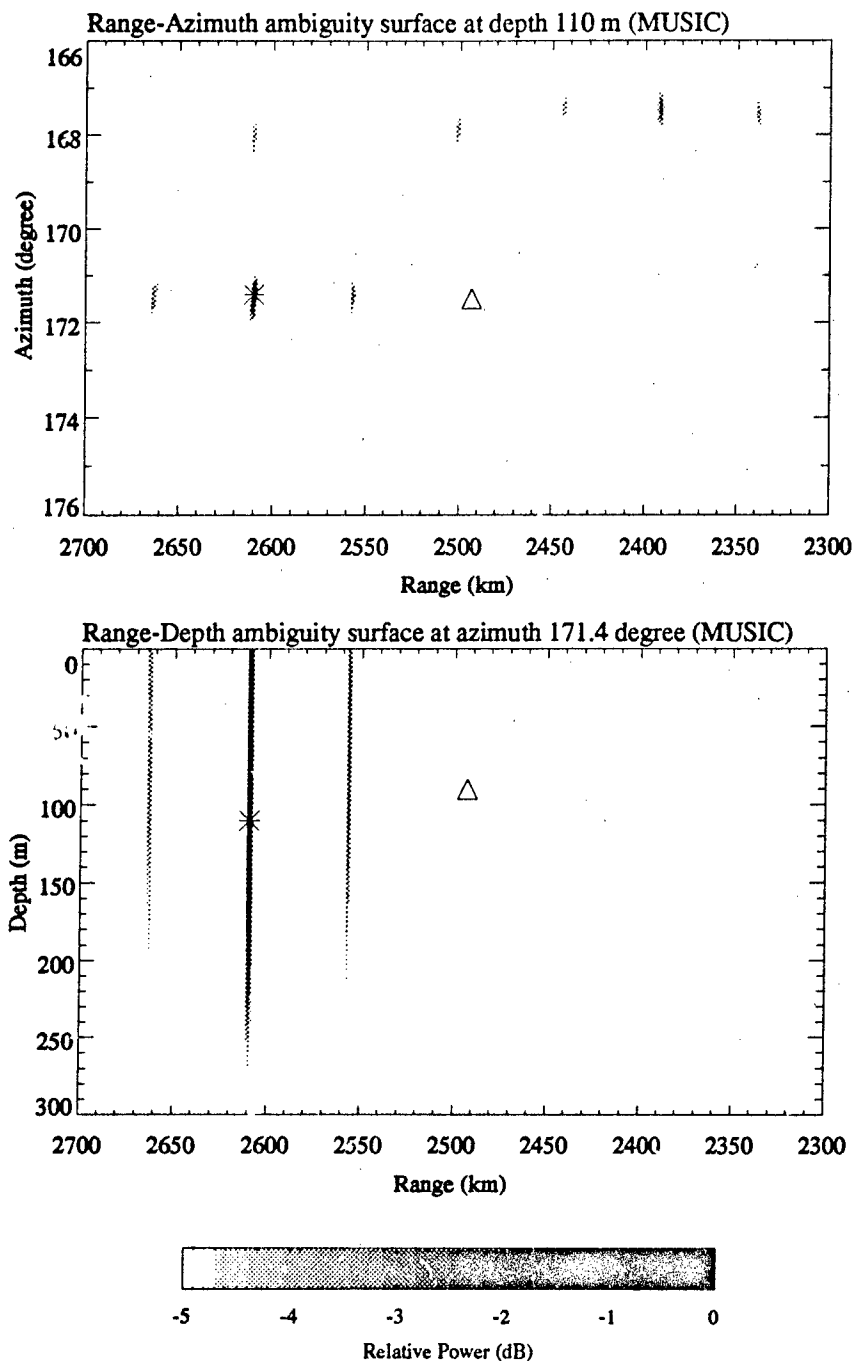


Figure 4.19 Matched-field processing simulation of uncertainty in sound speed structure using the MV method.



**Figure 4.20** Matched-field processing simulation of uncertainty in sound speed structure using the MUSIC method.



put of each individual float was high and the magnitude-squared coherence at source frequency was high among all floats. Eighty-four sound speed profiles derived from AXBT, XBT, and CTD measurements collected between  $34^{\circ} 50' \text{ N}$ ,  $122^{\circ} 20' \text{ W}$  and  $32^{\circ} \text{ N}$ ,  $150^{\circ} \text{ W}$  within 48 hours of the Swallow float experiment were input to an adiabatic normal mode model to compute the replica vectors. In spite of the presence of high sidelobes and grating lobes due to the sparse array, the matched-field ambiguity surfaces generated by all three MFP processor were consistent. While the azimuth estimate was quite successful, all three processors experienced difficulties in resolving the source depth, and all three exhibited errors in range estimates by three convergence zones. Controlled simulations were performed to aid in interpreting the real data processing results and confirmed that (1) depth resolution is indeed a difficult problem due to few modes propagating out to long range and due to a low source depth-to-wavelength ratio, (2) the range estimate is sensitive to uncertainty in sound speed structure, and (3) the azimuth estimate is robust. The environmental mismatch problem will be further investigated in chapter 5.

## 5. SELF-COHERENT MATCHED-FIELD PROCESSING

### 5.1 Introduction

Matched-field processing has been developed for localizing underwater acoustic sources by comparing acoustic data with predicted replica pressure fields. The inputs to MFP are the acoustic parameters of the ocean for predicting the replica pressure fields and the acoustic data received by an array of hydrophones. In order to compute the replica vectors for the matched-field processor, the knowledge of sound speed structure and bottom characteristics as a function of depth and range are required. As shown in the previous chapter, if the available environmental information is not sufficiently accurate (a situation referred to as mismatch) MFP can be degraded even if the signal-to-noise ratio is high. As an added complication, time-varying oceanographic features such as meso-scale eddies, ocean fronts, and internal gravity waves create fluctuations that result in the time-varying defocussing of the matched-field processor. Thus, calibration of the environmental parameters so as to improve the matched-processing performance is of special interest. This chapter investigates such an issue and is organized as follows. Section 2 reviews two approaches to the environmental mismatch problem reported in the literature. Section 3 proposes an approach to the environmental mismatch problem. Section 4 discusses the processing results using the proposed technique. Section 5 presents the chapter summary.

### 5.2 Literature Review

#### 5.2.1 Self-Cohering Technique

The self-cohering technique proposed by Bucker [Bucker, 1989; Tran and Hodgkiss, 1992] involves using a narrowband low frequency source at a known location in an imprecisely known oceanic environment. The essence of the self-cohering technique is to introduce a correction factor to the matched-field correlation formulation to compensate for the uncertainty in the ocean-acoustic environment so that the matched-field correlation between the received pressured fields and the replica vector is maximized. The correction factor has shown to be range-dependent and thus can be used to correct for the environmental parameters (i.e., the modal phases and the modal amplitudes) in a subsequent matched-field localization in search for other unknown source(s).

Recall that the modeled pressure field in a weakly range-dependent environment using adiabatic normal mode modeling is expressed as

$$p(r, z) = A \sum_{m=1}^M u_m(z_o; 0) u_m(z; r) \frac{\exp(i \int_0^r \xi_m dr)}{\sqrt{\xi_m(r) r}} \quad (5.1)$$

where  $z$  is the depth of the sensor,  $z_s$  is the depth of the source,  $r$  is the range of the source,  $u_m$  is the  $m^{th}$  mode eigenfunction,  $\xi_m$  is the  $m^{th}$  mode horizontal wave number, and  $M$  modes are used to model the acoustic pressure field.

If we express the Bartlett matched-field processor output power as

$$P = \left| \sum_{j=1}^J p_j^* \hat{p}_j \right|^2 \quad (5.2)$$

where  $J$  is the total number of sensors,  $p_j$  is the complex pressure measured at the  $j^{th}$  sensor, and the  $\hat{p}_j$  is the predicted complex pressure at the  $j^{th}$  sensor. Equation (5.1) can be substituted into (5.2), and the summations on the sensors and on the modes can be rearranged to yield

$$P = \left| \sum_{m=1}^M R_m^* S_m \right|^2 \quad (5.3)$$

where the first term corresponds to the receiving part

$$R_m^* = \sum_{j=1}^J p_j^* \frac{u_m(z_j, r)}{\sqrt{\xi_m(r)}} \quad (5.4)$$

and the second term corresponds to the source part

$$S_m = u_m(z_o; 0) \frac{\exp(i \int \xi_m dr)}{\sqrt{r}} \quad (5.5)$$

Correction factors for each mode  $C_m$  are introduced into the summation of Equation (5.3)

$$P = \left| \sum_{m=1}^M C_m R_m^* S_m \right|^2 \quad (5.6)$$

to maximize the correlation for each mode with respect to a source at known location  $(r_o, z_o)$ . Using this criterion, the correction factor  $C_m$  is given at the known source location by

$$C_m = \frac{R_m}{S_m} \quad (5.7)$$

where the known source range and depth  $(r_o, z_o)$  are used in Equation (5.5) to compute  $S_m$ . The correction factors are a function of range:

$$C_m(r) = |C_m(r_o)| \exp(i \frac{r}{r_o} \arg(C_m(r_o))) \quad (5.8)$$

It has been demonstrated in simulation that (5.8) calculated using a source at a known location can be used in search of other source(s) at a longer range.

### 5.2.2 Focalization Technique

Focalization [Collins and Kuperman, 1991] is an approach for reducing the problem of mismatch by treating the ocean as an acoustic lens that is out of focus and by adjusting the acoustic parameters until the source come into focus. This approach does not require a reference source but assumes the measured modal phases are available, although determining the measured modal phases can be difficult as pointed out by [Collins and Kuperman, 1991]. The focalization is performed by backpropagating the modeled modal phases using adiabatic normal mode approximation until the adiabatic modal phases match the measured modal phases. The simulated annealing optimization technique is used to search the modal phase parameter spaces via sound speed structure for the optimal values. It has been demonstrated by the focalization technique that the ocean parameters that bring the source into focus may not be unique; the focalization parameter search sometimes converges to the correct source location without converging to the correct environmental parameters.

## 5.3 Environment Adaptation Technique

In this section, we present an approach to the environment mismatch problem. We envision that, similar to the self-cohering technique by Bucker, the way that the environmental mismatch can be reduced is a two-phase process:

1. Adaptation phase: During this phase, a narrowband signal with frequency of interest at a known location is transmitted to probe the oceanic waveguide. The signal could be a surface ship of opportunity or a broadband source with good S/N on the frequency of interest such as air-deployed shots. The matched-field processor is configured in a feedback loop fashion as in Figure 5.1 to adjust the environmental parameters with the goal of causing the predicted pressure field to match the measured pressure field, i.e.,

$$\underset{\Gamma}{\text{maximize}} \quad P(r_o, z_o, \theta_o) \quad (5.9)$$

where  $\Gamma$  is the environmental parameter set, and  $P(r_o, z_o, \theta_o)$  is the matched-field processor output power due to source at a known location  $(r_o, z_o, \theta_o)$ .

2. **Localization phase:** When the environment adaptation phase is completed, the optimized environmental parameter set  $\Gamma_{opt}$  is then used to compute the replica pressure fields and normal matched-field processing can resume to search for an unknown target of interest in the vicinity of the reference source.

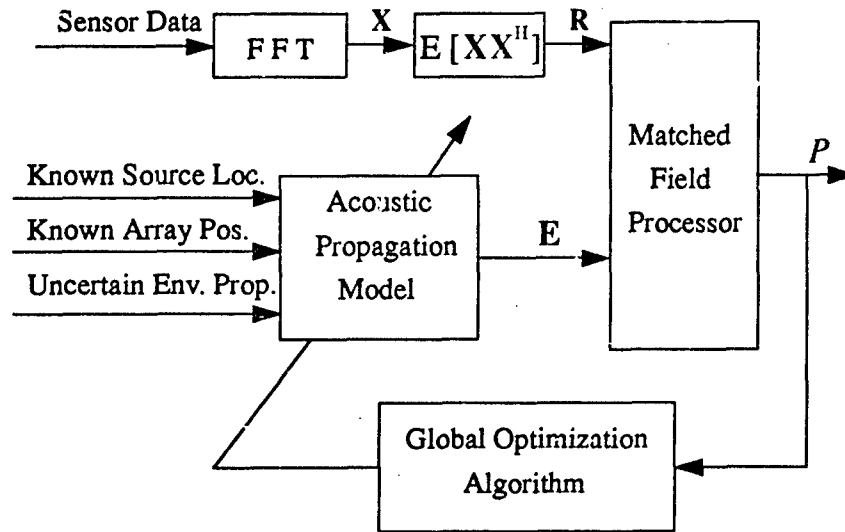


**Figure 5.1** Environment adaptation technique block diagram.

In this study, two types of environmental parameters, sound speed structure and horizontal wavenumber, are considered. We use matched-field processor output as a performance function or cost function, since the cost function  $P$  is nonlinear and may have many local maxima (or local minima if we use the negative of  $P$  as the cost function); a global optimization technique is required for searching the optimum environmental parameters. This section presents the global optimization method while the processing results using the environment adaptation technique are given in the next section.

### 5.3.1 Global Optimization Method

In this section we present an efficient global optimization method for searching the environmental parameter spaces. The method is based on the conventional simulated annealing tech-

nique. A detailed description of the technique is given in [Kirkpatrick et. al., 1983]. For completeness, the motivation and a brief description of the algorithm are given here.

### 5.3.1.1 Motivation

Traditionally, optimization problems are often treated by the iterative improvement method such as gradient search. Iterative improvement starts at some initial state, or set of values for the variables. Then successive small changes in the state are made in such a way that the cost function is decreased at each step. The moves from one state to another are effected by some procedure. This process continues until there are no moves that reduce the cost function. At this point we have found a minimum. Often, however, it is a local rather than a global minimum if the performance surface of the functional is multi-modal. A direct response to this problem is to perform iterative improvement from several initial states and select the best of the resulting local minima. The simulated annealing algorithm is a more effective method that avoids this pitfall by allowing "hill climbing" moves with probability. That is, it may accept moves that generate a cost function with a higher cost than the current one; thus it can pull itself out of the local minima and potentially fall into a more promising down-hill path.

The simulated annealing is suggested by an analogy between the search for a minimum in a cost function and the physical process by which a material changes states while minimizing its energy. In this analogy, a random initial state (or set of parameter values) in the optimization corresponds to the melted state, and local minima in the cost function relate to the formation of different crystal structures once the material freezes into a solid. In metallurgy, a technique called annealing is often used, where a very fine crystal is obtained through gradual cooling. Too rapid a cooling schedule results in a coarse structure, similar to a poor local minimum in an optimization. The correspondence between the two processes was first introduced by [Metropolis et. al., 1953].

### 5.3.1.2 Simulated Annealing Algorithm

For a system to be optimized, a cost function  $E$  is first established and a dynamic variable  $T$ , the "temperature" of the system, is chosen to control the process. Starting at a high temperature, the system is slowly cooled down until the system "freezes" and reaches the optimum state in a manner similar to the annealing of a crystal during growth to reach a near-perfect structure. At each "temperature," a change in the system state is made according to a certain rule, and then the "energy" or "cost" change of the system  $\Delta E$  is calculated. If  $\Delta E \leq 0$ , the system state alteration is accepted, and the process is continued. If  $\Delta E > 0$ , then the system state alteration is accepted with probability defined as  $\exp(-\frac{\Delta E}{kT})$ , the well-known Boltzmann probability distribution in thermodynamics. In the optimization problem, the quantity  $k$  is a constant, and its dimension depends on the dimensions of  $\Delta E$  and  $T$ . Then a random number  $\chi$  uniformly distributed in the interval  $[0,1]$  is chosen. If  $\chi \leq \exp(-\frac{\Delta E}{kT})$ , the change of system state is accepted; on the other hand, if

$\chi > \exp(-\frac{\Delta E}{kT})$ , the change is discarded, that is, the system state before change is used for the next step of the process. This procedure is repeated for each temperature until the system is optimized by arriving at a global energy minimum. The choices of initial temperature  $T_0$  and the cooling schedule are crucial for the success and the speed of convergence of the simulated annealing process. Due to the probabilistic Boltzmann selection rule of the  $\Delta E > 0$  case, the process can always get out of a local minimum of the cost function in which it could get trapped and proceed to the desired global minimum. This makes simulated annealing different from the iterative improvement procedure. To make use of the annealing algorithm for the optimization problem, one needs to provide the following basic components [Press et. al., 1988]:

1. A cost function  $E$  whose minimization is the goal of the procedure.
2. A model of what a legal set of parameter values is. This model represents the possible problem solutions over which we will search for a good answer.
3. Generators of random changes in the system state to determine how many variables and which variables will be altered and how many perturbations there will be to the current values of the selected variables.
4. A control parameter  $T$  and an annealing (or cooling) schedule. Specifically, we need a starting hot temperature (or a heuristic for determining a starting temperature for the problem) and rules to determine when the current temperature should be lowered, by how much the temperature should be lowered, and when annealing should be terminated.

#### 5.3.1.3 Fast Simulated Annealing Procedure

Our implementation of the simulated annealing algorithm simply uses the negative of the matched-field output power as the energy (or cost function) to be minimized, and sound speed or modal wave number EOF coefficients as the environmental parameters to be varied (refer to section 5.3.2) during the annealing process. We use a random-number generator with Poisson distribution to determine the number of parameters to be changed; a random-number generator with uniform distribution to select the parameters to be varied; and a random-number generator with Cauchy distribution to generate the perturbations for the selected variables. The merit of the Cauchy distribution is that it has a Gaussian-like peak and Lorentzian tails that imply more often large perturbations in the step space among dense small perturbations around the current parameter(s) that allow(s) fast escape from the local minima and fast convergence. As a result of using the Cauchy generating density, we adopted a fast annealing schedule suggested by [Szu and Hartley, 1987] which is inversely linear in time, i.e.,  $T_i = T_0 / i$ , where the  $T_0$  is the initial starting temperature, and  $i$  is the iteration number (note that the conventional simulated annealing algorithm uses a Gaussian distribution to generate the perturbations, and it has been proven by [Ge-

man and Geman, 1984] the cooling schedule must be inversely proportional to the logarithm of iteration  $i$  in order to guarantee convergence to a global minimum, i.e.,  $T_i = T_0 / \log i$ ).  $T_0$  is determined empirically to give good results. In practice, the starting temperature is chosen to give a high accept rate when  $\Delta E > 0$ . Lastly, the stopping criterion is to terminate annealing when the cost improvement seen across successive temperatures is sufficiently small. The fast simulated annealing algorithm for this study is encapsulated in the following procedure:

1. Set the initial temperature  $T_0$  to a large value.
2. Determine the number of parameters needed to be perturbed using Poisson distribution with a selection rate of 1.
3. Generate the perturbations for the selected parameter(s) using Cauchy distribution.
4. Perturb the current parameter set and compute the new cost,  $E_i$ .
5. If  $E_i < E_{i-1}$ , then accept the new parameter set and proceed to (7).
6. If  $E_i > E_{i-1}$ , then accept the new parameters with a probability given by the Boltzmann distribution.
7. Decrease the temperature according to the fast cooling schedule and repeat the procedure; terminate the procedure when no new parameters are accepted for a large number of iterations.

### 5.3.2 Reducing the Parameter Search Spaces

For optimization methods, an efficient parameterization to reduce the parameter search space leads to fast convergence and more uniqueness in the solution. Thus we would like to characterize the environment of interest in as few parameters as possible yet in a meaningful way. A common method from statistics for analyzing data is principal component analysis. The essence of this method is to find a set of  $K$  orthogonal vectors in data space that account for as much as possible of the data's variance. Projecting the data from their original  $N$ -dimensional space onto the  $K$ -dimensional subspace spanned by these vectors then performs a dimensionality reduction that often retains most of the intrinsic information in the data. Typically,  $K \ll N$ , thus making the reduced data much easier to handle.

Similar to the principal component analysis method, oceanographers have developed a method for deriving efficient basis functions, known as empirical orthogonal functions (EOFs), for measured physical quantities such as temperature, salinity, or sound speed as a function of depth [Davis, 1976; Tolstoy et al., 1991]. In an effort to reduce the ocean-acoustic parameter spaces,



one can describe the parameter set as a sum of EOFs. The EOFs are defined as the eigenvectors  $V_i$  of the parameter covariance matrix  $R$ :

$$R V_i = \lambda_i V_i \quad (5.10)$$

where  $\lambda_i$  is the  $i^{th}$  eigenvalue or the variance associate with  $V_i$ . The covariance matrix for the environmental data  $R$  is defined as

$$R = E[\tilde{\Gamma} \tilde{\Gamma}^T] \quad (5.11)$$

where  $\tilde{\Gamma} = \Gamma - E[\Gamma]$ , and  $\Gamma$  is the measured environmental parameter values.  $E[\ ]$  is the expectation (average) operator.

Any one of the environmental parameter sets used in estimating the covariance matrix can be represented or spanned as a linear combination of appropriate eigenvectors:

$$\hat{\Gamma} = E[\Gamma] + \sum_{n=1}^N \alpha_n V_n \quad (5.12)$$

where  $N$  is the total number of eigenvalues, and the  $V_n$ 's are indexed so that  $\lambda_n \geq \lambda_{n+1}$ . The merit of using the EOFs to reduce the parameter search spaces is twofold:

1. If we express the true parameter set in terms of some functional expansions:

$$\Gamma_{true} = E[\Gamma] + \sum_{n=1}^N \beta_n F_n \quad (5.13)$$

then for a fixed number of functions  $K < N$ , no approximate representation of the parameter set

$$\hat{\Gamma} = E[\Gamma] + \sum_{k=1}^K \beta_k F_k \quad (5.14)$$

can produce a lower mean-square error  $E[(\Gamma_{true} - \hat{\Gamma})^T (\Gamma_{true} - \hat{\Gamma})]$  than is obtained using  $F_k = V_k$  according to the least-squares principle [Davis, 1976]. In practice, a high degree of accuracy can be achieved with only two or three EOFs for ocean-acoustic parameters [LeBlanc and Middleton, 1980].

2. The covariance matrix calculated from measurements is a complete summary of the manner in which the environment varies. This matrix reveals the inter-statistical dependence between parameters. Thus the spanned parameter set is meaningful since the physics governing the process that generates the parameter set is preserved.

Using the EOF approach to parameterize the environment, (5.9) can now be expressed as

$$\begin{aligned} & \text{maximize} && P(r_o, z_o, \theta_o) \\ & \{\alpha_k, k=1, K\} \end{aligned} \quad (5.15)$$

where  $\alpha_k$  is related to  $\Gamma$  by

$$\Gamma = E[\Gamma] + \sum_{k=1}^K \alpha_k V_k \quad (5.16)$$

## 5.4 Processing Results

The environment adaptation technique described above is first applied to simulation data and then used to process data collected with the Swallow float array that was deployed in the North-east Pacific in July 1989.

### 5.4.1 Simulation

To make the simulation as realistic as possible, we modeled the source-array geometry corresponding to the July 1989 experiment with a 14-Hz source deployed at the locations according to the R/V Aloha source log. The freely drifting sensor array geometries corresponding to the navigation results during the three time intervals, i.e., 01:47, 04:38, and 07:32 PST July 9, 1989 were used in the simulation study.

To simulate the environmental mismatch, similar to that of the last chapter, we modified the profiles between 34° N, 140° W and 32° N, 150° W by adding a function of the form:

$$\Delta C(z) = C_{34^\circ N, 140^\circ W}(z) - C_{\text{mean}}(z) \text{ meter/second} \quad (5.17)$$

where  $C_{34^\circ N, 140^\circ W}$  is the sound speed profile taken at 34° N, 140° W, and  $C_{\text{mean}}$  is the mean profile between 34° N, 140° W and 32° N, 150° W (refer to the solid line in Figure 5.8(b) for the shape of  $\Delta C(z)$ ). This modification was justified by the fact that the sound speed profiles collected in this track were off the signal propagation path (refer to Figure 2.6). The simulated "acoustic

data" were generated with an adiabatic normal mode model using the sound speed profiles reflecting (5.17), while the replica vectors were generated using the original measured sound speed profiles. As in section 4.5, we ignored the bottom effect due to long-range propagation; only the first 16 non-bottom interacting modes were used in the calculation of the replica vector and the simulated data. Throughout this chapter, the MUSIC matched-field processor was used to compute the ambiguity surfaces due to its high-resolution capability. For comparison, both ambiguity surfaces for the ideal case (no mismatch) and the mismatched case during the three time intervals are plotted in Figure 5.2 and Figure 5.3, respectively. The  $\Delta$ 's are the "true" source locations according to the source log, and the \*'s are the MFP estimated source locations i.e., the highest peak in the ambiguity surfaces. As expected, the estimated source locations using the mismatched environment were off in range by roughly 100 km to 150 km (2 to 3 CZs) for all three time intervals.

#### 5.4.1.1 Sound Speed Adaptation

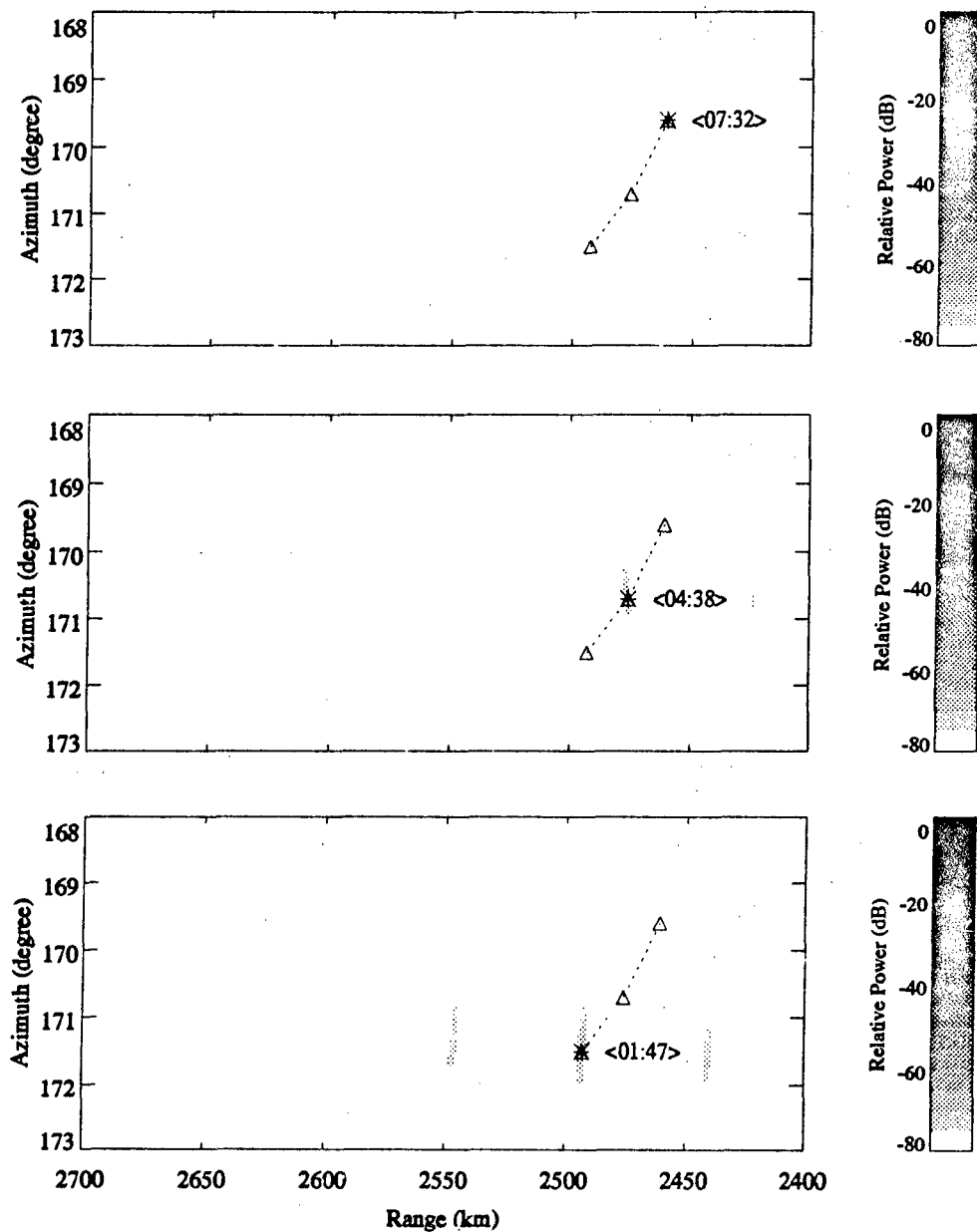
We now proceed to the environment adaptation technique and assume that the source-array geometry is known exactly during the first time interval (01:47). The first simulation case is to invert for the range-independent sound speed profile representing the environment along the signal propagation path between 140° W and 150° W (refer to Figure 2.6), in a matched-field sense. This range-independent approximation is justified by the fact that this part of the ocean is environmentally benign, and the range dependency is relatively weak as seen in Figure 4.5.

Figure 5.4 (a) shows the excess (demeaned) sound speed profiles derived from 30 AXBT measurements made between 34° N, 140° W and 32° N, 150° in the Northeast Pacific in July 1989. Table 5.1 lists the five largest eigenvalues obtained through eigen-decomposition of the sound

**Table 5.1** The five largest eigenvalues obtained from eigen-decomposition of the sound speed covariance matrix.

Number	Eigenvalue
1	54.06
2	35.96
3	11.93
4	2.81
5	1.81

speed covariance matrix. As can be seen, only the first few eigenvalues are significant. We thus use the eigenvectors or EOFs corresponding to the two largest eigenvalues in spanning the search spaces. Normalized versions of the EOFs corresponding to the two largest eigenvalues are shown as solid and dotted curves, respectively, in Figure 5.4(b). The eigenvalues or variances corre-



**Figure 5.2** Matched-field simulation (no mismatch) of 14-Hz source for the three time intervals corresponding to the experimental data collected during 1989 experiment.

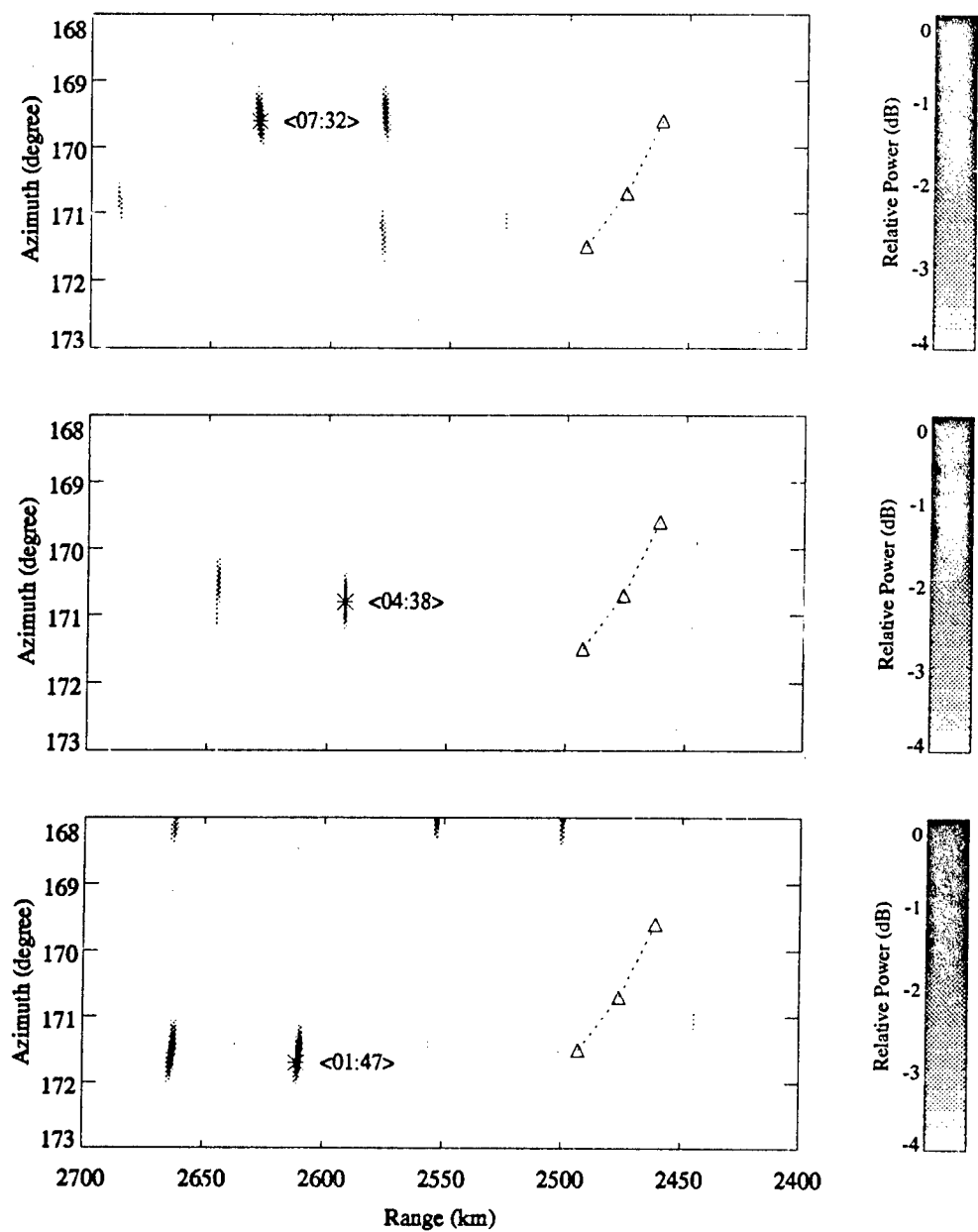


**Figure 5.3** Matched-field simulation of environmental mismatch for the three time intervals corresponding to the experimental data collected during 1989 experiment.

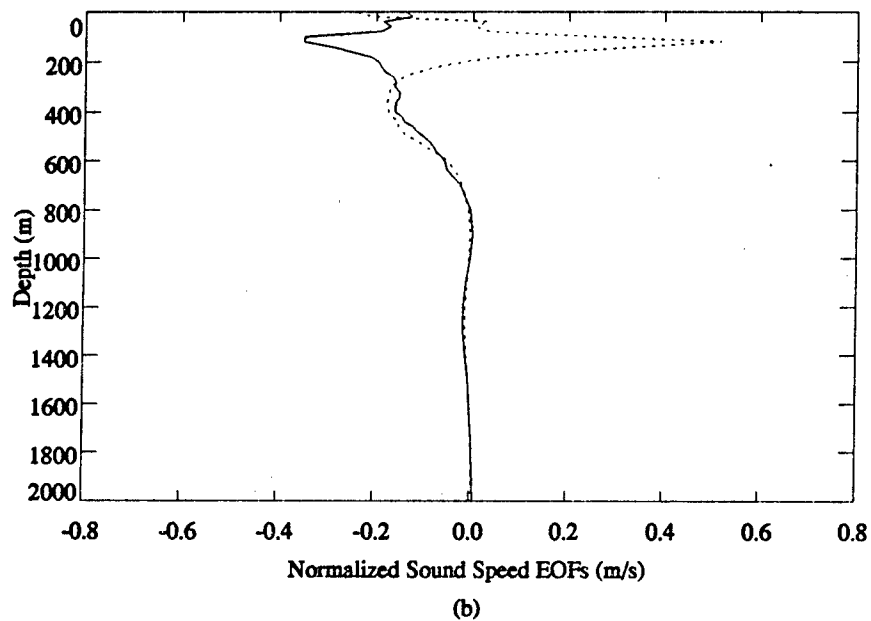
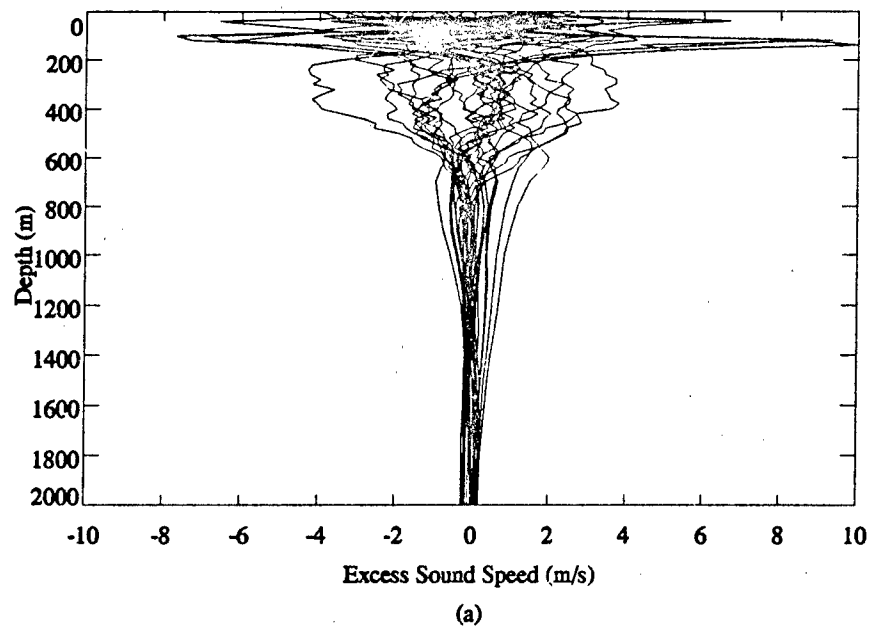


**Figure 5.4** (a) Excess (demeaned) sound speed profiles computed from 30 AXBT measurements made between  $140^{\circ}$  W and  $150^{\circ}$  W, July 1989, (b) Normalized versions of the first and second EOFs derived from (a).

sponding to these EOFs were  $\lambda_1 = \sigma_1^2 = 54.06$  and  $\lambda_2 = \sigma_2^2 = 35.96$ , respectively. To ensure all possible parameter values are reachable in the search spaces, we allow the values of the EOF coefficients to vary within  $\pm 6\sigma_n$ . Using the mean sound speed profile, the first two EOFs, and the initial solution of the EOF coefficients of (0,0), the optimization is performed with the fast simulated annealing procedure. Figure 5.5 shows the convergence properties of a typical annealing run. In this example, the temperature was initialized at 200 and was reduced to 0.2 over 1000 iterations. The first and second panels are the trajectories of the EOF coefficients while the third panel is the cost function learning curve as the annealing proceeds. As expected, the cost function learning curve declines as the iteration goes on, but occasionally the curve increases to a higher energy state thus indicating the escaping out of the local minima. After 350 iterations, the optimization process converges to the minimum energy state, and the solution of the EOF coefficients found at the 1000th iteration is (9.00, 21.91). To validate the optimal solution, the energy (cost function) surface as a function of the EOF coefficient values is calculated exhaustively on a regular grid in  $\alpha_1$  and  $\alpha_2$  (with a grid size of 1) bounded by [-50,50], which corresponds to 10201 evaluations of the cost function as displayed in Figure 5.6. The surface shows a global minimum at  $\alpha_1 = 9$ ,  $\alpha_2 = 22$  with numerous local minima scattering around. The joint trajectories of the EOF coefficients as the annealing proceeds are overlaid on the energy surface plot. A good agreement between the solutions obtained by grid search and optimization is observed. It is of interest to know whether the optimal solution of the EOF coefficients varies from run to run. The environment adaptation procedure is then repeated for nine times, each time with 1000 iterations. The joint trajectories of the EOF coefficients for the nine runs are plotted in Figure 5.7, and the corresponding solutions are given in Table 5.2. The convergency properties and the consistent agree-

**Table 5.2** Optimization results from nine runs using sound speed EOF coefficients as search parameters.

Run	EOF Coef. #1	EOF Coef. #2
1	9.01	21.88
2	8.96	21.85
3	8.72	22.00
4	8.92	21.89
5	9.09	21.93
6	9.05	21.88
7	9.00	21.97
8	9.05	21.74
9	8.82	22.02

ment among all runs are again observed, which confirms the fitness of the global optimization algorithm.

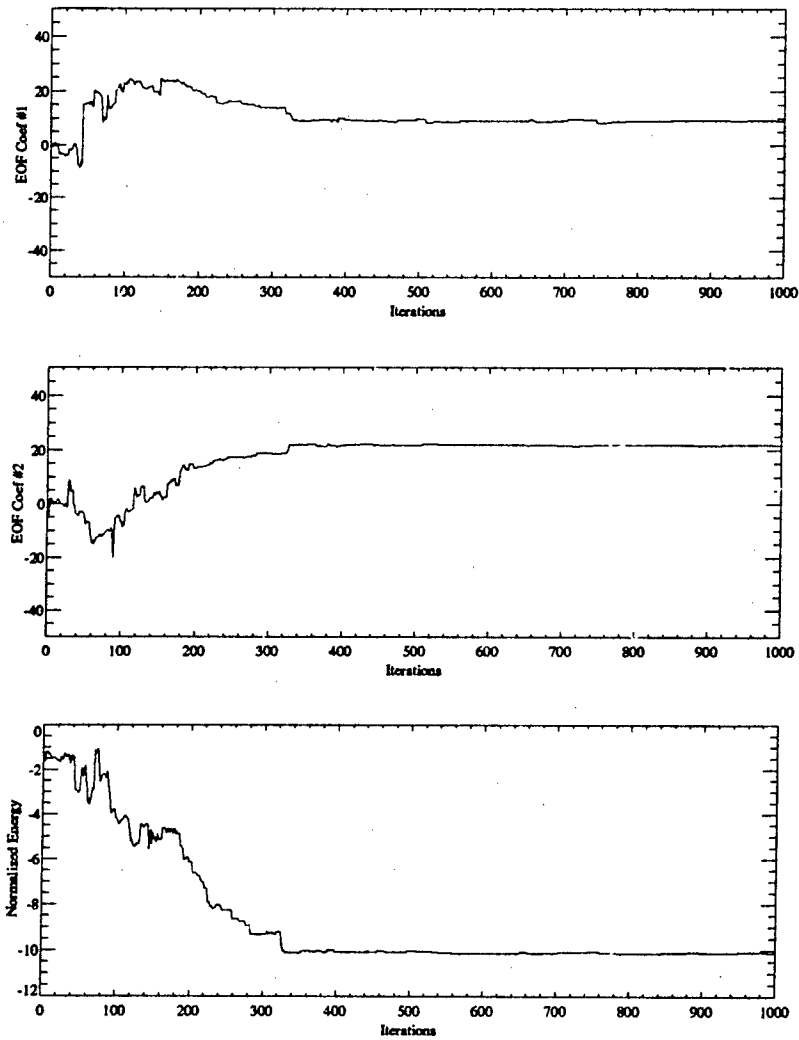


**Figure 5.5** Trajectories of the sound speed EOF coefficients and cost function learning curve for a typical annealing run.



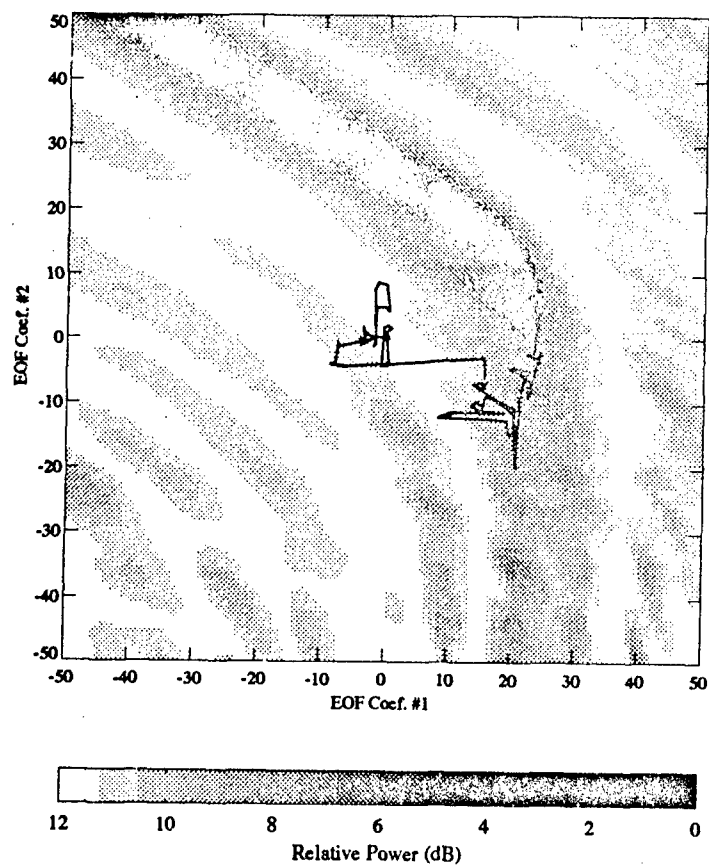


**Figure 5.6** Energy surface as a function of sound speed EOF coefficients computed by exhaustive search (simulation).

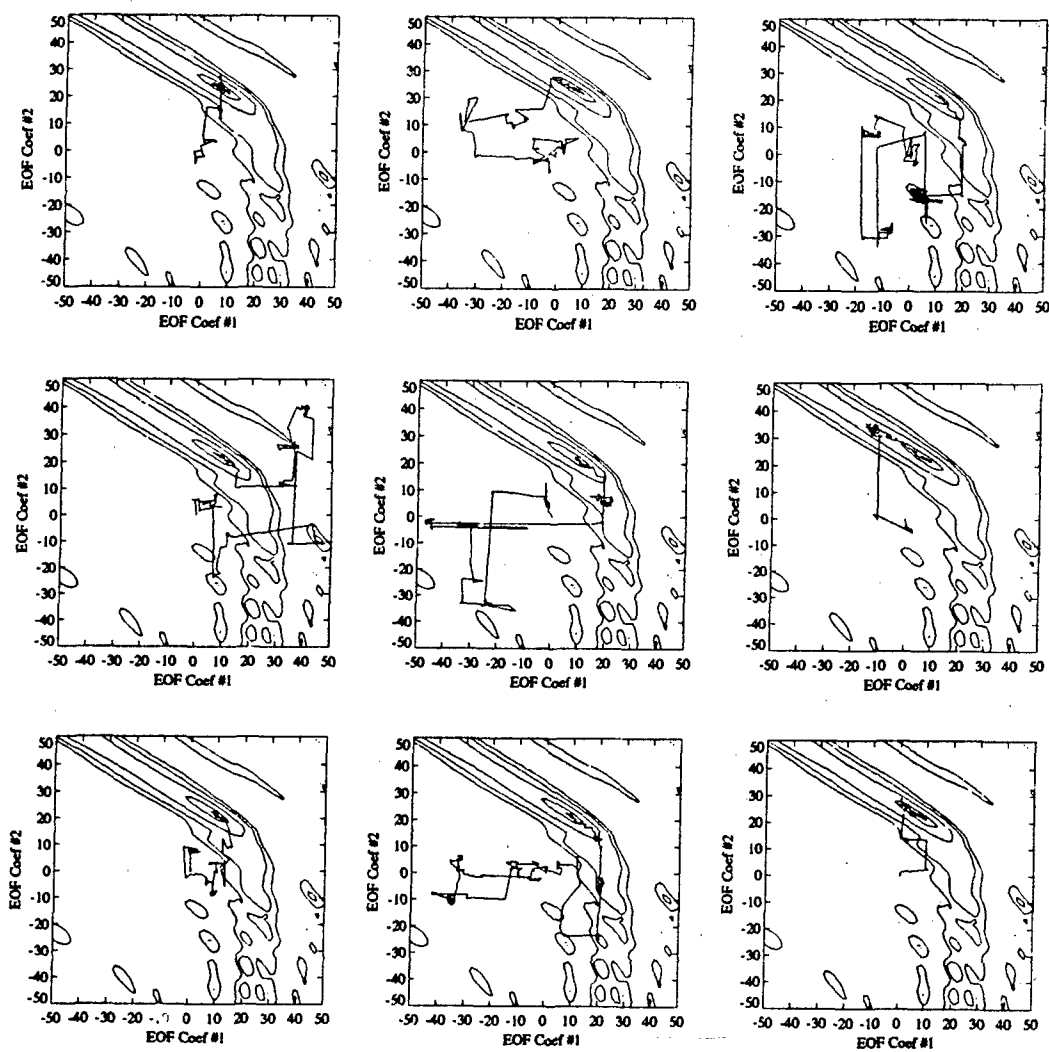


Figure 5.7 Joint trajectories of sound speed EOF coefficients for different annealing runs.

The adapted sound speed profile derived from the mean profile and the two EOF coefficients found at the 1000th iteration is plotted by dotted line in Figure 5.8. For comparison, the modified sound speed profiles (i.e., the "true" profiles) used to simulate the "acoustic data" are averaged and plotted by solid line, and the measured profiles that were used to model the replica vectors are averaged and plotted by dashed line. As can be seen, the adapted profile tracks the "true" profile closely. We now proceed to the localization phase of the technique. The measured sound speed profiles between 140° W and 150° W are replaced by the single adapted sound speed profile, and normal matched-field processing resumes. Figure 5.9 shows the optimized range-azimuth ambiguity surfaced for all three time intervals. The optimized (or self-cohered) source locations match those of an ideal simulation (no mismatch).

#### 5.4.1.2 Wave Number Adaptation

The second implementation of the environmental adaptation technique is to invert for the modal wave numbers at the source frequency (14 Hz) for the acoustic waveguide of interest. The assumptions and conditions are identical to the sound speed adaptation case with one exception, that is, the modal wave number EOF coefficients are now the search parameters. To compare these two implementations, we followed exactly the same path of investigation. Figure 5.10(a) shows the excess (demeaned) wave number estimates of the modal wave number at the source frequency (14 Hz) obtained from 30 AXBT measurements made in July 1989. Table 5.3 lists the five largest eigenvalues obtained through eigen-decomposition of the wave number covariance matrix. Normalized versions of the EOFs corresponding to the two largest eigenvalues are shown

**Table 5.3** The five largest eigenvalues obtained from eigen-decomposition of the wave number covariance matrix.

Number	Eigenvalue
1	$1.43 \times 10^{-9}$
2	$1.06 \times 10^{-10}$
3	$4.06 \times 10^{-11}$
4	$4.53 \times 10^{-12}$
5	$2.00 \times 10^{-12}$

as solid and dashed curves in Figure 5.10(b). Note that the lag in the wave number covariance matrix estimate is now the mode instead of the depth. Optimization is performed using the fast simulated annealing algorithm. Figure 5.11 shows the trajectories of the wave number EOF coefficients and the cost function learning curve for a typical run. Figure 5.12 shows the energy surface computed by exhaustive search and the joint trajectories of the wave number EOF coeffi-

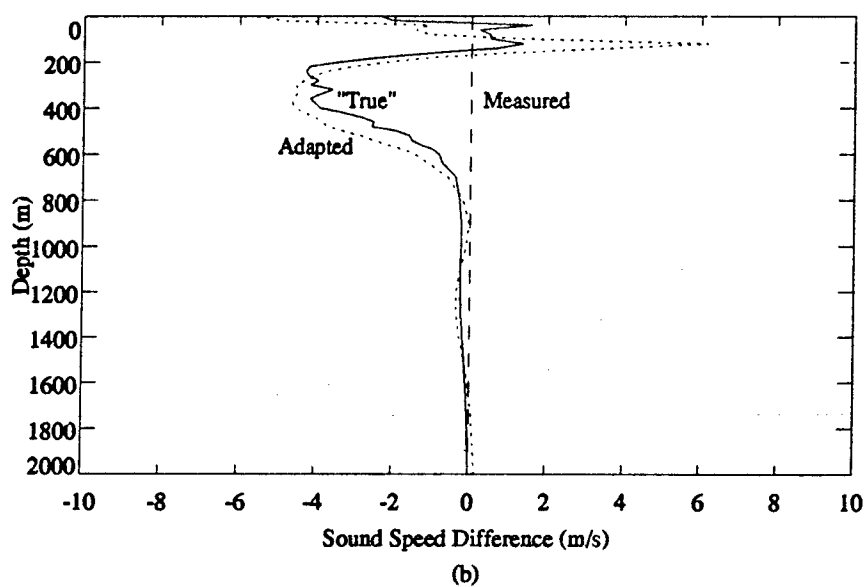
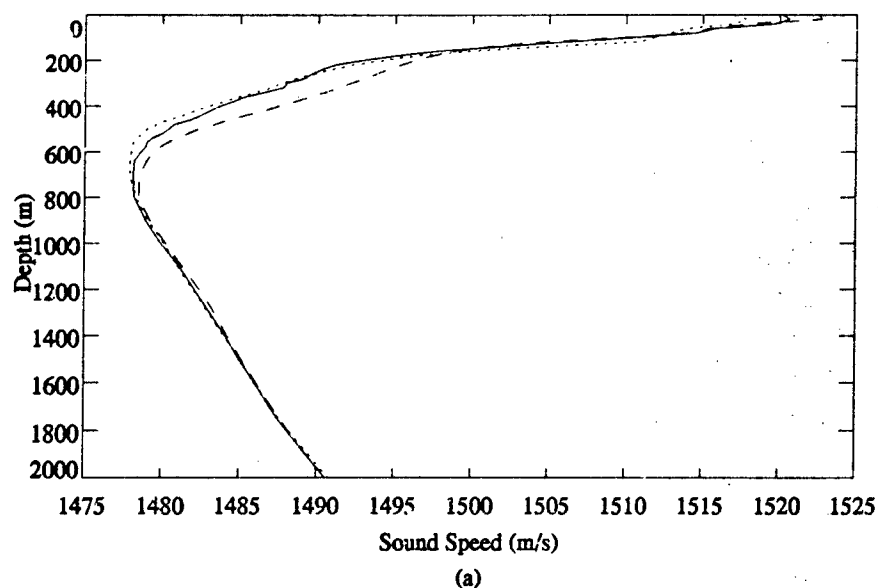


**Figure 5.8** (a) Sound speed profile derived from the environment adaptation technique (dotted line), "true" profile (solid line), and measured sound speed profile (dashed line); (b) the difference version of (a), i.e., using the measured profile as reference (dashed line), the "true" minus the measured and the adapted minus the measured are in solid and dotted lines, respectively (simulation).

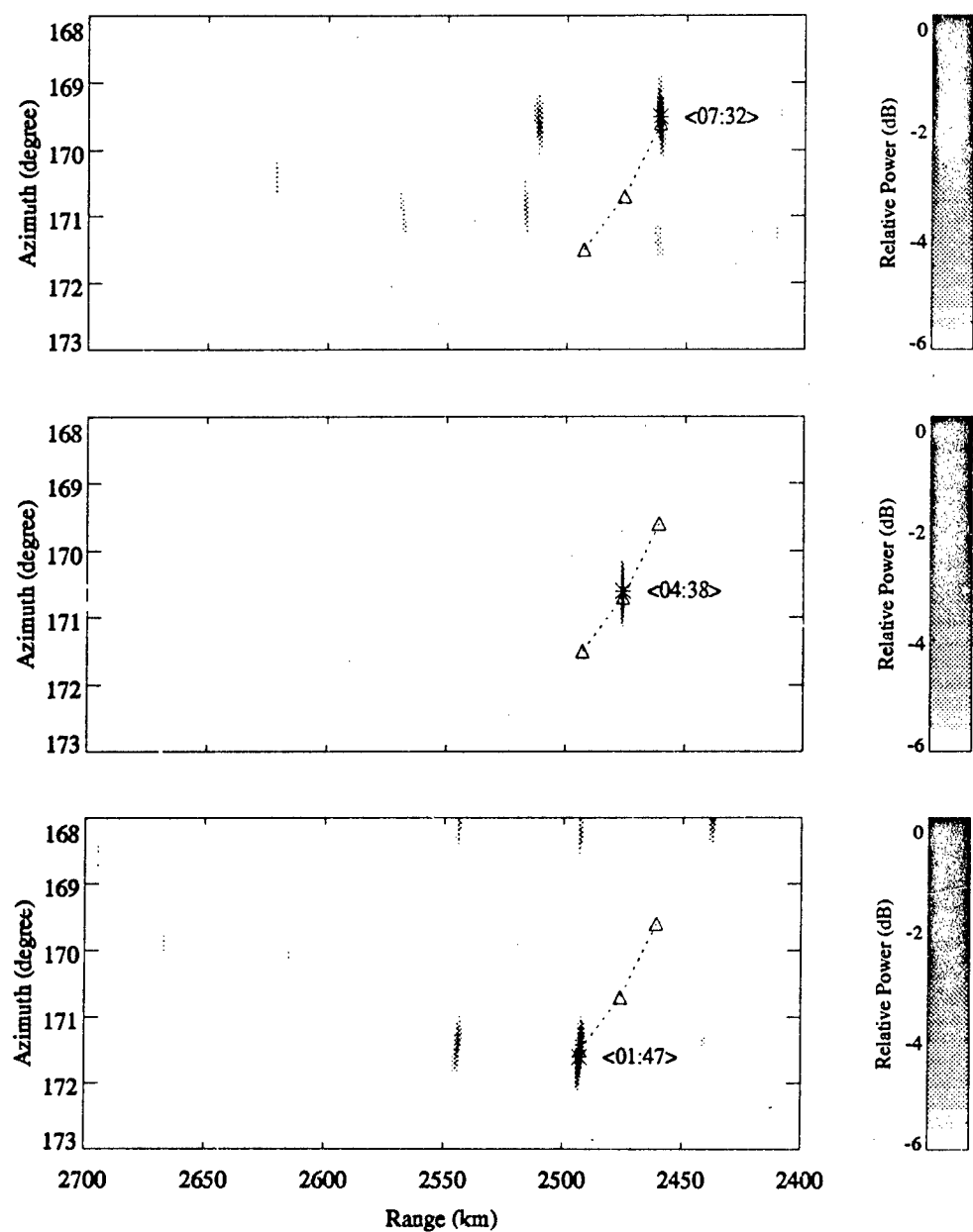
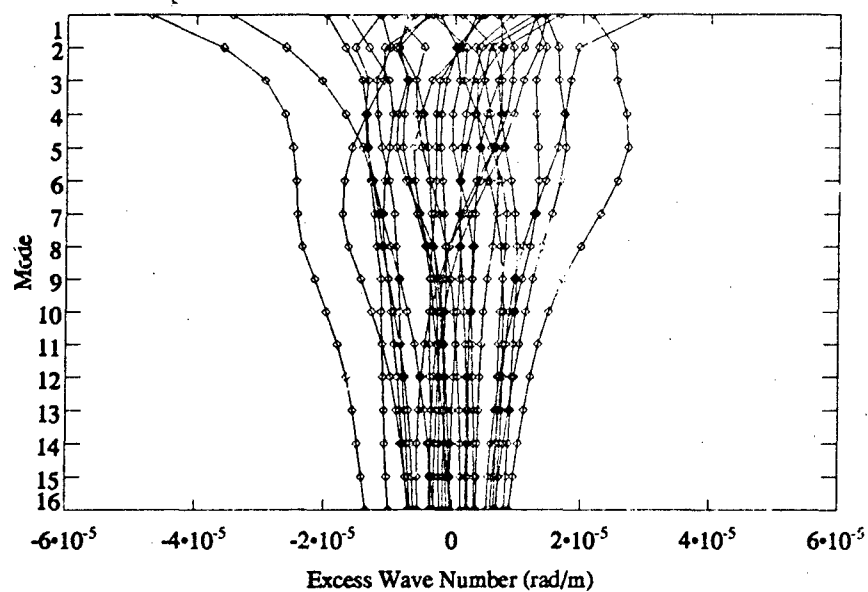
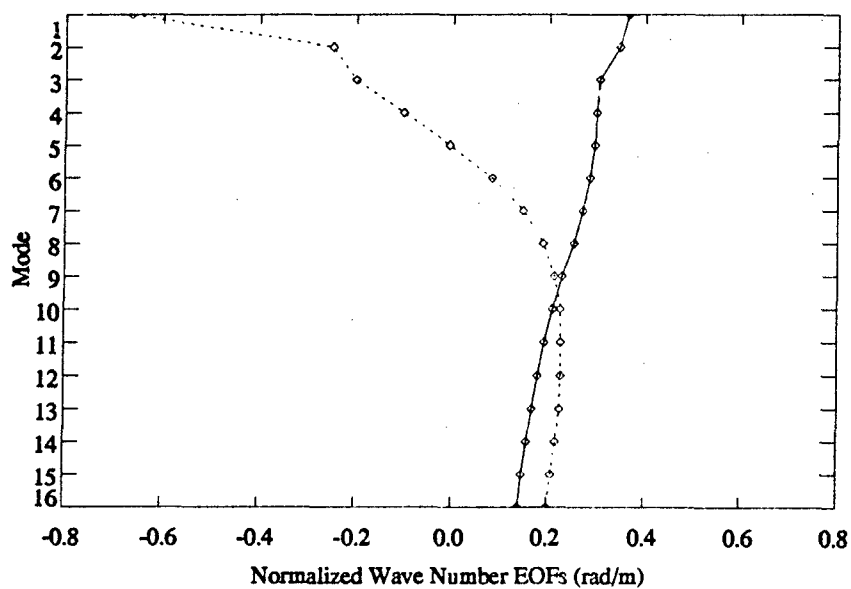


**Figure 5.9** Self-cohered source locations by environment adaptation technique using sound speed EOF coefficients as search parameters.



(a)



(b)

**Figure 5.10** (a) Excess (demeaned) horizontal wave numbers at 14 Hz derived from 30 AXBT measurements made between 140° W and 150° W, July 1989, (b) Normalized versions of the first and second EOFs derived from (a).

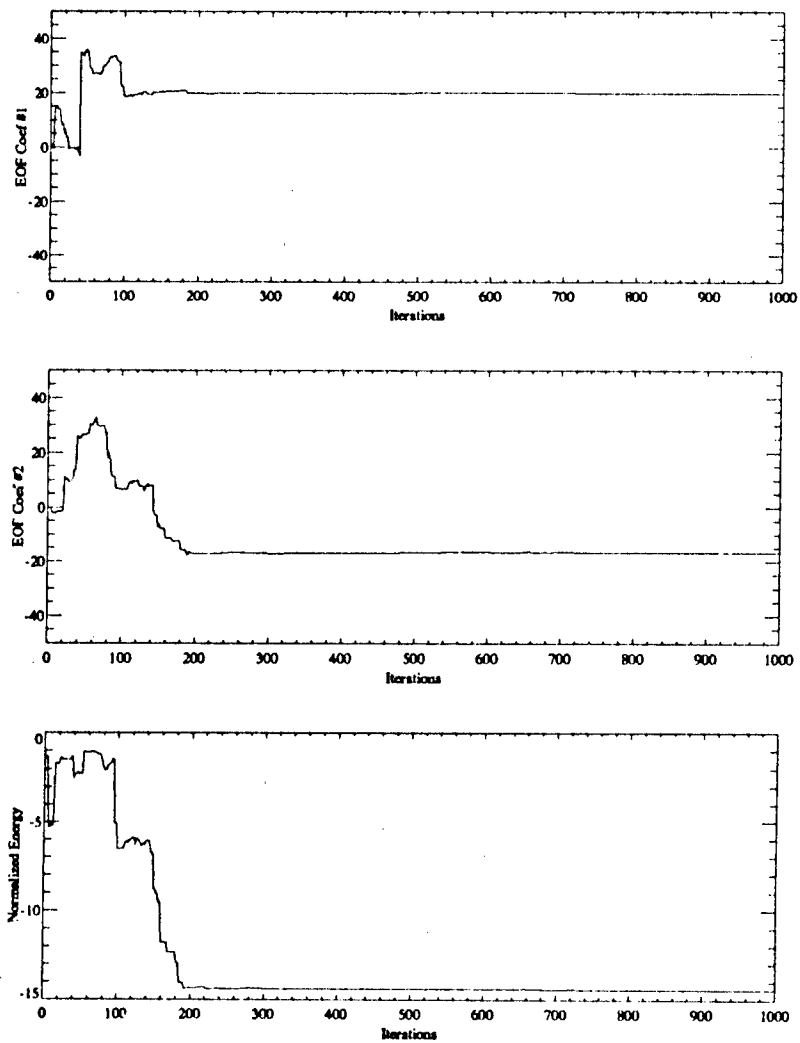


**Figure 5.11** Trajectories of the wave number EOF coefficients and cost function learning curve for a typical annealing run (simulation).

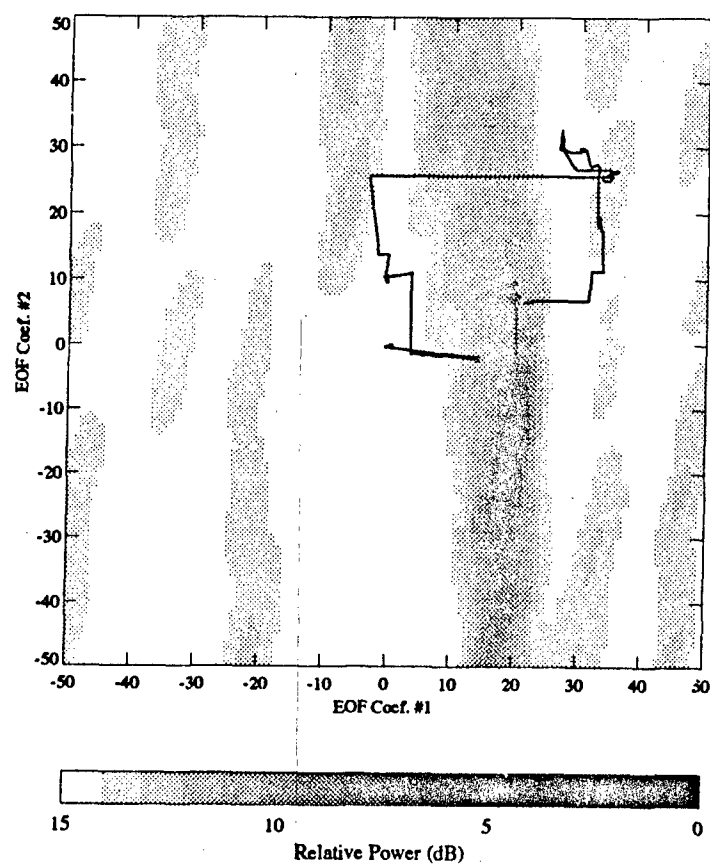


**Figure 5.12** Energy surface as a function of wave number EOF coefficients computed by exhaustive search (simulation).



cients as the annealing proceeds. Figure 5.13 presents the trajectories for the nine runs while Table 5.4 lists the optimal wave number EOF coefficients. Again, good convergence properties and

**Table 5.4** Optimization results from nine runs using wave number EOF coefficients as search parameters.

Run	EOF Coef. #1	EOF Coef. #2
1	20.05	-16.66
2	19.99	-16.85
3	19.98	-16.85
4	19.93	-16.83
5	20.07	-16.60
6	20.01	-16.72
7	19.95	-16.85
8	20.00	-16.83
9	20.02	-16.77

agreement among the wave number EOF coefficient estimates are observed. Using as a reference the averaged model wave numbers derived from the measured profiles, the "true" minus the measured and the adapted minus the measured are plotted by solid and dotted lines, respectively, in Figure 5.14. The adapted wave numbers track the "true" wave numbers nicely except for the first five modes. A possible explanation of the deviation from the "true" wave numbers is that these modes are weakly excited, thus less weight is given during the adaptation process. Figure 5.15 shows the range-azimuth ambiguity surface for all three time intervals using the adapted wave numbers. The optimized (or self-cohered source) locations match those of ideal simulation. It is of interest to know whether the true source location is unique in the neighborhood of the source location. The adaptation procedure is then repeated for each assumed source location within a spatial window extended 16 km in range and 1.5 degrees in azimuth (approximately 60 km in cross range) enclosing the true source location. Figure 5.16 confirms that the range-azimuth maximum energy surface indeed has a maximum that corresponds to the true source location. This suggests that a weakly range-dependent environment can be approximated by a range-independent environment in a matched-field sense, given that the sensor-array geometry is known exactly.

#### 5.4.1.3 Remarks

Although both implementations of the environment adaptation technique produce similar results under the example given above, the computation burden for the two approaches differs significantly. For the sound speed case, evaluation of the cost function requires the invocation of the acoustic propagation model to output the modal eigen-functions and wave numbers (this is com-

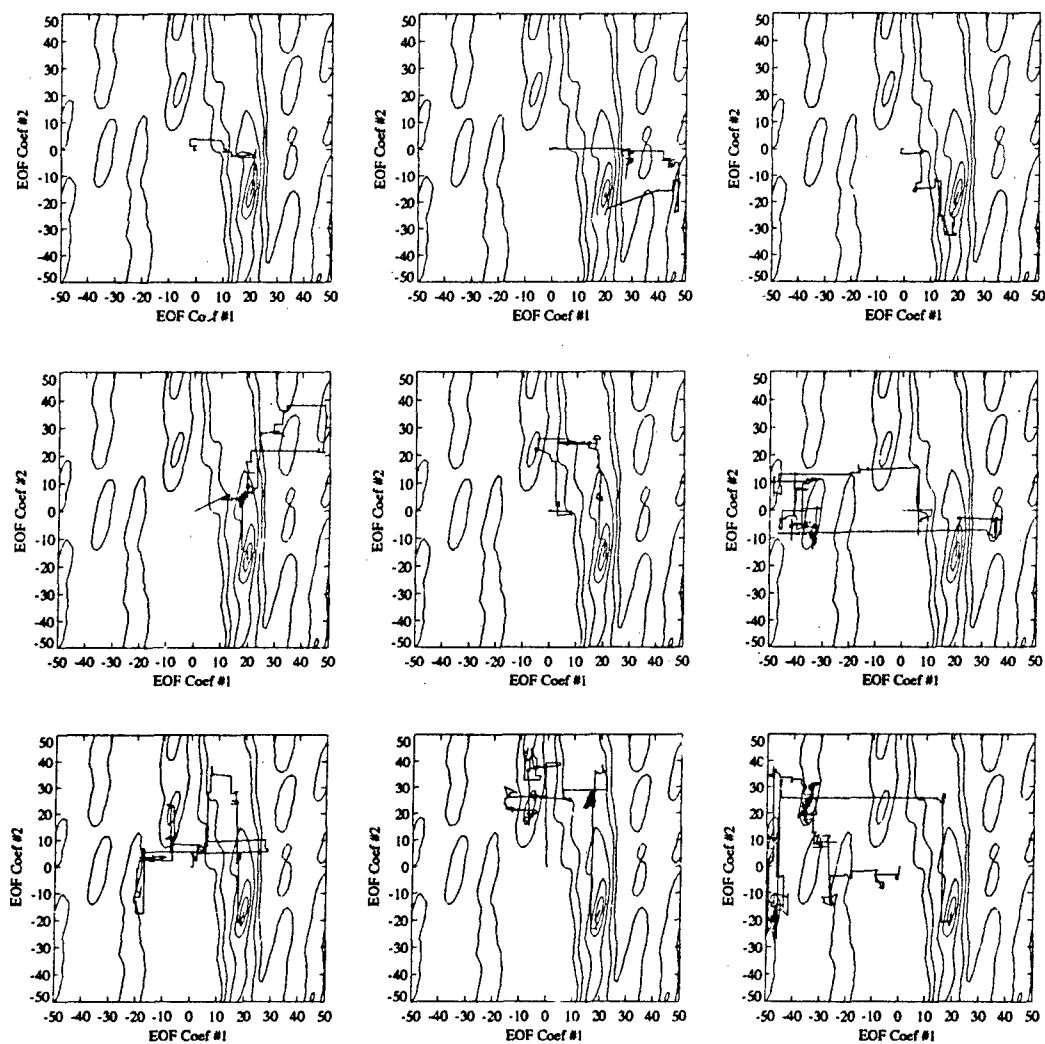


**Figure 5.13** Joint trajectories of the wave number EOF coefficients for different annealing runs.

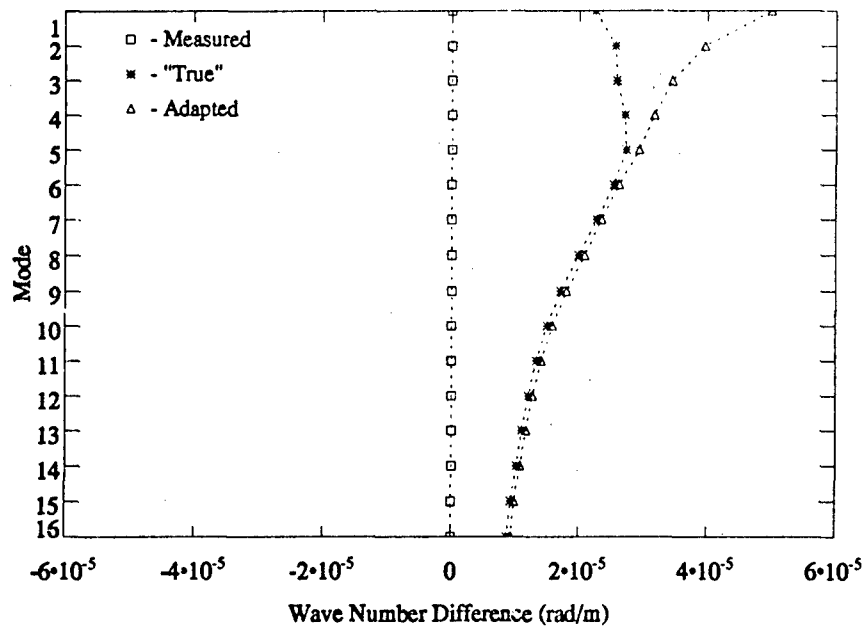


**Figure 5.14** Deviations in adapted wave numbers and "true" wave numbers from the measured model wave numbers (simulation).

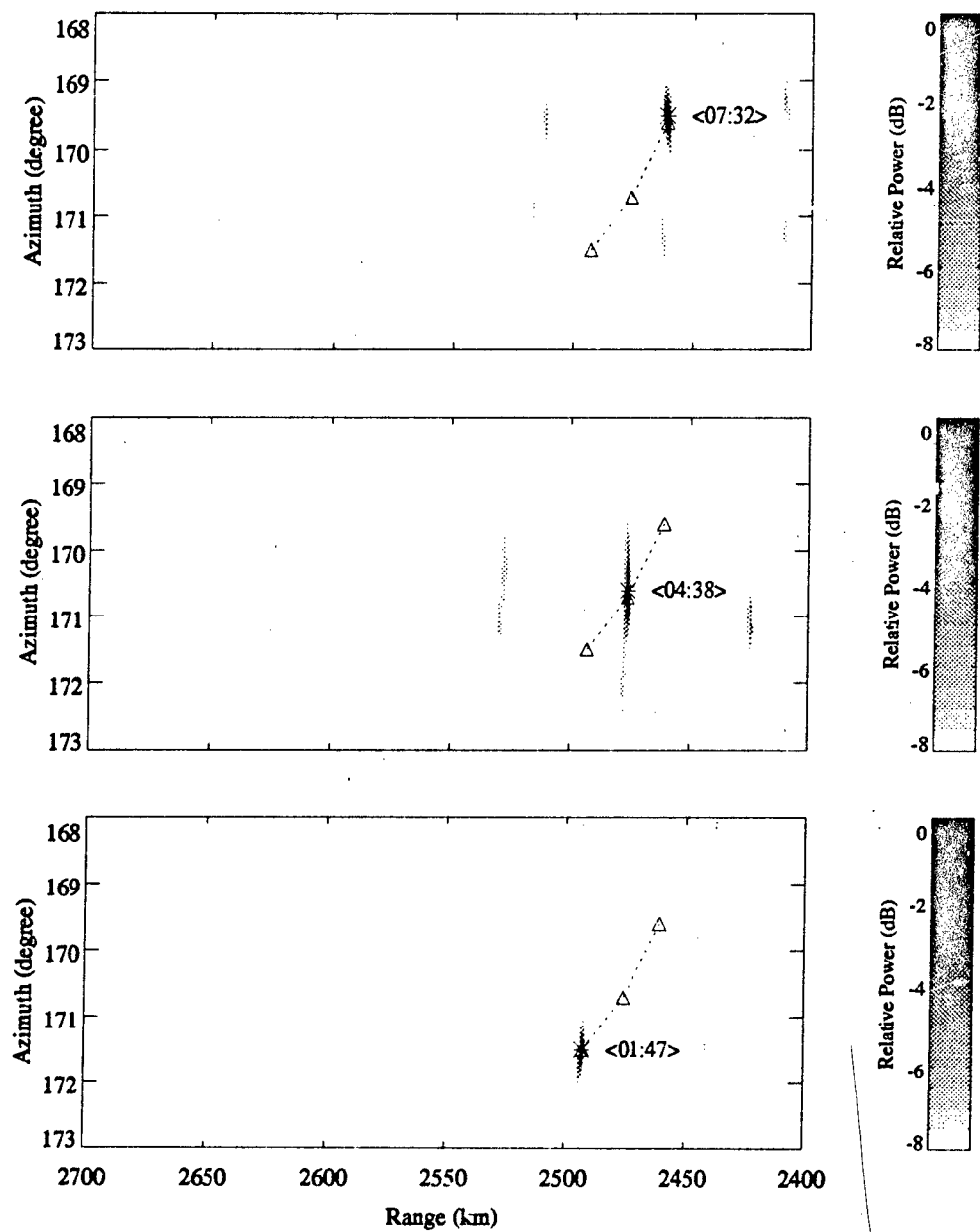


**Figure 5.15** Self-cohered source locations by environment adaptation technique using wave number EOF coefficients as search parameters (simulation).

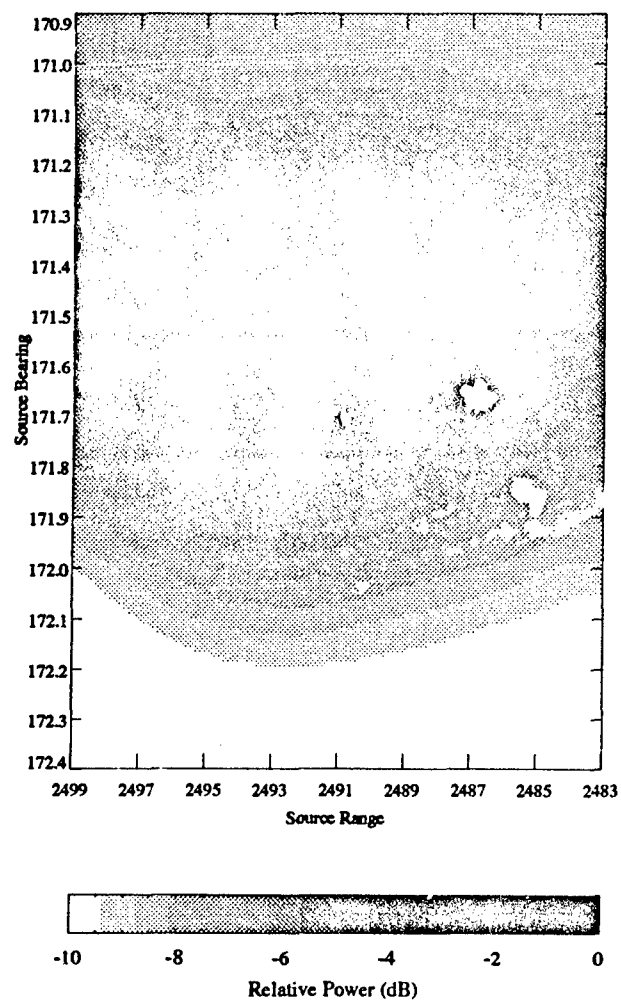


**Figure 5.16** Range-azimuth energy surface derived from repeating the optimization procedure for each range-azimuth cell (simulation).

putation intensive). In the wave number adaptation case, the wave numbers are readily available, and updating the wave numbers according to the perturbations involves only a few trivial algebraic steps. Thus, the difference in computation performance for the two implementations is at least on the order of a few magnitudes.

#### 5.4.2 Experimental Data

Data collected by the Swallow float array during the July 1989 experiment in the Northeast Pacific were then processed in the same fashion as the simulated data. The acoustic modeling was the same as in the simulation. The data considered here were recorded at 01:47, 04:38, and 07:32 PST July 9, 1989. A 2048-point data block for each time interval was extracted to estimate the array cross-spectral density matrix. Each time interval was 41 seconds long. Data were processed with 128-point fast Fourier transforms with 50 percent overlap. Thirty-one snapshots were obtained to estimate the array cross-spectral density matrix. Figure 5.17 plots the matched-field range-azimuth ambiguity surfaces for all three intervals with the highest peak marked with \*'s and the true source locations marked with  $\Delta$ 's. The shift in the source locations was due to the environmental mismatch as diagnosed through simulation in the last section. We then entered into the adaptation phase of the technique. We cautiously selected the reference source location that corresponded to 01:47 PST July 9, 1989, by repeating the adaptation procedure for all assumed range-azimuth cells in the neighborhood of the source location gotten from the source log. The wave number EOF coefficients were used as the search parameters for computational efficiency. Figure 5.18 shows the range-azimuth maximum energy surface. The highest peak in the surface (a range of 2489 km and an azimuth  $172.1^\circ$ ) was used as the reference location.

##### 5.4.2.1 Sound Speed Adaptation

First, the sound speed EOF coefficients were used as the search parameters. Figure 5.19 shows the trajectories of the sound speed EOF coefficients during an annealing run with the energy surface by grid search as the background. Figure 5.20 plots the adapted sound speed profile derived from the optimal EOF coefficients. The extensive excursion of the adapted profile between 100 to 200 meters suggests that the second EOF coefficient plays a major role in forming the underlying environment. Examining the energy surface confirms such conjecture, i.e., the surface peaks at around  $(-6, 29)$ . The adapted sound speed profile was then used to replace the measured sound speed profiles between  $140^\circ$  W and  $150^\circ$  W. We then proceeded to the localization phase of the adaptation technique. Figure 5.21 shows the optimized range-azimuth ambiguity surface for all three time intervals. As can be seen, the optimized or self-cohered source track mimics the track derived from the source log. The minor discrepancy, a  $0.6^\circ$  shift between the true and estimated source locations, is thought to be due to the slight uncertainty in selecting the coordinate system with respect to true north for the float localization (refer to Figure 3.14), since the orientation of the X axis of the coordinate system was taken to be the ship's position when bottomed floats 9 and

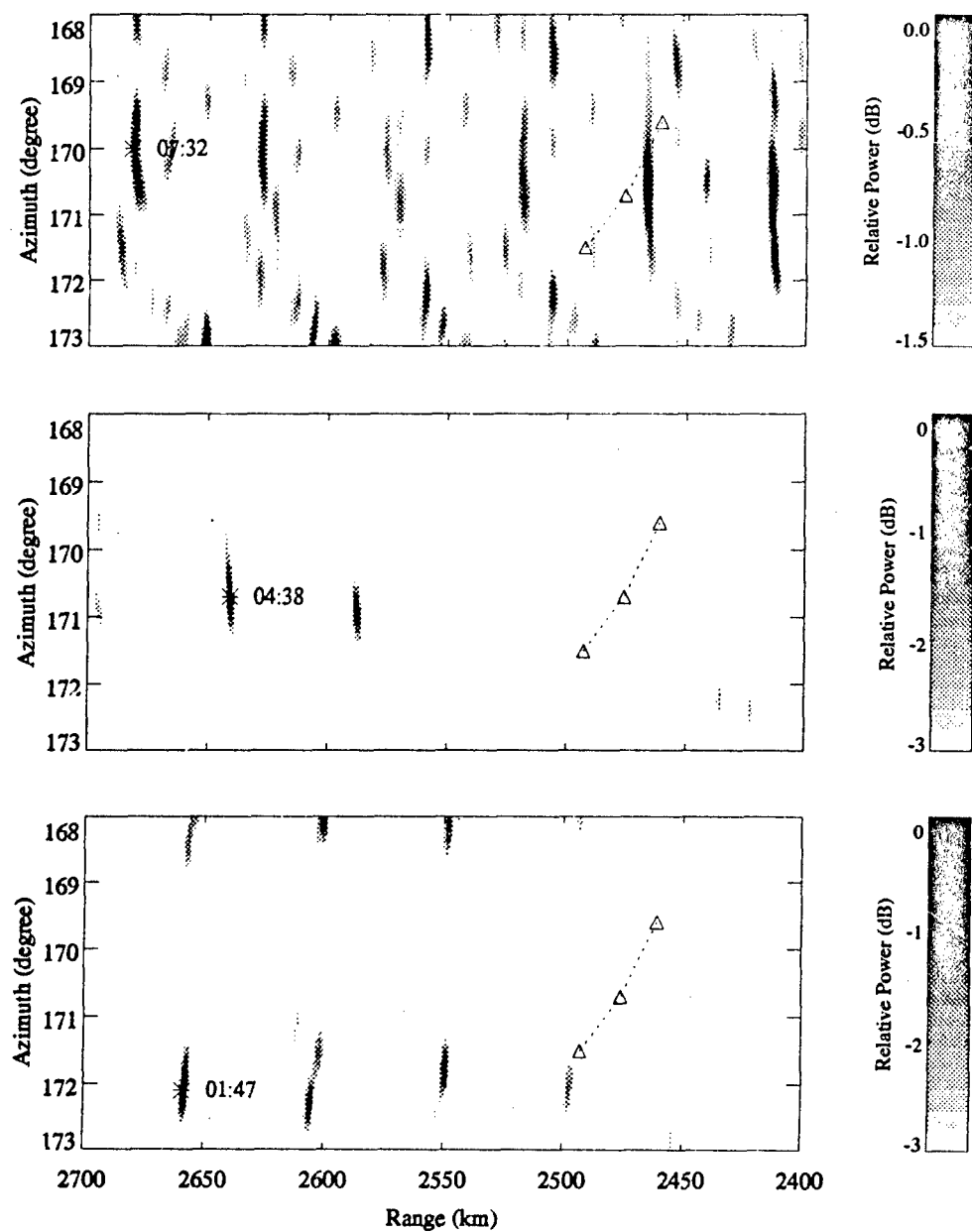
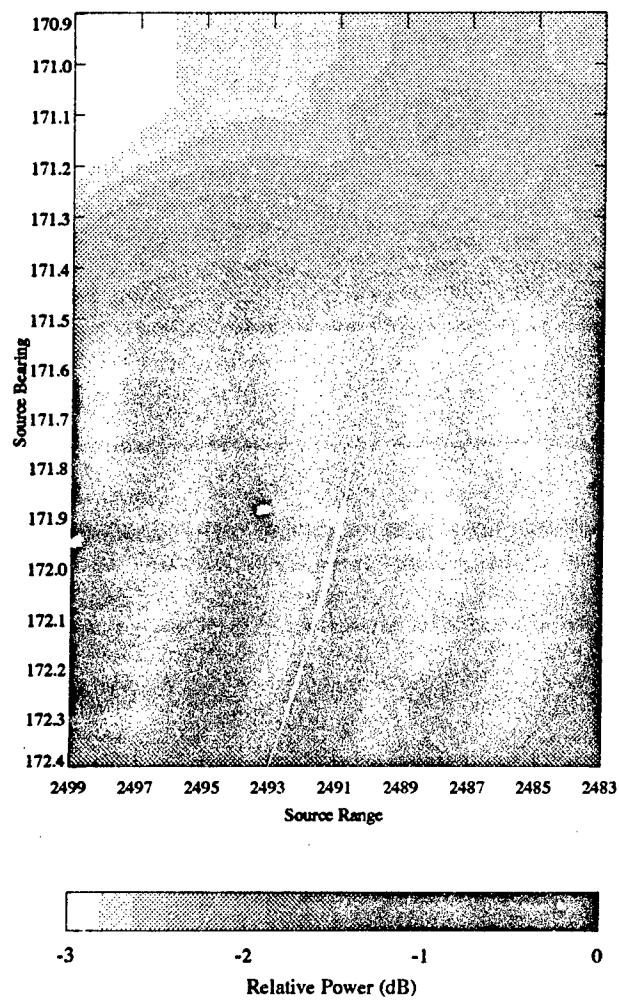
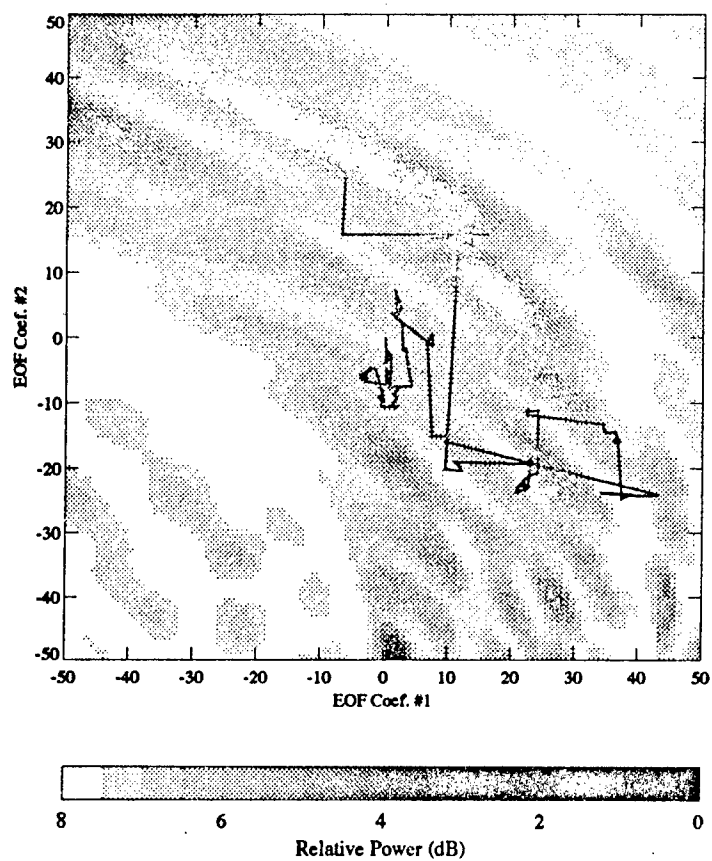


Figure 5.17 Matched-field processing of experimental data during the three time intervals.



**Figure 5.18** Range-azimuth energy surface derived from repeating the optimization procedure for each range-azimuth cell using data collected at 01:47 PST, July 1989.





**Figure 5.19** Energy surface as a function of sound speed EOF coefficients computed by exhaustive search corresponds to source location during 01:47 PST, July 1989.

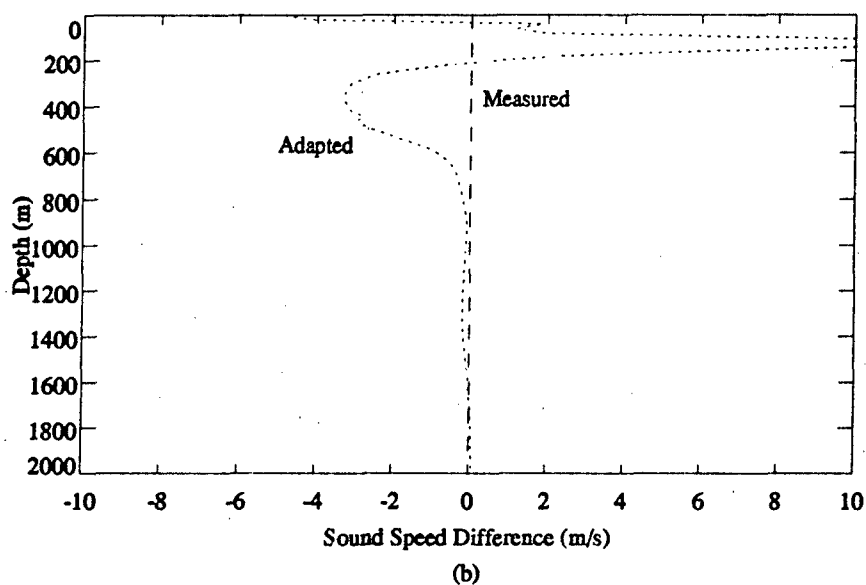
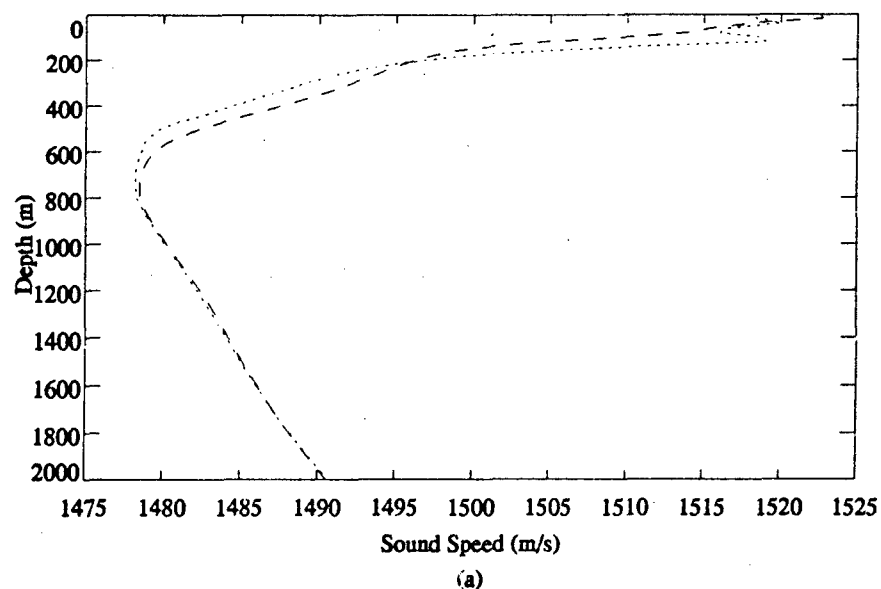


**Figure 5.20** (a) Sound speed profile (dotted line) computed from the optimal EOF coefficients obtained from Figure 5.19 and the averaged model sound speed profile (dashed line). (b) The difference version of (a) i.e., using the measured profile as reference (dashed line), the adapted minus the measured is plotted in dotted line.

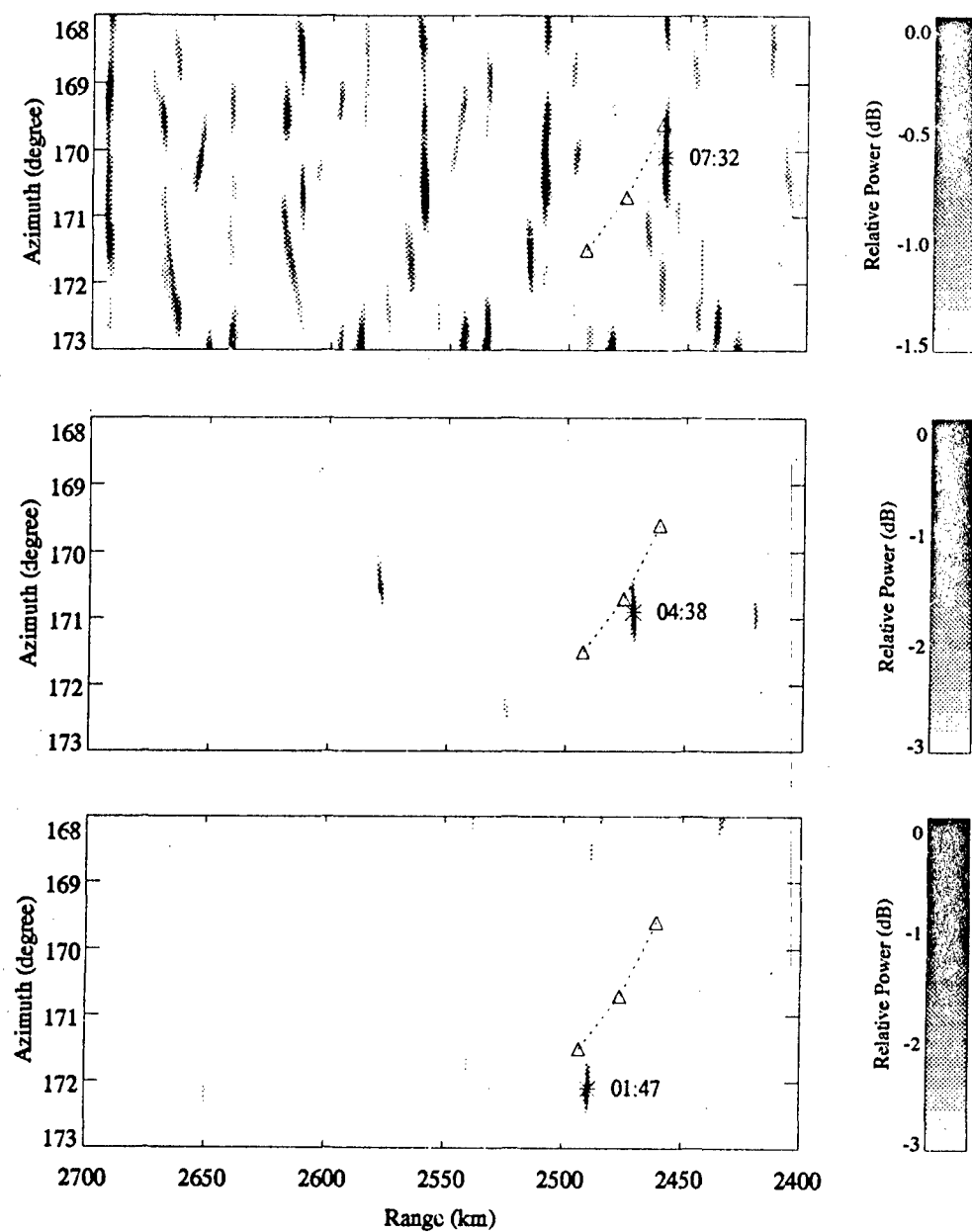


**Figure 5.21** Self-cohered source locations by environmental adaptation technique using sound speed EOF coefficients as the search parameters.

10 were put into the water. A relative motion of approximating 60 m in the Y direction between floats 9 and 10 while the floats descended to the bottom would cause the  $0.6^\circ$  rotation in the MFP results. This order of error between ship position and true float position on the bottom has been noted in other Swallow float experiments.

#### 5.4.2.2 Wave Number Adaptation

We next used the wave number EOF coefficients as the search parameters. Figure 5.22 shows the trajectories of the wave number EOF coefficients, corresponding to the annealing run that produced the highest peak in Figure 5.18. The energy surface is plotted as the background. Figure 5.23 plots the first 16 modal wave numbers (derived from the wave number EOF coefficients) with respect to the measured wave numbers. The adapted modal wave numbers were used to replace the measured modal wave numbers between  $140^\circ$  W and  $150^\circ$  W. We then proceeded to the localization phase of the adaptation technique. Figure 5.24 shows the optimized range-azimuth ambiguity surface for all three time intervals for the wave number adaptation approach. The optimized (self-cohered) source locations match those of the sound speed approach except that the source location during the third interval, i.e., 07:32, is missed by one CZ. The range estimate error found during the third time interval is thought to be due to the fact that the wave number adaptation approach adapts the wave numbers only and is not robust enough to accommodate large variations in the modal depth eigenfunctions at the source, i.e., the assumed modal eigenfunctions at the source differ significantly from the true underlying modal eigenfunctions at the source.

### 5.5 Summary

The major difficulty with MFP is the environmental mismatch problem. In this chapter, two techniques to deal with this problem were reviewed. An approach to the environmental mismatch problem was presented. The key idea of this approach was the adaptation of the replica pressure fields to the acoustic data received by the sensor array so that the environmental parameters along the path between a reference source and the sensor array can be inverted assuming the source-array geometry is known exactly. Using the inverted (or adapted) environmental parameters, normal MFP can be resumed to search for an unknown source of interest. An efficient optimization algorithm was implemented using the EOF approach to compress the search spaces and a fast annealing algorithm to search the optimal environmental parameter values. Two implementations of the environmental adaptation technique were first studied through simulation and then applied to experimental data. Both simulation and real data processing results demonstrated the potential of this technique. The self-cohered 14-Hz source locations for a period of 6 hours during the July 1989 experiment were found to be consistent with the source locations obtained from the source log. The sound speed structure adaptation implementation of the technique seemed to be robust but computation cumbersome. However, the modal wave number adaptation implementation was

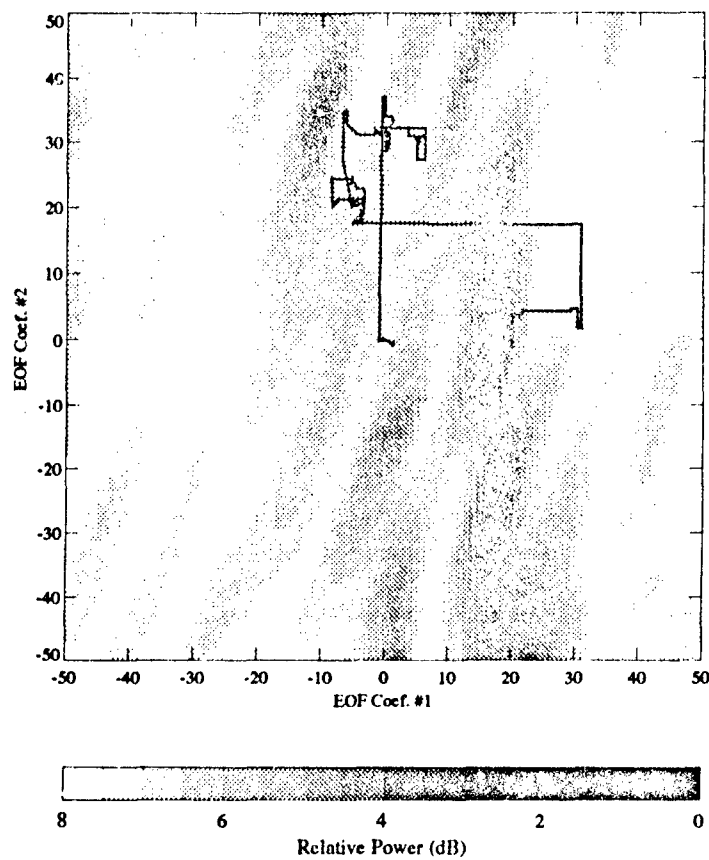


**Figure 5.22** Energy surface as a function of wave number EOF coefficients computed by exhaustive search corresponds to source location during 01:47 PST, July 1989.

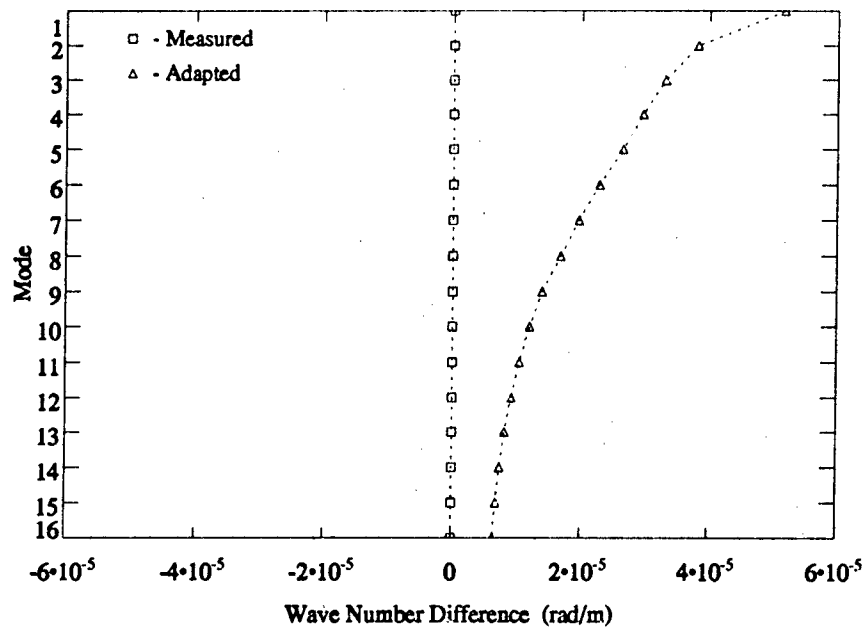
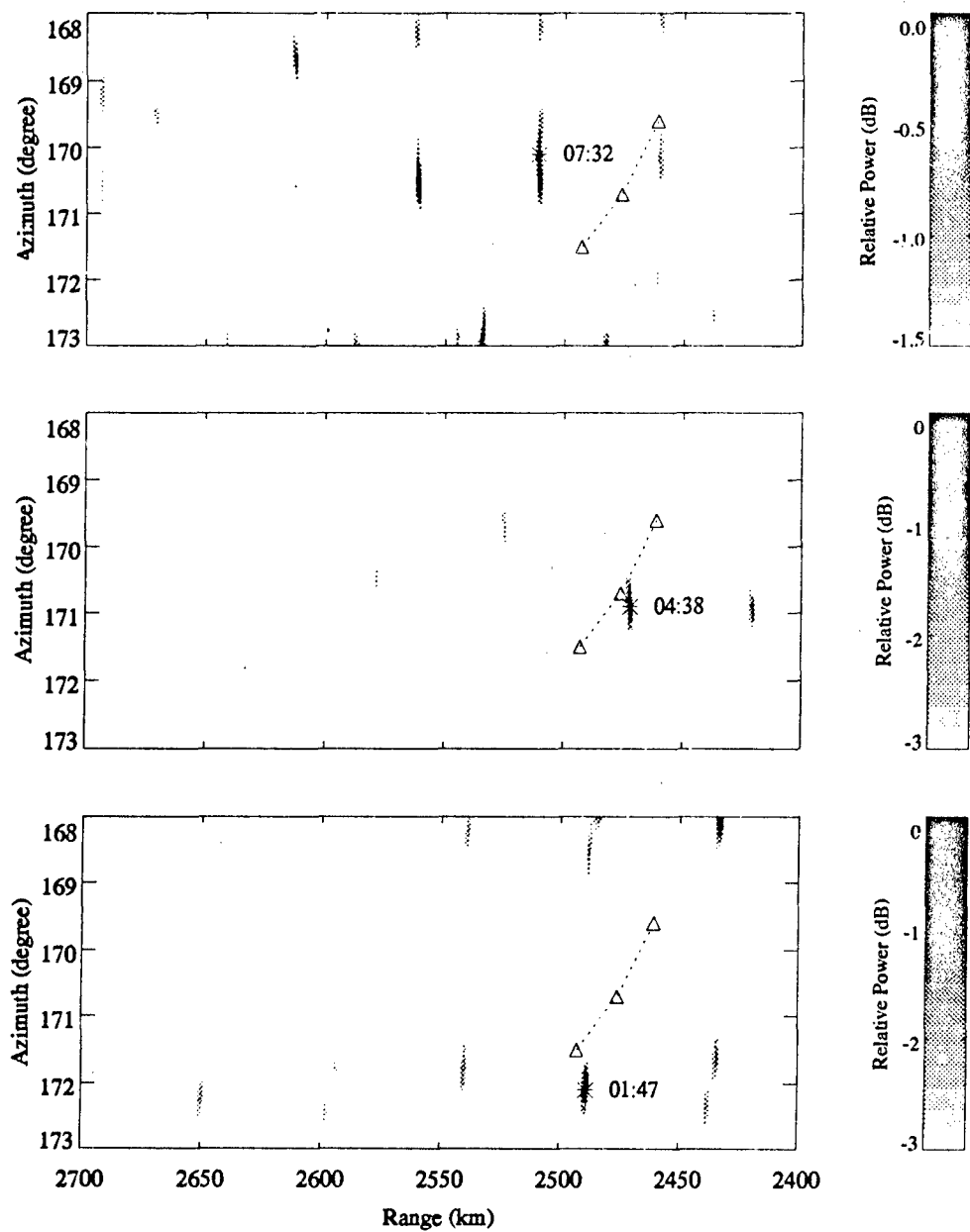


Figure 5.23 Adapted wave numbers compared to measured model wave numbers.



**Figure 5.24** Self-cohered source locations by environmental adaptation technique using wave number EOF coefficients as the search parameters.

computationally efficient but sensitive to separation between the reference and the unknown source locations in time and space.



## CONCLUSIONS

The central theme of this dissertation has been the underwater source localization problem. Specifically, we have demonstrated the source localization and tracking capability of a freely drifting volumetric array with MFP using experimental data. We have also proposed and demonstrated an environment adaptation technique to deal with the environmental mismatch problem.

Data collected during the 1989 Swallow float experiment were used to perform the study. The geometries of the Swallow float array as a function of time during the 1989 experiment have been estimated using the 8-kHz range measurement with both least-squares and Kalman filter methods. The rms position errors estimated by both methods are within 5 meters, which is within the desired accuracy of one-tenth of a wavelength at the highest frequency of interest 25 Hz (6 m) in order to effectively process the VLF acoustic data coherently. Furthermore, analysis of the experiment acoustic data showed high signal-to-noise ratio and high coherence at 14 Hz among all nine freely drifting floats during some time intervals. The 14-Hz was a continuous wave tonal projected by the Mark VI from the R/V Aloha involving in a companion experiment. The high coherence among the floats provided an opportunity for matched-field beamforming of the VLF acoustic data.

The replica vectors were modeled with an adiabatic normal mode numerical technique using the environmental data collected during the experiment. Initial matched-field processing of the experimental data experienced difficulties in estimating the source depth and range while the source azimuth estimate was somewhat successful. Controlled simulation using the same conditions as in the real data has revealed that (1) depth resolution indeed is a difficult problem for a shallow VLF source in a long-range environment due to fewer modes being available and due to low source depth-to-wavelength ratio, (2) the range estimate is sensitive to environmental mismatch, and (3) the azimuth estimate is robust. The main cause of the performance degradation has thus been identified to be uncertainty in the environment (i.e., sound speed mismatch).

An environment adaptation technique using a global optimization algorithm was developed to counteract the MFP performance degradation due to uncertainty in the ocean acoustic environment. We have demonstrated through simulation that with limited *a priori* knowledge of the environment and with a reference source at a known location, the environment can be adapted in a matched-field sense. Using the adapted environment, other unknown source(s) of interest in the vicinity of the reference source can be correctly localized. Applying the environment adaptation technique to experimental data has shown that the 14-Hz source was successfully localized and tracked in azimuth and range within a region of interest using the MFP technique for a period of 6 hours.

There are several directions in which the results developed here can be extended. In this dissertation, due to the nature of the data set, emphasis was placed on localizing underwater sound source at long range. It would be of interest to further test the localization performance of the Swallow float array and the environment adaptation concept in intermediate and close-range situations using experimental data. Also, we need to quantify the performance limitations of the environment adaptation technique through extensive simulation.

This thesis has been restricted to using the acoustic pressure data from the hydrophones. Since acoustic particle velocity data from three channels of the geophones are also available, it would be of interest to process the particle-velocity data in a matched-field sense and compare the results to those of acoustic-pressure data.

Finally, although the environment adaptation technique did perform well, efforts should also be directed toward investigating a more robust array processing technique, i.e., developing an MFP processor that is tolerant to some degrees of mismatch between replica and data and that still maintains a satisfactory localization performance.

## APPENDICES

### A: Harmonic Mean Sound Speed Estimates

Floats	Sound Speed (m/msec)	Error Variance ( (m/msec) <sup>2</sup> )
9 & 10	1.5237	$0.1 \times 10^{-6}$
9 & 11	1.5237	$0.1 \times 10^{-6}$
9 & 0	1.4975	$0.1 \times 10^{-6}$
9 & 1	1.4999	$0.1 \times 10^{-6}$
9 & 2	1.5024	$0.1 \times 10^{-6}$
9 & 3	1.5043	$0.1 \times 10^{-6}$
9 & 4	1.5075	$0.1 \times 10^{-6}$
9 & 5	1.5108	$0.1 \times 10^{-6}$
9 & 6	1.5143	$0.1 \times 10^{-6}$
9 & 7	1.5178	$0.1 \times 10^{-6}$
9 & 8	1.5213	$0.1 \times 10^{-6}$
10 & 11	1.5237	$0.1 \times 10^{-6}$
10 & 0	1.4975	$0.1 \times 10^{-6}$
10 & 1	1.4999	$0.1 \times 10^{-6}$
10 & 2	1.5024	$0.1 \times 10^{-6}$
10 & 3	1.5043	$0.1 \times 10^{-6}$
10 & 4	1.5075	$0.1 \times 10^{-6}$
10 & 5	1.5108	$0.1 \times 10^{-6}$
10 & 6	1.5143	$0.1 \times 10^{-6}$
10 & 7	1.5178	$0.1 \times 10^{-6}$
10 & 8	1.5213	$0.1 \times 10^{-6}$
11 & 0	1.4975	$0.1 \times 10^{-6}$
11 & 1	1.4999	$0.1 \times 10^{-6}$
11 & 2	1.5024	$0.1 \times 10^{-6}$
11 & 3	1.5043	$0.1 \times 10^{-6}$
11 & 4	1.5075	$0.1 \times 10^{-6}$
11 & 5	1.5108	$0.1 \times 10^{-6}$
11 & 6	1.5143	$0.1 \times 10^{-6}$
11 & 7	1.5178	$0.1 \times 10^{-6}$
11 & 8	1.5213	$0.1 \times 10^{-6}$
0 & 1	1.4809	$0.1 \times 10^{-6}$
0 & 2	1.4820	$0.1 \times 10^{-6}$
0 & 3	1.4830	$0.1 \times 10^{-6}$
0 & 4	1.4849	$0.1 \times 10^{-6}$
0 & 5	1.4872	$0.1 \times 10^{-6}$
0 & 6	1.4897	$0.1 \times 10^{-6}$
0 & 7	1.4926	$0.1 \times 10^{-6}$

Floats	Sound Speed (m/msec)	Error Variance ( (m/msec) <sup>2</sup> )
0 & 8	1.4955	$0.1 \times 10^{-6}$
1 & 2	1.4832	$0.1 \times 10^{-6}$
1 & 3	1.4844	$0.1 \times 10^{-6}$
1 & 4	1.4865	$0.1 \times 10^{-6}$
1 & 5	1.4890	$0.1 \times 10^{-6}$
1 & 6	1.4917	$0.1 \times 10^{-6}$
1 & 7	1.4948	$0.1 \times 10^{-6}$
1 & 8	1.4978	$0.1 \times 10^{-6}$
2 & 3	1.4860	$0.1 \times 10^{-6}$
2 & 4	1.4883	$0.1 \times 10^{-6}$
2 & 5	1.4909	$0.1 \times 10^{-6}$
2 & 6	1.4939	$0.1 \times 10^{-6}$
2 & 7	1.4970	$0.1 \times 10^{-6}$
2 & 8	1.5002	$0.1 \times 10^{-6}$
3 & 4	1.4898	$0.1 \times 10^{-6}$
3 & 5	1.4926	$0.1 \times 10^{-6}$
3 & 6	1.4957	$0.1 \times 10^{-6}$
3 & 7	1.4989	$0.1 \times 10^{-6}$
3 & 8	1.5022	$0.1 \times 10^{-6}$
4 & 5	1.4954	$0.1 \times 10^{-6}$
4 & 6	1.4986	$0.1 \times 10^{-6}$
4 & 7	1.5020	$0.1 \times 10^{-6}$
4 & 8	1.5053	$0.1 \times 10^{-6}$
5 & 6	1.5018	$0.1 \times 10^{-6}$
5 & 7	1.5052	$0.1 \times 10^{-6}$
5 & 8	1.5086	$0.1 \times 10^{-6}$
6 & 7	1.5086	$0.1 \times 10^{-6}$
6 & 8	1.5120	$0.1 \times 10^{-6}$
7 & 8	1.5155	$0.1 \times 10^{-6}$
9 & 9	0.7478	$0.1 \times 10^{-6}$
10 & 10	0.7478	$0.1 \times 10^{-6}$
11 & 11	0.7478	$0.1 \times 10^{-6}$
0 & 0	0.7423	$0.1 \times 10^{-6}$
1 & 1	0.7415	$0.1 \times 10^{-6}$
2 & 2	0.7415	$0.1 \times 10^{-6}$
3 & 3	0.7418	$0.1 \times 10^{-6}$
4 & 4	0.7424	$0.1 \times 10^{-6}$
5 & 5	0.7433	$0.1 \times 10^{-6}$
6 & 6	0.7443	$0.1 \times 10^{-6}$
7 & 7	0.7456	$0.1 \times 10^{-6}$
8 & 8	0.7469	$0.1 \times 10^{-6}$

## B: Reciprocal Path Travel Time Variances

Floats	Variance (msec <sup>2</sup> )
9 & 0	2.5637
9 & 1	0.8505
9 & 2	1.0208
9 & 3	1.9094
9 & 4	0.6386
9 & 5	0.1996
9 & 6	0.3951
9 & 7	0.8572
9 & 8	0.6349
10 & 0	0.9729
10 & 1	0.8914
10 & 2	0.7811
10 & 3	0.9248
10 & 4	0.5736
10 & 5	0.2852
10 & 6	1.7845
10 & 7	0.7622
10 & 8	0.8752
11 & 0	1.5452
11 & 1	1.4314
11 & 2	0.8876
11 & 3	1.6525
11 & 4	0.5814
11 & 5	0.2615
11 & 6	1.1790
11 & 7	0.8512
11 & 8	0.3782
0 & 1	1.2800
0 & 2	1.8693
0 & 3	2.1737
0 & 4	3.8525
0 & 5	1.0472
0 & 6	2.5033
0 & 7	1.9553
0 & 8	2.0692
1 & 2	1.4894
1 & 3	2.7448
1 & 4	2.1325
1 & 5	0.4147

Floats	Variance (msec <sup>2</sup> )
1 & 6	2.4348
1 & 7	1.5548
1 & 8	1.0353
2 & 3	0.9688
2 & 4	0.8213
2 & 5	1.5815
2 & 6	1.4629
2 & 7	1.3690
2 & 8	1.5648
3 & 4	0.3759
3 & 5	0.7077
3 & 6	2.2006
3 & 7	0.8939
3 & 8	2.3961
4 & 5	0.4745
4 & 6	0.3362
4 & 7	1.1722
4 & 8	2.3950
5 & 6	0.4461
5 & 7	0.5171
5 & 8	0.2398
6 & 7	0.9575
6 & 8	0.7759
7 & 8	0.8713

**C: Coefficients of Second-Order Fits to the Reciprocal Path Measurement Differences**

Float	Float	Curvature (msec/(100 records) <sup>2</sup> )	Slope (msec/ 100 records)	Intercept (msec)
9	10	0.01518	-2.50139	-44.85477
9	11	0	54.54246	-70.34302
9	0	-0.00399	25.55177	-143.75967
9	1	-0.02566	36.63271	-180.84509
9	2	0.10133	-0.61512	-120.54930
9	3	0.07983	42.33369	-39.60468
9	4	0.07021	34.60133	4.20795
9	5	0.10593	24.74624	-73.47556
9	6	0.00936	10.18588	-74.90748
9	7	-0.00872	-9.31168	-56.46815
9	8	-0.05318	21.87121	-23.24966
10	11	-0.04577	58.26873	-36.45166
10	0	0	27.24289	-89.77655
10	1	0.00429	38.10869	-131.25516
10	2	0.01703	3.83972	-86.58073
10	3	0.04859	45.28195	3.27728
10	4	0	38.47172	40.12939
10	5	0	29.46763	-41.03638
10	6	-0.04374	13.62054	-33.69858
10	7	0	-7.32420	-10.27667
10	8	0.00109	22.64396	30.63046
11	0	0	-29.19710	-73.01617
11	1	0.05370	-19.95675	-101.24307
11	2	0.05198	-53.80684	-58.25610
11	3	0.09517	-12.82133	35.28806
11	4	0.04854	-19.51229	69.53906
11	5	0.18019	-31.36666	-0.52029
11	6	0.01447	-44.42154	-6.89490
11	7	0.02574	-64.76017	16.32593
11	8	0.01572	-35.06775	64.42834
0	1	0.02894	9.89287	-32.20901
0	2	0.02596	-23.89109	8.72311
0	3	0.01238	18.85915	91.22421
0	4	0.04712	10.02173	139.38211
0	5	0.08044	0.14604	60.69196
0	6	-0.04036	-13.76737	57.26703
0	7	0.01477	-35.07599	84.37808

Float	Float	Curvature (msec/(100 records) <sup>2</sup> )	Slope (msec/ 100 records)	Intercept (msec)
0	8	0.00207	-4.94819	126.70593
1	2	0.02212	-34.60089	47.02808
1	3	-0.04047	9.60653	118.90907
1	4	-0.02242	1.17007	165.56229
1	5	0.05049	-9.63175	92.00610
1	6	-0.08490	-23.35032	88.31992
1	7	-0.03788	-44.52425	114.87286
1	8	-0.03449	-14.65317	158.19537
2	3	0.01816	41.85386	86.79614
2	4	-0.12803	37.56519	109.27396
2	5	0.02849	24.51210	50.82257
2	6	-0.01694	8.64918	58.06210
2	7	0.00913	-11.82151	79.21877
2	8	-0.09417	20.80200	107.27597
3	4	-0.04826	-6.73761	36.29120
3	5	0.08602	-19.59419	-22.48524
3	6	-0.04837	-32.81397	-32.02466
3	7	-0.06930	-52.08339	-16.81482
3	8	-0.02307	-23.57817	35.45761
4	5	0.07278	-10.60359	-74.41269
4	6	0	-26.25876	-64.93631
4	7	0	-45.90385	-51.37494
4	8	-0.06807	-14.64013	-13.09142
5	6	-0.12665	-13.52716	-5.83221
5	7	-0.05768	-35.12783	20.22412
5	8	-0.05973	-5.68480	69.97832
6	7	0.05221	-21.31087	26.96481
6	8	-0.03280	10.73389	59.33090
7	8	0.07448	27.69873	58.11115



# D: Magnitude-Squared Coherence (Record 1145)

Float	Float	MSC
0	1	0.750720
0	2	0.885170
0	3	0.700810
0	4	0.712970
0	5	0.804030
0	6	0.679740
0	7	0.820220
0	8	0.816530
1	2	0.789920
1	3	0.616370
1	4	0.580990
1	5	0.634840
1	6	0.627240
1	7	0.666920
1	8	0.670200
2	3	0.712980
2	4	0.755040
2	5	0.774810
2	6	0.802950
2	7	0.814410
2	8	0.836930
3	4	0.609960
3	5	0.726390
3	6	0.739470
3	7	0.710770
3	8	0.742590
4	5	0.732270
4	6	0.662420
4	7	0.617800
4	8	0.683280
5	6	0.695380
5	7	0.689330
5	8	0.765470
6	7	0.638040
6	8	0.713870
7	8	0.777410

## REFERENCES

- Baggeroer, A. B., W. A. Kuperman, and H. Schmidt, "Matched-Field Processing: Source Localization in Correlated Noise as an Optimum Parameter Estimation Problem," *J. Acoust. Soc. Am.*, vol. 83, no. 2, pp. 571-587, 1988.
- Bar-Shalom, Y. and T. E. Fortman, *Tracking and Data Association*, Academic Press, Florida, 1988.
- Boyles, A. C., *Acoustic Waveguides, Applications to Oceanic Science*, John Wiley, N.Y., 1984.
- Brekhovskikh, L. and Y. Lysanov, *Fundamentals of Ocean Acoustics*, Springer Verlag, Berlin, 1982.
- Brown, R. G., *Introduction to Random Signal Analysis and Kalman Filtering*, John Wiley & Sons, N.Y., 1983.
- Bucker, H. P., "Use of Calculated Sound Fields and Matched-Field Detection to Locate Sound Sources in Shallow Water," *J. Acoust. Soc. Am.*, vol. 59, no. 2, pp. 368-373, 1976.
- Bucker, H. P., "Self-Coherent Matched-Field Processing," *Fourth Matched-Field Processing Workshop, Defence Research Establishment Pacific*, Victoria, B.C. Canada, September 6-8 1989.
- Burdic, W. S., *Underwater Acoustic System Analysis*, 2nd ed. Prentice-Hall, Englewood Cliffs, N.J., 1991.
- Candy, J. V., *Signal Processing: The Modern Approach*, McGraw-Hill, New York, 1988.
- Capon, J., "High Resolution Frequency-Wavenumber Spectrum Analysis," *Proc. IEEE*, vol. 57, pp. 1408-1418, 1969.
- Carlson, B. D., "Covariance Matrix Estimation Errors and Diagonal Loading in Adaptive Arrays," *IEEE Trans. Aerosp. Electron. Syst.*, vol. 24, no. 4, pp. 397-401, 1988.
- Chen, G. C., G. L. D'Spain, W. S. Hodgkiss, and G. L. Edmonds, "Freely Drifting Swallow Float Array: July 1989 Trip Report," MPL TM-420, Marine Physical Laboratory, Scripps Institution of Oceanography, San Diego, CA, 1990.
- Chen, G. C. and W. S. Hodgkiss, "Localizing Swallow Floats during the July 1989 Experiment," MPL TM-421, Marine Physical Laboratory, Scripps Institution of Oceanography, San Diego, CA, 1990.
- Churgin, J. and S. J. Halminski, "Temperature, Salinity, Oxygen, and Phosphate in Waters off the United States, Eastern North Pacific," National Oceanographic Data Center, 3, 1974.
- Collins, M. D. and W. A. Kuperman, "Focalization: Environmental Focusing and Source Localization," *J. Acoust. Soc. Am.*, vol. 90, no. 3, pp. 1410-1422, September 1991.
- Culver, R. L., "Localizing and beamforming freely-drifting VLF Acoustic Sensors," SIO Reference 88-16, Scripps Institution of Oceanography, San Diego, CA, 1988. Also, Ph.D. dissertation, University of California, San Diego, 1988.

- Culver, R. L. and W. S. Hodgkiss, "Comparison of Kalman and Least Squares Filters for Locating Autonomous Very Low Frequency Acoustic Sensors," *IEEE J. Ocean. Eng.*, vol. OE-13, pp. 282-290, 1988.
- Culver, R. L., G. L. D'Spain, W. S. Hodgkiss, and G. L. Edmonds, "Estimating 8kHz Pulse Travel Times and Travel Times Error from Swallow Float Localization System Measurements," Unpublished Notes, Marine Physical Laboratory, Scripps Institution of Oceanography, San Diego, CA, 1989.
- Culver, R. L. and W. S. Hodgkiss, "Localizing Swallow Floats during the April 1987 Experiment," Unpublished Notes, Marine Physical Laboratory, Scripps Institution of Oceanography, San Diego, CA, 1989.
- Davis, E. R., "Predictability of Sea Surface Temperature and Sea Level Pressure Anomalies over the North Pacific Ocean," *J. Phys. Ocean.*, no. 6, pp. 249-266, May 1976.
- D'Spain, G. L., W. S. Hodgkiss, and G. L. Edmonds, "Energetics of the Deep Ocean's Infrasonic Sound Field," *J. Acoust. Soc. Am.*, vol. 89, no. 3, pp. 1134-1158, March 1991.
- D'Spain, G. L., W. S. Hodgkiss, and G. L. Edmonds, "The Simultaneous Measurement of Infrasonic Acoustic Particle Velocity and Acoustic Pressure in the Ocean by Freely Drifting Swallow Floats," *IEEE J. Ocean. Eng.*, vol. 16, no. 2, pp. 195-207, April 1991.
- Daugherty, J. R. and J. F. Lynch, "Surface Wave, Internal Wave, and Source Motion Effects on Matched-Field Processing in a Shallow Water Waveguide," *J. Acoust. Soc. Am.*, vol. 87, no. 6, pp. 2503-2526, June 1990.
- De Fatta, D., J. Lucas, and W. S. Hodgkiss, *Digital Signal Processing*, John Wiley, N.Y., 1988.
- Etter, P. C., *Underwater Acoustic Modeling: Principles and Techniques*, Elsevier Applied Science, London, 1991.
- Evans, R. B., "A Coupled Mode Solution for Acoustic Propagation in a Waveguide with Stepwise Depth Variations of a Penetrable Bottom," *J. Acoust. Soc. Am.*, vol. 74, no. 1, pp. 188-195, July 1983.
- Feuillade, C., D. R. Del Balzo, and M. M. Rowe, "Environmental Mismatch in Shallow Water Matched-Field Processing: Geoacoustic Parameter Variability," *J. Acoust. Soc. Am.*, vol. 85, no. 6, June 1989.
- Feuillade, C., W. A. Kinney, and D. R. Del Balzo, "Shallow-Water Matched-Field Localization off Panama City, Florida," *J. Acoust. Soc. Am.*, vol. 88, no. 1, pp. 423-433, July 1990.
- Fizell, R. G., "Application of High-Resolution Processing to Range and Depth Estimation Using Ambiguity Function Methods," *J. Acoust. Soc. Am.*, vol. 82, no. 2, pp. 606-613, 1987.
- Gelb, A. (Ed.), *Applied Optimal Estimation*, MIT Press, Massachusetts, 1974.
- Geman, S. and D. Geman, "Stochastic Relaxation, Gibbs Distributions, and the Bayesian Restoration of Images," *IEEE Trans. Patt. Ana. Mach. Intel.*, no. 6, 721-741, November 1984.

- Gingras, D. F., "Methods for Predicting the Sensitivity of Matched-Field Processors to Mismatch," *J. Acoust. Soc. Am.*, vol. 86, no. 5, pp. 1940-1949, November 1989.
- Gordon, D. F. and H. P. Bucker, "Arctic Acoustic Propagation Model with Ice Scattering," NOSC Technical Report 985, Naval Ocean Systems Center, San Diego, CA, 30 September 1984.
- Hamson, R. M. and R. M. Heitmeyer, "Environmental and System Effects on Source Localization in a Shallow Water by the Matched-Field Processing of a Vertical Array," *J. Acoust. Soc. Am.*, vol. 86, no. 5, pp. 1950-1959, November 1989.
- Harris, F. J., "On the Use of Windows for Harmonic Analysis with the Discrete Fourier Transform," *Proc. IEEE*, vol. 66-1, pp. 51-83, 1978.
- Hodgkiss, W. S. and V. C. Anderson, "Acoustic Positioning for an Array of Freely Drifting Sensors," *IEEE J. Ocean. Eng.*, vol. OE-8, no. 3, pp. 116-119, 1983.
- Jensen, F. B., "Wave Theory Modeling: A Convenient Approach to CW and Pulse Propagation Modeling in Low-Frequency Acoustics," *IEEE J. Ocean. Eng.*, vol. 13, no. 4, pp. 186-197, October 1988.
- Johnson, D. H., "The Application of Spectral Estimation Methods to Bearing Estimation Problems," *Proc. IEEE*, vol. 70, pp. 1018-1028, September 1982.
- Kanasewich, E. R., *Time Sequence Analysis in Geophysics*, University of Alberta Press, Edmonton, Alberta, 1975.
- Kirkpatrick, S., C. D. Gellat, and M. P. Vecchi, "Optimization by Simulated Annealing," *Science*, vol. 220, pp. 671-680, May 1983.
- Le Blanc, L. R. and F. H. Middleton, "An Underwater Acoustic Sound Velocity Data Model," *J. Acoust. Soc. Am.*, vol. 67, no. 6, pp. 2055-2062, June 1980.
- Mackenzie, K. V., "Nine-Term Equation for Sound Speed in the Oceans," *J. Acoust. Soc. Am.*, vol. 70, no. 3, p. 808, September 1981.
- Metropolis, N., A. Rosenbluth, M. Rosenbluth, E. Teller, and A. Teller, "Equation of State Calculations by Fast Computing Machines," *J. Chem. Phys.*, vol. 21, pp. 1087-1092, 1953.
- Olivera, R. M., "Downslope Conversion Experiment: Environmental Data Report," MPL TM-414, Marine Physical Laboratory, Scripps Institution of Oceanography, San Diego, CA, 1990.
- Ozard, J. M., "Matched-Field Processing in Shallow Water for Range, Depth, and Bearing Determination: Results of Experiment and Simulation," *J. Acoust. Soc. Am.*, vol. 86, no. 2, pp. 744-753, August 1989.
- Palmer, L. B. and E. Powell, "A Range-Dependent Active System Performance Prediction Model (RASP)," NRL TR-400415, Naval Research Laboratory, Washington, DC, 1989.
- Penrose, R., "A Generalized Inverse for Matrices," *Proc. Cambridge Philos. Soc.*, vol. 51, pp. 406-413, 1955.

- Perkins, J. S., and R. N. Baer, "An Approximation to the Three-Dimensional Parabolic-Equation Method for Acoustic Propagation," *J. Acoustic. Soc. Am.*, vol. 72, no. 2, pp. 515-522, August 1982.
- Pierce, A. D., "Extension of the Method of Normal Modes to Sound Propagation in an Almost Stratified Medium," *J. Acoust. Soc. Am.*, vol. 37, no. 6, pp. 19-27, 1965.
- Pillai, S. U., *Array Signal Processing*, Springer Verlag, N.Y., 1989.
- Polvani, D. G., "Harmonic Sound Speed is Adequate for Transponder Navigation," *IEEE Oceans Conference Record*, vol. 1, 1984.
- Porter, M. B., R. L. Dicus, and R. G. Fizell, "Simulations of Matched-Field Processing in a Deep-Water Pacific Environment," *IEEE J. Ocean Eng.*, vol. OE-12, no. 1, pp. 173-181, January 1987.
- Press, W. H., B. P. Flannery, S. A. Teukolsky, and W. T. Vetterling, *Numerical Recipes in C*, Cambridge University Press, 1988.
- Ross, D., *Mechanics of Underwater Noise*, Pergamon Press, New York, 1976.
- Schmidt, R. O., "Multiple Emitter Location and Signal Parameter Estimation," *IEEE Trans. Antennas. Propag.*, vol. AP-34, no. 3, pp. 276-280, March 1986.
- Sorenson, H. W., *Parameter Estimation*, Marcel Dekker, New York, 1980.
- Sorenson, H. W., *Kalman Filtering: Theory and Application*, IEEE Press, New York, 1985.
- Sotirin, B. J., J-M. Q. D. Tran, and W. S. Hodgkiss, "Matched-Field Processing of Deep- Water Ambient Noise," *IEEE J. Ocean. Eng.*, vol. OE-15, no. 4, pp. 316-323, October 1990.
- Szu, H. and R. Hartley, "Fast Simulated Annealing," *Phys. Lett. A*, vol. 122, pp. 157-162, June 1987.
- Tappert, F. D., "The Parabolic Approximation Method," in *Wave Propagation and Underwater Acoustics*, J. B. Keller and J.S. Papadakis, Eds. New York: Springer-Verlag, 1977, pp. 224-281.
- Tolstoy, A., "Sensitivity of Matched-Field Processing to Sound Speed Profile Mismatch for Vertical Arrays in a Deep Water Pacific Environment," *J. Acoust. Soc. Am.*, vol. 85, no. 6, June 1989.
- Tolstoy, A., O. Diachok, and L. N. Frazer, "Acoustic Tomography via Matched-Field Processing," *J. Acoust. Soc. Am.*, vol. 89, no. 3, pp. 1119-1127, March, 1991.
- Tran, J-M. Q. D., "Approaches to the Processing of Data from Large Aperture Acoustic Vertical Line Arrays," SIO Reference 90-21, Scripps Institution of Oceanography, San Diego, CA, April 1990. Also, Ph.D. dissertation, University of California, San Diego, 1990.
- Tran, J-M. Q. D. and W. S. Hodgkiss, "Matched-Field Processing of 200 Hz Continuous Wave (cw) Signals," *J. Acoust. Soc. Am.*, vol. 89, no. 2, pp. 745-755, February, 1991.

Tran, J-M. Q. D. and W. S. Hodgkiss, "Sound Speed Inversion Using Large Aperture Vertical Line Array," submitted to *JASA* for publication, 1992.

Urick, R. J., *Principles of Underwater Sound*, 3rd ed. McGraw-Hill, New York, N.Y., 1983.

Zala, C. Z. and J. M. Ozard, "Matched-Field Processing in a Range-Dependent Environment," *J. Acoust. Soc. Am.*, vol. 88, no. 2, pp. 1011-1019, August 1990.

# REPORT DOCUMENTATION PAGE

Form Approved  
OMB No. 0704-0188

Public reporting burden for this collection of information is estimated to average 1 hour per response, including the time for reviewing instructions, searching existing data sources, gathering and maintaining the data needed, and completing and reviewing the collection of information. Send comments regarding this burden estimate or any other aspect of this collection of information, including suggestions for reducing this burden, to Washington Headquarters Services, Directorate for Information Operations and Reports, 1215 Jefferson Davis Highway, Suite 1204, Arlington, VA 22202-4302, and to the Office of Management and Budget, Paperwork Reduction Project (0704-0188), Washington, DC 20503.

1. AGENCY USE ONLY (Leave blank)		2. REPORT DATE September 1992		3. REPORT TYPE AND DATES COVERED Final: June 1990 - June 1992	
4. TITLE AND SUBTITLE VLF SOURCE LOCALIZATION WITH A FREELY DRIFTING ACOUSTIC SENSOR ARRAY				6. FUNDING NUMBERS 0602314N SUB87 RJ14C32 DN308105	
8. AUTHOR(S) G. C. Chen					
7. PERFORMING ORGANIZATION NAME(S) AND ADDRESS(ES) Naval Command, Control and Ocean Surveillance Center (NCCOSC) RDT&E Division (NRaD) San Diego, CA 92152-5000				8. PERFORMING ORGANIZATION REPORT NUMBER NRaD TR 1501	
9. SPONSORING/MONITORING AGENCY NAME(S) AND ADDRESS(ES) Office of Naval Technology 800 North Quincy Street Arlington, VA 22217				10. SPONSORING/MONITORING AGENCY REPORT NUMBER	
11. SUPPLEMENTARY NOTES					
12a. DISTRIBUTION/AVAILABILITY STATEMENT  Approved for public release; distribution is unlimited.				12b. DISTRIBUTION CODE	
13. ABSTRACT (Maximum 200 words)  This report documents the source localization and tracking capability of the freely drifting Swallow float volumetric array with the matched-field processing technique using data collected during a 1989 Swallow float experiment conducted in the Northeast Pacific.					
14. SUBJECT TERMS  antisubmarine warfare acoustic surveillance  Swallow float volumetric array VLF source localization				15. NUMBER OF PAGES 158	
				16. PRICE CODE	
17. SECURITY CLASSIFICATION OF REPORT UNCLASSIFIED	18. SECURITY CLASSIFICATION OF THIS PAGE UNCLASSIFIED		19. SECURITY CLASSIFICATION OF ABSTRACT UNCLASSIFIED		20. LIMITATION OF ABSTRACT SAME AS REPORT

UNCLASSIFIED

21a. NAME OF RESPONSIBLE INDIVIDUAL G. C. Chen	21b. TELEPHONE (include Area Code) (619) 553-4924	21c. OFFICE SYMBOL Code 732
---	--	--------------------------------



## INITIAL DISTRIBUTION

Code 0012	Patent Counsel	(1)
Code 144	V. Ware	(1)
Code 541	H.P. Bucker	(1)
Code 705	M. F. Morrison	(1)
Code 73	J. A. Roese	(1)
Code 732	C. E. Persons	(1)
Code 732	G. C. Chen	(5)
Code 733	D. K. Barbour	(1)
Code 804	J. Ziedler	(1)
Code 961	Archive/Stock	(6)
Code 964B	Library	(2)

Defense Technical Information Center  
Alexandria, VA 22304-6145 (4)

NCCOSC Washington Liaison Office  
Washington, DC 20363-5100

Center for Naval Analyses  
Alexandria, VA 22302-0268

Navy Acquisition, Research & Development  
Information Center (NARDIC)  
Washington, DC 20360-5000

GIDEP Operations Center  
Corona, CA 91718-8000